S.J. Bierma

Modelling a Cone Penetration Test in Dry Sand using the Material Point Method

A State-Dependent Constitutive Model Approach

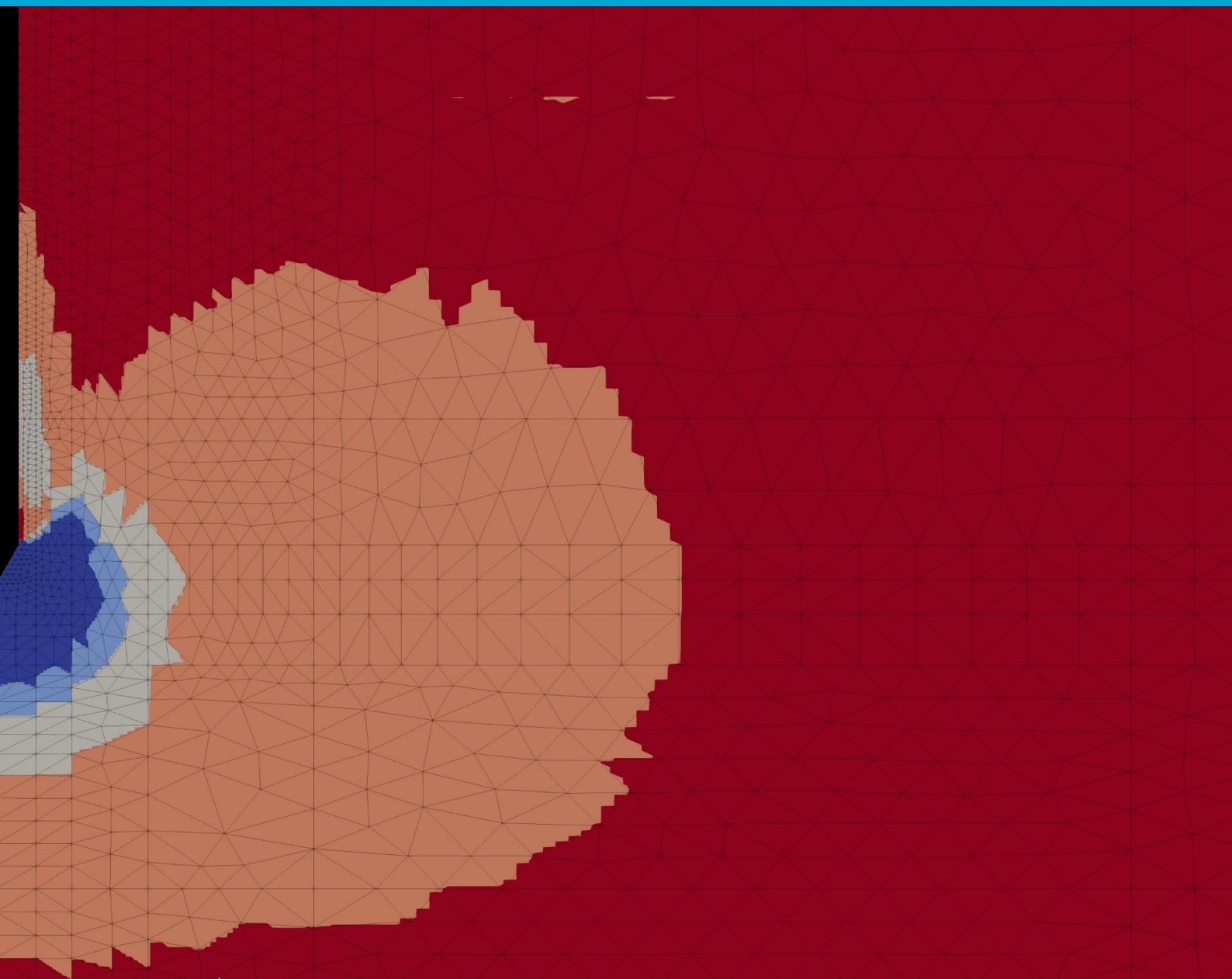

TU Delft

FUGRO

Modelling a Cone Penetration Test in Dry Sand using the Material Point Method

A State-Dependent Constitutive Model Approach

by

S.J. Bierma, BSc

in partial fulfilment of the requirements for the degree of

Master of Science
in Civil Engineering

Delft University of Technology
Faculty of Civil Engineering and Geosciences
Department of Geoscience & Engineering

Student number:	4467418
Master track:	Geo-Engineering
Project duration:	February 2021 - January 2022

Thesis committee:	Prof. dr. M.A. Hicks	TU Delft (Chair)
	Dr. F. Pisanò	TU Delft
	Dr. A. Askarinejad	TU Delft
	Dr. M. Martinelli	TU Delft
	Ir. F.J.M. Hoefsloot	Fugro

List of Tables

List of Figures

List of Symbols

Symbol	Description	Symbol	Description
a	Exponent in stiffness equation	Γ	Altitude of log-linear CSL
D	Dilatancy	γ_d	Dry unit weight
D_R	Relative density	ε	Total strain
D_c	Cone diameter	ε_1	Axial strain
e	Void ratio	ε_q	Deviatoric strain
e_Γ	Altitude of curved CSL	ε_v	Volumetric strain
e_c	Critical state void ratio	η	Stress ratio (q/p')
e_{max}	Maximum void ratio	θ	Lode angle
e_{min}	Minimum void ratio	λ	Slope of log-linear CSL
f_s	Shaft friction	λ_c	Slope of curved CSL
G	Shear modulus	ν	Poisson's ratio
G_{ref}	Shear modulus coefficient	ξ	Exponent in curved CSL equation
H	NorSand hardening modulus	ρ_{sur}	Density of surcharge layer
N	Volumetric coupling parameter	σ'_{v0}	Initial vertical effective stress
n	Porosity	ϕ_c	Friction angle at critical state
M	Critical friction ratio	χ	Soil property relating D_{min} to ψ
p'	Mean effective stress	ψ	State parameter
p_{ref}	Reference stress level $(= 100\,kPa)$	ψ_0	Initial state parameter
Q	Normalised cone resistance		
q	Deviatoric stress		
q_c	Cone resistance		
R	Overconsolidation ratio		
R^2	Coefficient of determination		
S_I	Sensitivity Index		
W	Work		

*Only frequently occurring or fundamentally important parameters are reported in the list of symbols.
*Increments of variables are either notated with a "d" in front of the symbol, or with a dot "." above. The two ways of notation mean the same and are interchangeable.
*Many variables can be expressed in terms of an elastic component or a plastic component. This is indicated in the symbols by a superscript of "e" and "p", for respectively elastic and plastic components.
*Many variables in this theses are expressed in terms of the condition in which they are determined. This could be e.g. during triaxial compression or at the image condition. When relevant, the condition at which the parameter is determined is indicated by a subscript and explained in the text.

List of Abbreviations

Abbreviation	Meaning
ALE	Arbitrary-Eulerian-Lagrangian
BC	Boundary condition
BE	Bender element
CC	Calibration chamber
CCR	Chamber cone ratio
CID	Consolidated isotropic drained
CPM	Cone pressure meter
CPT	Cone penetration test
CSSM	Critical state soil mechanics
CSL	Critical state locus
DCPM	Dynamic cone pressure meter
FEM	Finite element method
FLIP	Fluid-Implicit-Particle
HS	Hardening soil
LCC	Limit compression curve
MC	Mohr-Coulomb
MCSS	Mohr-Coulomb strain softening
MP	Material point
MPC	Material point cluster
MPM	Material point method
MSF	Mass scaling factor
NMD	Nodal Mixed Discretisation
NS	NorSand
OCC	Original Cam Clay
OWT	Offshore wind turbine
PIC	Particle-in-cell
PSD	Particle size distribution
RC	Resonant column
SS	Strain Smoothing

Preface

This MSc thesis marks the culmination of my civil engineering studies at Delft University of Technology. This research has been conducted as an internship at the GeoConsulting department of Fugro in Leidschendam. I would like to express my gratitude to Fugro for allowing me to conduct this internship and giving me the opportunity to experience the company from within.

For the past year I have had the opportunity to dive into the world of advanced numerical modelling, constitutive models and fundamental soil behaviour. This, under the supervision of my thesis committee consisting of: Prof. dr. M.A. Hicks, Dr. F. Pisanò, Dr. A. Askarinejad, Dr. M. Martinelli and Ir. F.J.M. Hoefsloot. I would like thank my thesis committee for their guidance throughout the project and for sharing their expertise. A special thanks to Mario Martinelli and Flip Hoefsloot, with whom I had frequent, even daily, discussions about the results and progress of the project.

Furthermore, I would like to thank my colleagues at Fugro for making this internship a pleasant experience.

Last but not least, I thank my friends and family for their unconditional support throughout the project.

S.J. Bierma
Delft, January 2022

Abstract

The numerical modelling of a cone penetration test (CPT) has long been a challenging task due to the large deformations associated with the penetration of a CPT. Recent developments in advanced numerical methods have shown promising results in overcoming these difficulties by using the Material Point Method (MPM). In this thesis it is researched whether the MPM is able to reliably produce CPT results in dry sand by using a state-dependent constitutive model. Calibration chamber (CC) tests are modelled for dry sand and results are compared with experimentally performed CC tests in the laboratory. Features regarding the numerical setup and applied boundary conditions which quantitatively influence modelling results are identified and assessed before the model is validated to real CC test data. Validation results show that the model is able to accurately produce cone resistance values for different types of sand for soil states that can be categorised as moderately-dense to dense. Last, it is shown how parameters within the constitutive framework affect the model output and a quantification of the sensitivity of the parameters to model results is presented.

Keywords: sand, CPT, soil state, constitutive relations, MPM, calibration chamber tests.

Summary

Fugro is developing a new site investigation device in cooperation with the TU Delft. This device is a further development of the already existing Cone Pressure Meter (CPM), and is called the Dynamic Cone Pressure Meter (DCPM). The harmonic excitation of the membrane of the DCPM will allow for a better determination of dynamic in-situ soil properties such as the damping ratio. This is particularly relevant to the construction of near- and offshore wind turbines founded on monopiles, where the dynamic loads of wind and waves are important factors to consider in the design.

An acknowledged problem of the DCPM, however, is the fact that during installation of the device, penetration of the cone behind which the DCPM is attached causes disturbance to the soil. As the pressuremeter device is located behind the cone, the test is conducted in disturbed soil conditions rather than the initial in-situ soil conditions. This can lead to incorrect interpretation of the DCPM measurements. To be able to correctly interpret DCPM results it is desired to quantify the disturbance caused by the penetration of the cone. For this purpose numerical models are used.

Before any quantification of the disturbance around the cone can be assessed it first has to be proven that the numerical model is able to produce accurate results of a cone penetration test (CPT). Recent developments in the field of geotechnical numerical modelling have shown promising results of modelling a CPT using the Material Point Method (MPM). However, obtaining quantitative accurate CPT results with the MPM has not yet been achieved. This is related to limitations in the constitutive models used in previous research. The objective of this thesis is therefore to investigate if the MPM using a more advanced constitutive model is able to produce reliable results of modelling a CPT in dry sand, which are quantitatively in agreement with experimental tests conducted in the laboratory. NorSand is such a promising advanced constitutive model and is applied in this thesis. The accompanying main research question to this objective is formulated as follows: *"Is the MPM using NorSand as its constitutive model suitable as a reliable quantitative modelling tool for a CPT in dry sand?"*

To achieve the objective, the research part of this thesis is divided into four phases: the numerical verification phase, the boundary condition analysis, the validation phase and the NorSand parameters sensitivity analysis. For each phase the approach and most relevant results and conclusions are discussed.

The goal of the numerical verification phase is to determine the optimal numerical calculation settings and setup before model validation. Quantitative differences caused by changing the numerical settings or setup are assessed and it is examined whether a certain setting or setup should be used in the validation phase or not. Roughly speaking this phase consists of three parts. First, the optimal values for the most important numerical settings are determined by performing small sensitivity analyses. Second, the optimal mesh size is determined by performing a mesh size analysis. This analysis showed that it is possible to determine an optimal value of the mesh size for the cone resistance, but that changing the mesh size adjacent to the shaft led to inconsistencies in the sleeve friction. Attempts have been made to solve these inconsistencies but these were unsuccessful. However, it is shown that the current implementation of NorSand is a possible cause for the discrepancies in the results. It is therefore concluded that although the sleeve friction results are in the expected order of magnitude, it cannot be reliably obtained due to the inconsistencies related to the mesh size. Last, an analysis is performed to investigate

the effect of using a different type of element. This analysis showed a quantitative difference in cone resistance between triangular and quadrilateral elements. Further investigation into these observations proved that the different methods used to mitigate volumetric locking is the cause of this difference. Ultimately it is decided to use quadrilateral elements in the validation phase because no volumetric strains are shared between adjacent elements when this element type is used.

The goal of the boundary condition (BC) analysis is to assess how different boundary conditions affect model results and whether this corresponds to what has been reported in literature about the boundary conditions of calibration chamber (CC) tests. In this analysis the bottom BC and lateral BC are assessed. The analysis showed that using a rough bottom BC provides results which best agree with free field conditions. The analysis of the effects of a change of the lateral BC on model results is more elaborately compared to the bottom BC, since the effect of changing the chamber size is also included in this analysis. For four different chamber sizes, the cone resistance results of a constant stress lateral BC and zero displacement lateral BC are assessed. Since the density of the sand is known to influence the response generated by the BC, the lateral BC analysis is performed for three different sand densities, ranging from sand characterised as loose to sand characterised as dense. The results of the lateral BC analysis showed that changing the lateral BC in the MPM has similar implications on the results as changing the lateral BC in real CC tests as is reported in literature. Ultimately, the boundary condition analysis qualitatively confirms the correct functioning of the boundary conditions in the MPM model with NorSand.

During the model validation phase the goal was to evaluate whether cone resistance results of the MPM model are quantitatively in agreement with experimental CC tests. Three types of sand are assessed whose CC test results are obtained from literature. For one additional sand CC tests with a preliminary DCPM device are performed in the laboratory. To account for uncertainties related to the preparation of the initial density of the sand samples, a margin of uncertainty is included in assessing the agreement between model results and the CC tests. The results of the sands obtained from literature show that there is a good agreement between the cone resistance obtained from the MPM model and CC tests for sands at densities that can be categorised as moderately-dense to dense when the boundary conditions are properly applied. For sands in a looser state the model overestimates the cone resistance in certain cases, so caution is advised when interpreting model results of loose sand.

The goal of the NorSand parameter sensitivity analysis is to obtain insight in how the NorSand parameters affect cone resistance results. By comparing a reference scenario to scenarios where single NorSand parameters are changed, the sensitivity of that parameter to the cone resistance is assessed. It is evaluated whether the obtained changes in cone resistance due to a change of a certain NorSand parameter can be substantiated with the theory of that specific parameter. The results of this analysis provided clear insights in how sensitive the NorSand soil and state parameters are. For each parameter it has been confirmed that changing the parameters affects the cone resistance as would be expected based on the underlying theory. This confirms the correct functioning of the NorSand parameters within the constitutive framework.

The answer to the main research question whether the MPM is suitable as a reliable quantitative modelling tool for a CPT using NorSand as its constitutive model can only partly be confirmed. Compared to other constitutive models the advanced description of dilatancy in NorSand is regarded an important feature. The validation phase has shown that for certain sands in loose states the MPM tends to overestimate the cone resistance. Furthermore, inconsistencies in the obtained sleeve friction due to numerical factors prevent the complete reliable modelling of a CPT. For both aspects, further investigation into whether these problems can be solved is recommended.

Contents

1 Introduction

1.1 Background

Site characterisation of soil is of great importance to construct safe structures and reduce ground-related uncertainties. This has long been acknowledged and the development of methods to characterise soil on-site and determine its strength has been an active subject of research for as long as geotechnical engineering has been of interest.

Developments in the field of site investigation and in-situ soil characterisation are of particular interest to companies conducting these activities, as these developments allow such companies to increase the quality and efficiency of their operations. Fugro is a company which has been actively involved in conducting site investigation since its founding in 1962, and has been actively contributing to the research and development of new devices and investigation techniques ever since. Currently, Fugro is developing a new site investigation device which is able to measure dynamic in-situ soil properties: the Dynamic Cone Pressure Meter (DCPM).

The DCPM is a further development of the already existing Cone Pressure Meter (CPM). The pressuremeter is a device characterised by a cylindrical probe with a flexible membrane which is able to excite and apply a pressure to the wall of a borehole. By doing so, stiffness and strength parameters of the soil can be obtained (Houlsby & Withers, 1988). The DCPM is a further development of the CPM, in that it will be able to excite the membrane harmonically, whereas the CPM is only able to excite the membrane once. The harmonic excitation of the DCPM allows for a better determination of dynamic in-situ soil properties (e.g. damping ratio). This is especially relevant for the construction of offshore wind turbines (OWTs) founded on monopiles. In offshore conditions, loads from wind and waves result in dynamic soil behaviour. The soil has to be able to withstand these dynamic loads to ensure a stable foundation and safe operation of the OWT. With the upcoming energy transition towards more sustainable energy sources, the expectation is that the size of OWTs will increase resulting in more demands on the foundation. It is also expected that the depth at which the OWTs will be placed will increase, leading to a higher share of foundation costs on the total costs of an OWT (Oh et al., 2018). A better determination of dynamic soil properties by the DCPM can lead to a less conservative foundation design without compromising safety standards. This can potentially save costs on the foundation, which becomes progressively more important with increasing OWT sizes and installation depths.

The installation of the CPM (and future DCPM) is achieved by driving the device into the ground by attaching it behind a cone which is pushed into the soil. This type of installation is called a full displacement method. One of the motivations for the development of the full

displacement technique was to increase the feasibility of CPM investigation for offshore applications. At the time the two alternative installation techniques to bring a pressuremeter to depth (namely, lowering into a pre-drilled hole and the self boring pressuremeter) were not convenient for deep offshore operations (Withers et al., 1986). The full displacement pressuremeter intended to add the possibility of obtaining accurate soil stiffness and strength parameters from the pressuremeter, combined with the convenience of the Cone Penetration Test (CPT) (Withers et al., 1989).

1.2 Problem description

Beside the convenience the full displacement pressuremeter entails by attaching it behind a cone, a downside is that the penetration of the cone results in disturbance of the soil around the cone. Changes in e.g. stress state, density or soil fabric induced by the cone penetration could influence the response of the soil close to the dynamic pressuremeter. A consequence of the soil disturbance around the cone could be that the DCPM inaccurately measures the actual in-situ soil properties. Before the DCPM measurements can be reliably interpreted, it is necessary to quantify the disturbance of the soil caused by the cone penetration. A method to achieve this is by using large displacement numerical modelling techniques.

Developments in the field of geotechnical numerical modelling have allowed for the modelling of problems involving large deformations (which is the case for a cone penetration) using the Material Point Method (MPM). Previous research has shown that the MPM has the potential to model disturbance around a penetrated cone in dry sand (Martinelli & Galavi, 2021; Schuringa, 2020).

An important factor in a numerical model calculation is the selected constitutive model. A constitutive model defines the mechanical behaviour of a material in a continuum framework. Selecting a different constitutive model can lead to an entirely different formulation of the relationship between stresses and strains, and can heavily influence the results of a numerical calculation. It is of importance that the constitutive model selected in a numerical calculation is able to accurately describe relevant features of soil behaviour of the problem at hand. For the modelling of a CPT this includes e.g. an accurate description of both peak and residual strength and the incorporation of density effects. In both the studies of Schuringa (2020) and Martinelli and Galavi (2021) constitutive models were used which do not meet all requirements for accurate soil modelling of a CPT, resulting in inaccurate quantitative model results (the constitutive models previously used were Mohr-Coulomb Strain Softening and Hardening Soil respectively). To accurately obtain numerical model results of a CPT which are quantitatively in agreement with experimental observations, a more advanced constitutive model is desired. A constitutive model which has the potential to accurately model a CPT is called NorSand (Jefferies, 1993). However, this has not yet been validated and is what will be investigated in this thesis.

1.3 Research objective and scope

The objective of this thesis is to investigate if the MPM using NorSand as its constitutive model is able to produce reliable results of modelling a CPT in dry sand, which are quantitatively in agreement with experimental tests performed in the laboratory.

To be able to prove the maturity of the model, a variety of MPM studies have to be conducted. These include the investigation into numerical settings, the effect of different boundary conditions, the validation to experimental test data for different types of sand and an investigation into the sensitivity of input model parameters to model output.

The material that will be modelled in this research is dry sand. In selecting the types of sand that will be modelled it is important to consider the availability of published literature, both for the determination of model input parameters as well as for the eventual validation.

1.4 Research questions

1.4.1 Main research question

The main research question of this thesis is formulated as follows:

"Is the MPM using NorSand as its constitutive model suitable as a reliable quantitative modelling tool for a CPT in dry sand?"

1.4.2 Sub-research questions

As a guide towards answering the main research question, several sub-research questions have been drafted. They are grouped by topic and listed below:

- **Material Point Method**
  - *"Why is the MPM suitable for modelling a CPT?"*
  - *"What are the quantitative effects of changing numerical MPM settings and what is the optimal numerical setup for the analysis?"*
- **Constitutive model**
  - *"Why is NorSand a suitable constitutive model for a CPT analysis in dry sand?"*
  - *"How can NorSand input parameters be determined?"*
  - *"What is the effect of changing NorSand input parameters on the model output results?"*
- **Model validation**
  - *"Which experimental data is available and is this data reliable to validate the MPM model to?"*
  - *"Are MPM model results quantitatively in agreement with experimental results?"*

1.5 Thesis outline

To answer the research questions, the research part of this thesis is divided into four phases:

1. Numerical verification phase: in this phase it is investigated how the numerical settings and numerical setup of the MPM influence the model results.
2. Boundary condition analysis: here it is investigated how the different boundary conditions the model offers affect modelling results.
3. Validation phase: in this phase it is investigated if the MPM produces results that can be reliably validated to experimental data.
4. NorSand parameter sensitivity analysis: in this phase the effect of changing NorSand input parameters on model results are examined.

The Chapters are structured as follows:

Chapter 2 contains the literature study conducted during this thesis.

Chapter 3 describes how the model is setup and how various features within the model are defined.

Chapter 4 describes how the NorSand input parameters can be determined for different types of sand.

Chapter 5 contains the results of the numerical verification phase.

Chapter 6 contains the results of the boundary condition analysis.

Chapter 7 contains the results of the validation phase.

Chapter 8 contains the results of the NorSand parameter sensitivity analysis.

Chapter 9 consists of the conclusions drawn from the conducted research. Here the main research question is also answered.

Chapter 10 describes the recommendations for further research regarding this research topic.

2

Literature Study

This Chapter provides an overview of the most relevant literature research conducted during this thesis.

Three main subjects will be discussed. First, numerical methods are discussed where special emphasis is placed on the Material Point Method. Second, the used constitutive model will be elaborated on. Last, a compression model for cohesionless soils will be explained which is of importance for later calibrations of the critical state locus.

2.1 Numerical modelling

2.1.1 Introduction

Numerical models are widely used in geotechnical engineering. The increase in computational power over the past decades has allowed scientists and engineers to solve increasingly complex problems. With the development of commercial software (e.g. PLAXIS), numerical calculation methods have become increasingly available to engineers who use them in their everyday design process (Carter et al., 2000).

In a numerical model the domain of a problem is made up of elements with boundary conditions defining the conditions at the edges of the domain. Depending on the type of numerical model a material can be discretised as e.g. elements or points in the domain. Stress strain relationships of the material are solved using constitutive equations. Numerical models are relatively cost efficient when compared to laboratory testing or large scale testing. They are also able to solve challenging problems, whereas purely analytical relations often only suffice in simplified situations.

Numerical modelling is an active field of research in geotechnical engineering where new techniques are being developed and existing techniques are improved. This Section gives an overview of different types of techniques that exists and will compare these to one another. Special emphasis is placed on the Material Point Method (MPM), which is the numerical calculation method used in this thesis. The most relevant characteristics of the specific MPM program used in this thesis are also addressed.

2.1.2 Different types of numerical calculation methods

Based on how deformations and motions are defined in the domain, spatial discretisation in numerical methods can be distinguished into three groups: Lagrangian, Eulerian and hybrid methods (Zhang et al., 2016).

Lagrangian methods

In Lagrangian methods the computational grid is embedded and deformed with the material. Defining the deformations this way has the following advantages (Zhang et al., 2016):

1. The solution process is simplified as there is no movement of the material between adjacent mesh cells, so no advection term is needed in the governing equations.
2. It is relatively easy to impose boundary conditions because the element boundaries coincide with the material interface.
3. It is relatively easy to implement history dependent constitutive models because the flow of individual masses is considered.

Figure 2.1 shows an example of a Lagrangian grid with an applied deformation. It can be clearly seen that the deformation of the material with the grid results in distortions of the elements. Severe element distortion results in significant numerical errors in the calculation. A stable solution is obtained when the time step is smaller than a critical time step. This critical time step condition is known as the Courant-Friedrichs-Lewy or CFL condition (Courant et al., 1967) shown in Eq. 2.1

$$\Delta t_{cr} = \min_{e} \frac{T^{e}_{min}}{\pi} = \min_{e} \frac{l^{e}}{c} \tag{2.1}$$

where T^{e}_{min} is the smallest period of element e, l^{e} is the characteristic length of element e and c is the speed of sound. Element distortion will lead to a reduction of the characteristic length of an element. If the distortion continues and becomes severe the time step in a Lagrangian calculation eventually reaches zero and the calculation is terminated (Zhang et al., 2016). The inability of Lagrangian methods to model large deformations or motions due to the limitations of element distortion is one of the largest drawbacks of using Lagrangian methods.

An example of a Lagrangian method is the Finite Element Method (FEM), which has been (and currently is) extensively researched over the past decades and is widely accepted as a capable modelling tool for geotechnical applications.

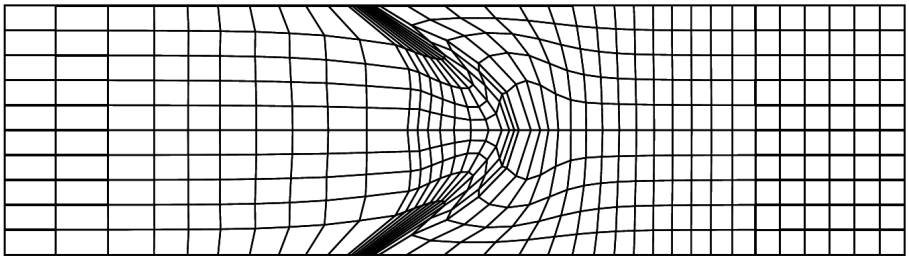

Figure 2.1: Example of a deformation applied in a Lagrangian grid. Adopted from Zhang et al. (2016).

Eulerian methods

In Eulerian methods the computational grid is fixed and the material moves though the grid. This method does not suffer from element distortions as is the case with Lagrangian methods. However, physical variables (e.g. mass, momentum, energy, temperature) advect between adjacent elements. An advection term is required in the governing equations making them conceptually more complex and less efficient (Zhang et al., 2016).

Eulerian methods are suitable for modelling large deformations. An example application of this method is in modelling fluid dynamics. Purely Eulerian methods are generally not used for modelling geotechnical problems, as for most situations the order of magnitude of the deformations allow for Lagrangian methods to be used which are then more accurate and more easily to implement.

Figure 2.2 shows an example of a deformation in an Eulerian grid. Here, it is visible that the elements remain at a constant volume and the material flows through the domain.

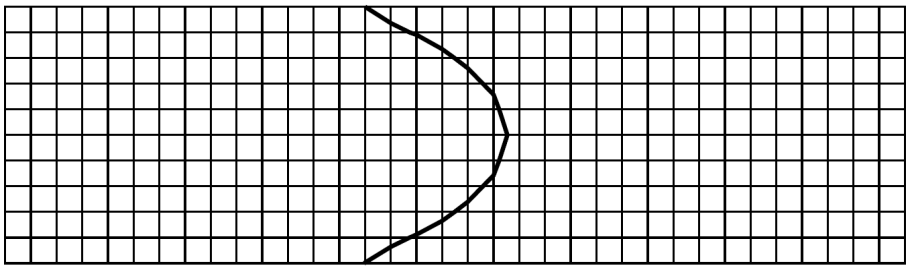

Figure 2.2: Example of a deformation applied in a Eulerian grid. Adopted from Zhang et al. (2016).

Hybrid methods

Using purely Lagrangian or Eulerian methods results in their respective shortcomings and advantages as described above. To be able to better solve challenging problems a combination of the two methods can be used, which is then called a hybrid method. Two examples of a hybrid method are the Arbitrary Eulerian-Lagrangian (ALE) method (Donea et al., 2004) and the Particle-In-Cell (PIC) method (Evans & Harlow, 1957).

In an ALE description the nodes of the computational mesh can be moved in a Lagrangian way, in a Eulerian way or in some arbitrary specified way to give a continuous rezoning capability. This offers more freedom in the movement of the mesh and allows for larger distortions than a purely Lagrangian method, with a greater resolution than if only a Eulerian method would be used (Donea et al., 2004). A disadvantage of this method is that a convective term is still necessary. It is also difficult to design an efficient mesh moving algorithm, especially in 3D problems (Zhang et al., 2016). Figure 2.3 shows an example motion using an ALE method.

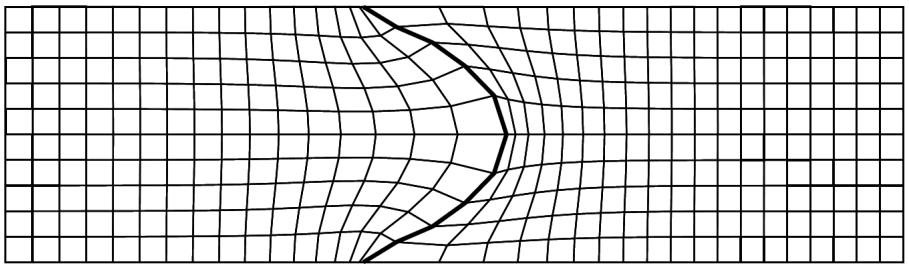

Figure 2.3: Example of a deformation applied in an ALE grid. Adopted from Zhang et al. (2016).

The PIC method was initially developed to solve fluid dynamics problems. The fluid is discretised as Lagrangian particles which contain the material position and mass. The mesh is uniform Eulerian. A complete calculation step consists of two phases: a Lagrangian phase and an Eulerian phase. The Lagrangian phase updates all quantities except the advection. The Eulerian phase moves the particles and accomplishes all advective fluxes (Harlow, 2004). During

the Lagrangian phase the variables including the mesh nodes and particles are advanced. In the Eulerian phase the mesh is mapped back to its original position. The particles are then at their new position (Evans & Harlow, 1957).

The original PIC method is only partially Lagrangian in that only mass and position are carried by the particles. Remaining quantities such as momentum and total energy are still stored in the grid. The transfer of information between the particles and the grid leads to numerical diffusion. Two possible ways to reduce this numerical diffusion are:

1. Using a second-order accuracy for the advective term. The scheme is close to the original PIC method. Only mass and position are carried by the particles. Momentum and energy are treated similarly as the original PIC method, but more accurately (Nishiguchi & Yabe, 1983).

2. Using a fully Lagrangian particle method. An example is the Fluid-Implicit-Particle (FLIP) method. In this method the properties of the fluid are carried by the particles, including momentum and energy. Discretisation of the particles in this manner eliminates a substantial source of numerical dissipation (Brackbill & Ruppel, 1986).

2.1.3 Material point method

The Material Point Method (MPM) stems from the task to improve computational fidelity and efficiency of the Finite Element Method (FEM). A research team started to combine computational fluid dynamics with computational solid dynamics (Zhang et al., 2016). The result was a continuum based particle method (Sulsky et al., 1994), which was later called the Material Point Method (MPM).

The MPM is an extension of the FLIP method with two fundamental differences (Sulsky et al., 1994):

1. FLIP has been used for materials with history independent constitutive equations. For these type of materials it is convenient to solve the constitutive equations at the nodes of the mesh. In MPM the constitutive equations are solved at the material points. This allows each material point to be tracked, and history-dependent variables such as plastic strain can be associated with that material point throughout the entire analysis. This enables MPM to model history-dependent materials.

2. The MPM is formulated in the weak form consistent with FEM. The weak form means that differential equations are solved incrementally instead of completely solving the differential equations.

An illustration of the different phases within a single time step of MPM is shown in Figure 2.4. A description of the phases is as follows (Zhang et al., 2016):

a. At the start of the time step the information is transferred from the material points to the nodes on the computational mesh using mapping functions.

b. The governing equations are solved at the nodal mesh points and the quantities are updated (e.g. nodal acceleration).

c. Variables of the material points are updated by the new values from the mesh nodes using mapping functions. Stresses at the material point are updated from the specific constitutive relation.

d. Because all information is transferred back to the material points the mesh contains no information and can be freely reset for the next time step.

The MPM utilises the advantages of both Lagrangian and Eulerian methods. Compared to Lagrangian methods, mesh distortion and mesh entanglement problems are avoided in extreme cases (e.g. penetration problems). Compared to Eulerian methods, problems regarding numerical diffusion are solved due to the mapping of variables from the grid nodes to material points and vice versa.

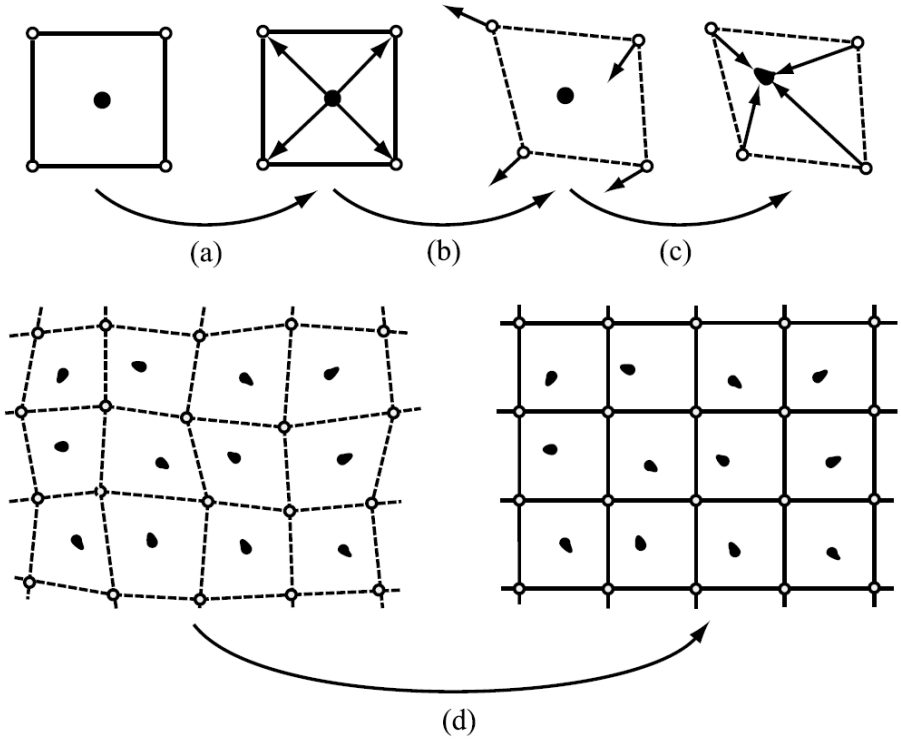

Figure 2.4: Illustration of a single time step of the MPM. Adopted from Zhang et al. (2016).

2.1.4 Comparison between MPM and FEM

The MPM can be seen as an extension of the FEM. The two methods have much in common. Both are formulated in the weak form and the governing and system of equations at the nodes are identical in both cases (Ceccato et al., 2019). However, beside the differences in ability to calculate large displacements previously mentioned, there are also differences in computational efficiency and accuracy which are important to consider when deciding which method to select for a certain problem.

Efficiency

The computational efficiency depends on the computational cost per time step and the time step size.

In the MPM additional steps are needed for the mapping of variables between the material points and the mesh nodes. In the FEM these mapping steps are not required because variables are carried at grid nodes and do not have to be recalculated at the beginning of every time step and Gauss points deployed in the FEM do not move relative to the mesh as is the case with material points. Additionally, the FEM deploys one Gauss point per element, whereas the

MPM usually has one, four and eight material points for 1D, 2D and 3D problems respectively. The additional mapping steps per time step and higher number of material points per element result in a higher computational cost for the MPM compared to the FEM (Zhang et al., 2016).

For the FEM the time step size is heavily influenced by the distortion of the mesh as is shown in Eq. 2.1. The decrease of the required time step with increasing distortion makes the FEM inefficient for large deformation problems. The MPM does not suffer from this problem as the mesh is reset after every time step.

Accuracy

If grid (MPM) and element (FEM) size are comparable, the differences in accuracy mainly depend on the quadrature scheme of the method and the ability to deal with large deformations. In a numerical analysis the term "quadrature" refers to the method of approximation of a definite integral.

The FEM employs a Gaussian quadrature scheme which can integrate more accurately in the weak form than the particle quadrature scheme used in the MPM.

When elements are heavily distorted in the FEM, the Jacobian matrix decreases to zero which introduces errors or even completely terminates the calculation. Techniques exist to continue the FEM calculation (e.g. erosion or remeshing techniques), but these are accompanied by their own errors in calculation. For situations with large deformations the MPM can be more accurate than the FEM (Zhang et al., 2016).

2.1.5 Numerical modelling of a CPT

From the previous Sections it has become apparent that the order of magnitude of the deformations of the problem are decisive in choosing the type of numerical method. Due to the extreme deformation which occurs during penetration problems such as the CPT the FEM is not suitable for modelling these types of problems.

The MPM is able to produce accurate results while dealing with the extreme deformations. Due to the similarities with the FEM the same constitutive relations can be implemented in the MPM. This means that the knowledge on soil behaviour and constitutive models acquired through working with FEM can be used in MPM codes as well.

Considering all aspects, the MPM shows promise for modelling CPT type of problems provided an adequate constitutive model is present.

Other numerical methods

For completeness it is noted that beside the MPM other advanced numerical methods have been used to model CPT problems. Each method has its own strengths and weaknesses. Because in this theses the MPM is used, a complete description of these methods is deemed outside the scope of this literary research. For the interested reader a small list with examples of other numerical methods used to model a CPT is presented below.

- Discrete Element Method (DEM) (Arroyo et al., 2011);
- Smoothed Particle Hydrodynamics (SPH) (Kulak & Bojanowski, 2011);
- Coupled Eulerian Lagrangian Method (CEL) (Fallah et al., 2016);
- Arbitrary Lagrangian-Eulerian Method (ALE) (Van den Berg, 1994).

2.1.6 Program specific aspects

The MPM program used in this thesis is a version of the Anura3D MPM Software developed by the Anura3D MPM Research Community. Certain settings and features are used in the calculations performed in this thesis which are worthwhile to be elaborated upon.

2D axisymmetric formulation

Many problems in geotechnical engineering are axisymmetric, including a CPT. If the rotational symmetry of the CPT and the soil is considered, the computational cost can be significantly decreased because a smaller domain would be required and fewer material points are needed. An axisymmetric formulation based on a formulation developed by Sulsky and Schreyer (1996) is implemented in the Anura3D program. Compared to 3D simulations, the results of the 2D axisymmetric simulations are the same while having a significant lower computational cost (Galavi et al., 2019). In the 2D axisymmetric formulation a material point represents the volume of one radian around the ring of symmetry.

In all calculations performed in this thesis the 2D axisymmetric formulation is used.

Moving mesh concept

A moving mesh concept is applied during the simulation of the CPT (Al-Kafaji, 2013). Because all properties of the continuum are stored in the material points and no permanent information is stored in the mesh, the mesh can be redefined after each time step. When using the moving mesh concept the mesh can be distinguished in two parts:

1. Moving mesh: this part of the mesh moves along with the displacement of the CPT. The boundary elements adjacent to the CPT surface remain adjacent to that surface throughout the entire simulation. The elements in the moving mesh region of the domain keep the same size during the calculation.

2. Compressible mesh: this part of the mesh is compressed as the moving mesh is displaced. The compression of this zone is linearly distributed along the depth. The nodes in contact with the moving mesh have the same displacement as the moving mesh, and the nodes at the bottom boundary have zero displacement.

Figure 2.5 shows an illustration of the moving mesh concept applied to a pile driving problem (which is very comparable to the CPT problems simulated in this thesis).

Using a moving mesh yields two large advantages.

1. Mesh refinement only has to be applied directly around the cone. The refined area moves along with the penetration of the cone. This way, the fine mesh is always kept around the cone. If no moving mesh is used the entire area the cone is expected to penetrate into has to be refined. This results in more calculations at locations in the domain which are not of importance and is therefore inefficient.

2. There is no need to identify new soil-structure interfaces during the simulation because the interface nodes coincide with the geometry of the cone throughout the entire simulation. Inaccuracies related to redefining these interfaces are therefore eliminated (Al-Kafaji, 2013).

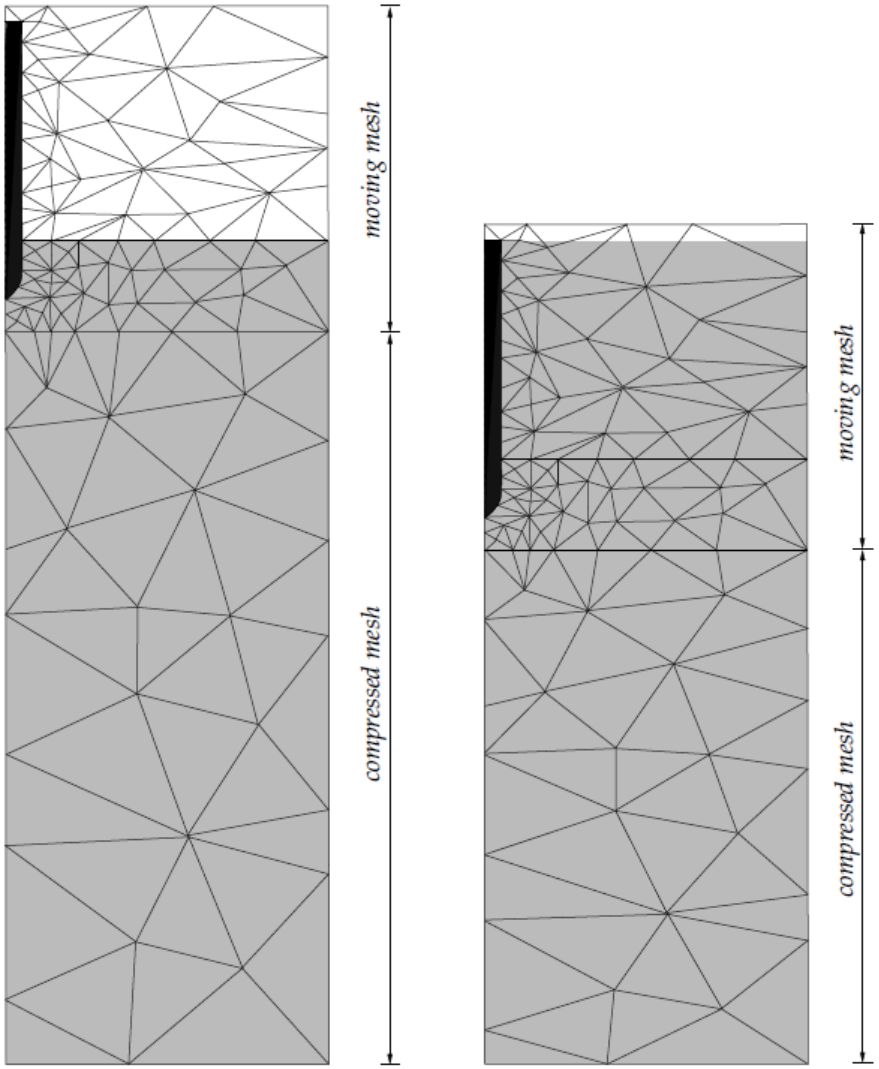

Figure 2.5: Illustration of the moving mesh concept applied to a pile driving problem: (left) initial condition and (right) situation after penetration of the pile. Adopted from Al-Kafaji (2013).

Anti-volumetric locking

One of the shortcomings of the MPM, inherited from the close description with FEM, is the volumetric locking of elements that can occur due to the linearity of shape functions when nearly incompressible solids are modelled. The area of an incompressible element must remain constant. For linear 3-node elements this means that nodes are restricted in their degrees of freedom. When incompressible elements are assembled together it might be that certain nodes have no degrees of freedom left and become locked up. This type of locking usually propagates through the mesh, resulting in an unrealistic stiff response. An illustration of this volumetric locking of triangular elements is shown in Figure 2.6. In this example, node 3 of Figure 2.6c is locked by the constraining nodes 1, 2 and 4. As a result the volume of elements e_1 and e_2 cannot change.

To mitigate volumetric locking problems the Nodal Mixed Discretisation (NMD) technique is used (in this thesis this technique is also referred to as strain smoothing). This technique averages volumetric strains of elements which share nodes. This increases the number of degrees

of freedom per element, resolving volumetric locking problems (Ceccato et al., 2019).

In 2D and 3D situations the NMD technique is sufficient for solving volumetric locking problems. However, in a 2D-axisymmetric situation the smoothed volumetric strains are inaccurate close to the axis of symmetry due to the inaccurate calculation of the volume of the nodes. In these situations it is therefore necessary to use higher order shape elements to calculate nodal volumes (Martinelli & Galavi, 2021).

Another method to prevent volumetric locking is the B-Bar method (Hughes, 2000). The B-Bar method separates the volumetric and deviatoric components of the B-matrix. The deviatoric strains are calculated in all Gauss points of the element, whereas the calculation of the volumetric stain is reduced to a single Gauss point in the centre in the element by averaging. Using the B-Bar method is possible because when the MPM-Mixed calculation method is used, Gauss integration is also partly applied (see Section 5.2.1 for a more detailed description of the MPM-Mixed method).

In this thesis the B-Bar method is solely used for quadrilateral elements. Quadrilateral elements with a linear shape function have four Gauss points per element, which enables the averaging of volumetric strains over the Gauss points. Linear triangular elements only have one Gauss point per element to begin with, resulting in no effect when applying the B-Bar method to mitigate volumetric locking in the system.

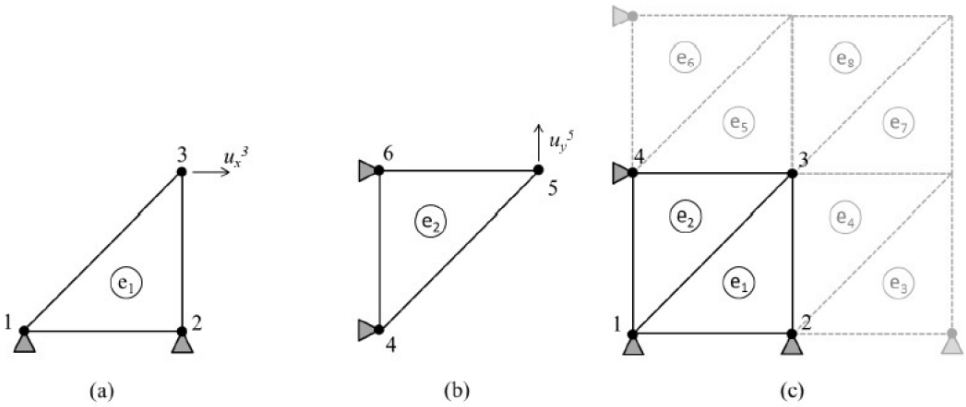

Figure 2.6: Illustration of volumetric locking for linear triangular elements. Adopted from Ceccato et al. (2019).

2.2 Constitutive model: NorSand

2.2.1 Introduction

Constitutive models are an important aspect of numerical modelling. A constitutive model defines the mechanical behaviour of a material in a continuum framework. It describes the relationship between stress and strain increments, generally described in Eq. 2.2.

$$\underline{\dot{\sigma}} = \underline{\underline{M}}\, \underline{\dot{\varepsilon}} \tag{2.2}$$

Here $\underline{\dot{\sigma}}$ is the stress increment, $\underline{\dot{\varepsilon}}$ is the strain increment. The stiffness matrix $\underline{\underline{M}}$ is formed by the constitutive model.

The development of constitutive models (or stress-strain relationships) has been of interest to researchers since the early days of soil mechanics. Many constitutive models have been developed in the past, each for specific conditions and with their own assumptions. The choice of which constitutive model to use depends on the type of soil that is modelled and on the specific conditions of the problem at hand. It is important that the selected constitutive model is able to a capture the desired mechanical behaviour of the soil as this has a significant effect on modelling results.

Broadly speaking two types of constitutive models can be distinguished (Jefferies & Been, 2016):

1. Descriptive models: these type of models are based on fitting to test data. In situations where the problem is similar to the test conditions, descriptive models can produce accurate results. However, when modelling more general situations which differ from the testing conditions used to develop the model, the accuracy is often compromised by a lack of insight of underlying physical processes.

2. Idealised models: postulated mechanics form the basis of these types of models. Because of the fundamental principle of these models, results are more accurate over a broader range of situations. This allows the models to be used more generally than with descriptive models. However, for specific situations descriptive models can be more accurate.

The constitutive model used in this thesis is NorSand (Jefferies, 1993). NorSand is an idealised constitutive model based on critical state theory. Before the model parameters and equations are presented a general description of constitutive models and the theoretical framework upon which the model is built are discussed.

2.2.2 General features of constitutive models

Generally speaking, constitutive models are often constructed in the same way and therefore often have similar features. How these features are defined is specific for each constitutive model and is what makes them unique. Before discussing particular constitutive models in more detail, a general explanation of these features is presented.

The two sources used in this Section are the personal communication of Brinkgreve (2019), and the Anura3D scientific manual from Ceccato et al. (2019).

Strain decomposition

The basic principle of elastoplasticity is to divide the total strain experienced by the soil in two components during yielding: an elastic component and a plastic component. By definition elastic strains are recoverable and plastic strains are not. This decomposition of the total strain is according to Eq. 2.3.

$$\varepsilon = \varepsilon^e + \varepsilon^p \tag{2.3}$$

Yield function

The yield function F is a function which determines if elastic or plastic strains occur. The yield function is a function of stress and optionally other parameters. The yield function must have the following condition: $F \leq 0$. Stress conditions where $F = 0$ can be viewed as a border in the stress space. This is called the yield surface or yield contour. An example of what a yield surface could look like is shown in Figure 2.7.

A material with a stress state within the yield surface behaves elastically. When the stress state is on top of the yield surface, plastic strains are developed. It is impossible to have a stress state outside the yield surface. During the development of plastic strains the stress state must remain on top of the yield contour, this is called the consistency condition. In summary, elastic or plastic strains develop as follows:

$F < 0$	Elastic behaviour
$F = 0$ & $dF < 0$	Unloading from a plastic state, which is elastic behaviour
$F = 0$ & $dF = 0$	Plastic behaviour

Flow rule

The flow rule describes the plastic strain rates. It is defined by the plastic potential function G. The derivative of G with respect to stress gives the direction of the plastic strain. The magnitude of the plastic strain rates is defined by the plastic multiplier Λ, consisting of hardening terms. Eq. 2.4 shows how plastic strain rates are calculated.

$$d\varepsilon^p = \Lambda \frac{\partial G}{\partial \sigma'} \tag{2.4}$$

Two types of flow rules exist:

1. Associated flow rule: the plastic potential function is the same as the yield function ($G = F$). What follows is that the plastic strains develop in the direction $\partial F/\partial \sigma'$. The normal to the yield surface is also in the direction $\partial F/\partial \sigma'$, hence the plastic strain increment vector is normal to the yield surface. This is called the normality principle. An example of the normality principle is shown in Figure 2.7.

2. Non-associated flow rule: the plastic potential function is not the same as the yield function ($G \neq F$). The plastic strain increment vector is therefore not normal to the yield surface.

Consistency condition

As already briefly touched upon, the consistency condition states that during the generation of plastic strains the stress state must remain on top of the yield surface. In other words, $F = 0$ and must remain zero so that $dF = 0$. By knowing that $dF = 0$, the yield function can be partially differentiated with respect to the variables defining the yield function using the chain rule. As a result the plastic multiplier Λ of Eq. 2.4 can be expressed in terms of the derivatives of yield function variables.

Hardening law

The yield surface is not fixed in stress space. This makes sense, as an increase in stresses in the presence of plastic strains must result in an expansion of the yield surface because of the consistency condition. Similarly, a decrease in stress state during plastic straining results in a shrinkage of the yield surface. The expansion of the yield surface is called hardening, the shrinkage of the yield surface is called softening.

The hardening law is a general term which describes both hardening and softening. It controls the evolution of the yield surface and is a function of plastic strains $(\partial F/\partial \varepsilon^P)$. The hardening law can consist of hardening parameters, defining the hardening or softening process.

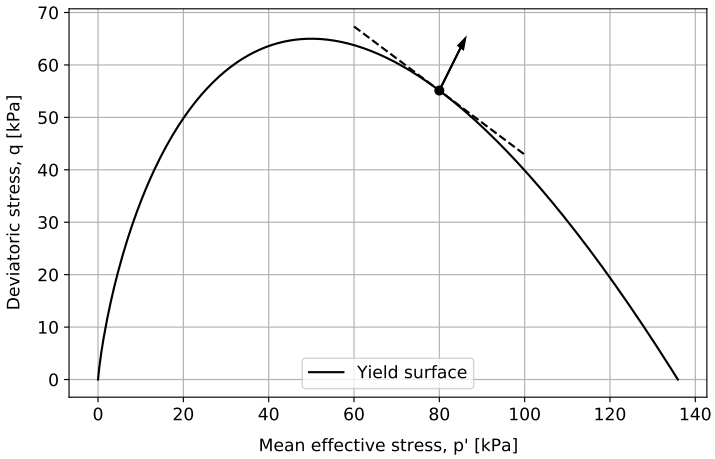

Figure 2.7: Example of what a yield surface can look like. The direction of the plastic strain increment is indicated with the arrow. In this example an associated flow rule is used because the plastic strain increment vector is normal to the yield surface. Also notice that the consistency condition is maintained because the stress state is on top of the yield surface during plastic shearing.

2.2.3 Critical state theory

Before discussing any constitutive model in detail it is interesting to look at the underlying principles upon which the models are built. This Section provides a description of soil mechanics in which the critical state plays a central role. This forms the basis of the constitutive models that will be discussed later.

Dilatancy and critical state

One of the aspects that distinguishes soil from other engineering materials is that it changes its volume when sheared. If a soil is initially dense it increases in volume, if it is initially loose the volume decreases. This tendency of soils to change its volume is called dilatancy and has been known for a long time, as it was first reported in the late 19th century by Reynolds (1885).

It was discovered by Casagrande (1936) that if a sand is sheared in a dense or loose state, it will dilate or contract respectively, until the same void ratio is reached at large strains. This void ratio is called the critical void ratio. The term critical state is derived from the critical void ratio. Roscoe et al. (1958) defined the critical state as the state of soil where unlimited deformation can take place while stress and void ratio remain constant. In this definition of the critical state two important criteria are named:

1. At the critical state the dilatancy is zero $(D = 0)$;
2. At the critical state the rate of change of dilatancy is zero $(\dot{D} = 0)$.

If one of these two criteria is not met, the critical state has not been achieved yet.

The void ratio at critical state is affected by the mean effective stress. It decreases with increasing stress levels. The relationship between the critical void ratio and the mean effective stress is called the critical state locus (CSL). The CSL is commonly formulated as a semi-log function shown in Eq. 2.5

$$e_c = \Gamma - \lambda \ln(p') \tag{2.5}$$

where Γ is the altitude of the CSL at 1 kPa, λ is the slope of the CSL. Both Γ and λ are intrinsic soil parameters. p' is the mean effective stress. An example of what this CSL formulation looks like in e-p' space is shown in Figure 2.9.

Although the semi-log expression of Eq. 2.5 is often acceptable as an approximation to describe the CSL, it is not by definition the way to express the CSL. Different expressions of the CSL exist. An example of a different formulation of the CSL follows from tests performed on Toyoura sand, where a curvature was introduced in the CSL expression to better fit the data (Verdugo, 1992). The validity of the CSL as a frame of reference does not depend on one single expression of the CSL. Rather, the expression of the CSL can be considered to be a modelling detail where it is important that the CSL describes a particular soil adequately (e.g. fits well to lab data) (Jefferies & Been, 2016).

Traditionally, one way to account for density effects in geotechnical practise was to change soil properties based on whether the soil is in a dense or loose state (e.g. use a higher value of ϕ' for a sand in a dense state than in a loose state). However, strictly speaking this is incorrect, because intrinsic soil properties are not a function of density. It is important to recognise that soil is a material that can exist over a range of different states. As a result, engineering behaviour (e.g. stress and stiffness) is determined by the combination of the soils state and intrinsic properties (Jefferies & Been, 2016). The theoretical development of capturing the density of a soil as a state variable and considering volume changes during shearing has become known as Critical State Soil Mechanics (CSSM), first put forward by lecturers at Cambridge University Schofield and Wroth (1968).

Stress-dilatancy

The fact that denser sand has more strength than looser sand led to the idea to separate the strength component due to friction from the dilatancy component. The first mathematical formulation of this idea was formulated by Skempton and Bishop (1950), who used work increments to formulate soil strength.

Consider a shear box test (see Figure. 2.8). Let σ_n be the normal stress, τ be the shear stress, and τ_d be the shear stress required to let the sample dilate. For an incremental horizontal displacement of δ_Δ the work performed against the normal stress is shown in Eq. 2.6. The frictional shear stress is denoted as τ_f and is defined as $\tau_f = \tau - \tau_d$. The shear strength can then be formulated according to Eq. 2.7. Notice that Eq. 2.7 clearly consists of the frictional and dilatancy component.

$$\sigma_n \delta_V = \tau_d \delta_\Delta \tag{2.6}$$

$$\frac{\tau}{\sigma_n} = \frac{\tau_f}{\sigma_n} + \frac{\delta_V}{\delta_\Delta} \tag{2.7}$$

In Figure 2.8 illustrative results of a shear box test are shown. The frictional component develops to an almost constant value. The dilatancy component evolves with shear strain. Volume expansion leads to an increase in shear strength, while volume contraction results in a shear strength decrease.

Later, Rowe (1962) related the mobilised stress ratio to plastic strain rates. This was called stress-dilatancy. The essence of stress-dilatancy is that it recognises dilation as a work transfer mechanism between principal stresses. Also note the strong analogy with how Skempton and Bishop (1950) formulated shear strength development in a shear box earlier.

A quantification of dilatancy is defined as the ratio between the two work conjugate strain increments, the volumetric strain ε_v and deviatoric strain ε_q (Jefferies & Been, 2016), shown in Eq. 2.8.

$$D = \frac{\dot{\varepsilon}_v}{\dot{\varepsilon}_q} \tag{2.8}$$

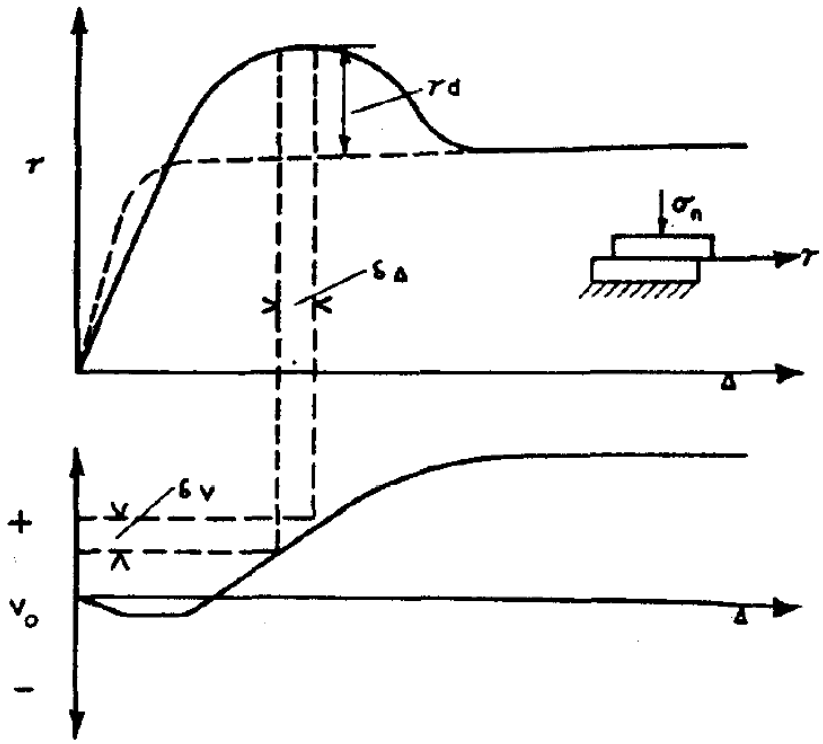

Figure 2.8: Illustration of the frictional and the dilatancy components of shear strength. The dashed line represents the frictional shear strength. The solid line is the shear strength consisting of the frictional and dilatancy components. Adopted from Skempton and Bishop (1950).

Critical friction ratio

So far the critical state has been expressed in the e - p space. The critical state is also associated with a particular stress ratio. The stresses at critical state are expressed in Eq. 2.9. Eq. 2.9 shows the magnitude of the deviator stress needed to keep the soil flowing as a function of the critical friction ratio M (Schofield & Wroth, 1968).

$$M = \frac{q_c}{p'_c} \tag{2.9}$$

A similarity exists between the critical state friction ratio and the critical friction angle ϕ_c, as both parameters represent critical state. Eq. 2.10 shows the relation between M and ϕ_c for triaxial compression conditions.

$$M_{tc} = \frac{6\sin(\phi_c)}{3 - \sin(\phi_c)} \tag{2.10}$$

It is relevant to specify the condition in which M is determined because M varies with different magnitudes of principal stresses relative to one another. The type of loading is relevant to describe M, which is accomplished by the Lode angle θ. The Lode angle ranges from +30° for triaxial compression to -30° for triaxial extension. It follows that M is a function of θ to give a general description of the critical friction ratio, where M_{tc} is a soil property used as input. Various expression for $M(\theta)$ have been developed in literature. An example proposed by Jefferies and Shuttle (2011) is shown in Eq. 2.11.

$$M(\theta) = M_{tc} - \frac{M_{tc}^2}{3 + M_{tc}} \cos\left(\frac{3\theta}{2} + \frac{\pi}{4}\right) \tag{2.11}$$

State parameter

With the soil state playing an important role in soil behaviour, it is important to be able to measure the soil state. The relative density of a sand is an example of how the state of a soil can be measured. Between a minimum and maximum void ratio, the relative density D_R is a measure of the state of sand between these two values, mathematically represented in Eq. 2.12.

$$D_R = \frac{e_{max} - e}{e_{max} - e_{min}} \tag{2.12}$$

A shortcoming of relative density is that it does not account for the stress level. At high confining stress levels dilatancy has a tendency to be suppressed. This is because at high pressure the crushing of grain contacts reduces the degree of interlocking (Rowe, 1962). A sand with a high relative density, but at a high confining stress will behave like a loose sand (Been & Jefferies, 1985).

Instead of using e_{max} and e_{min} as reference states, the critical state can be defined as the reference state for sands. The distance of a sand from this reference state in void ratio - stress space can be defined as the state of the sand. A new parameter called the state parameter, represented with the symbol ψ, is introduced to define this new state measure (Been & Jefferies, 1985). Eq. 2.13 shows the definition of the state parameter. A visual definition of ψ in void ratio - stress space is shown in Figure 2.9.

$$\psi = e - e_c \tag{2.13}$$

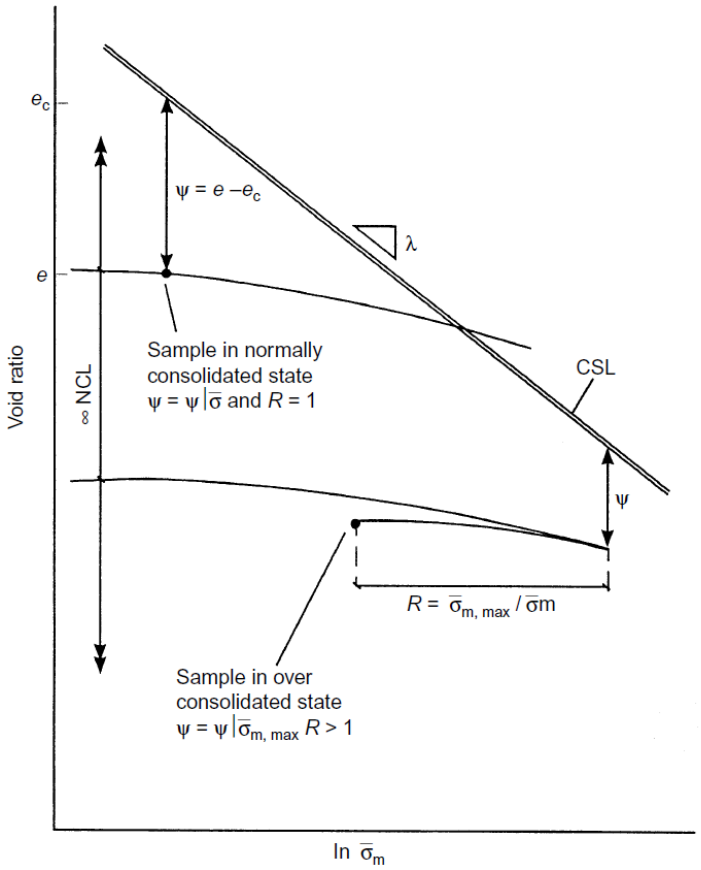

Figure 2.9: Definition of state parameter and overconsolidation ratio in void ratio - stress space. Adopted from Jefferies and Shuttle (2002).

By using ψ, the stress level is taken into consideration when assessing a sand's state because the CSL is dependent on the stress level as can be clearly seen in Eq. 2.5 and Figure 2.9.

Figure 2.10 demonstrates that samples with similar relative densities can show completely different stress paths, whereas samples with a similar state parameter show similar behaviour.

Beside being an improvement of measuring the state of a sand, the state parameter is also a fundamental parameter to capture density effects in constitutive models such as NorSand (Jefferies & Been, 2016).

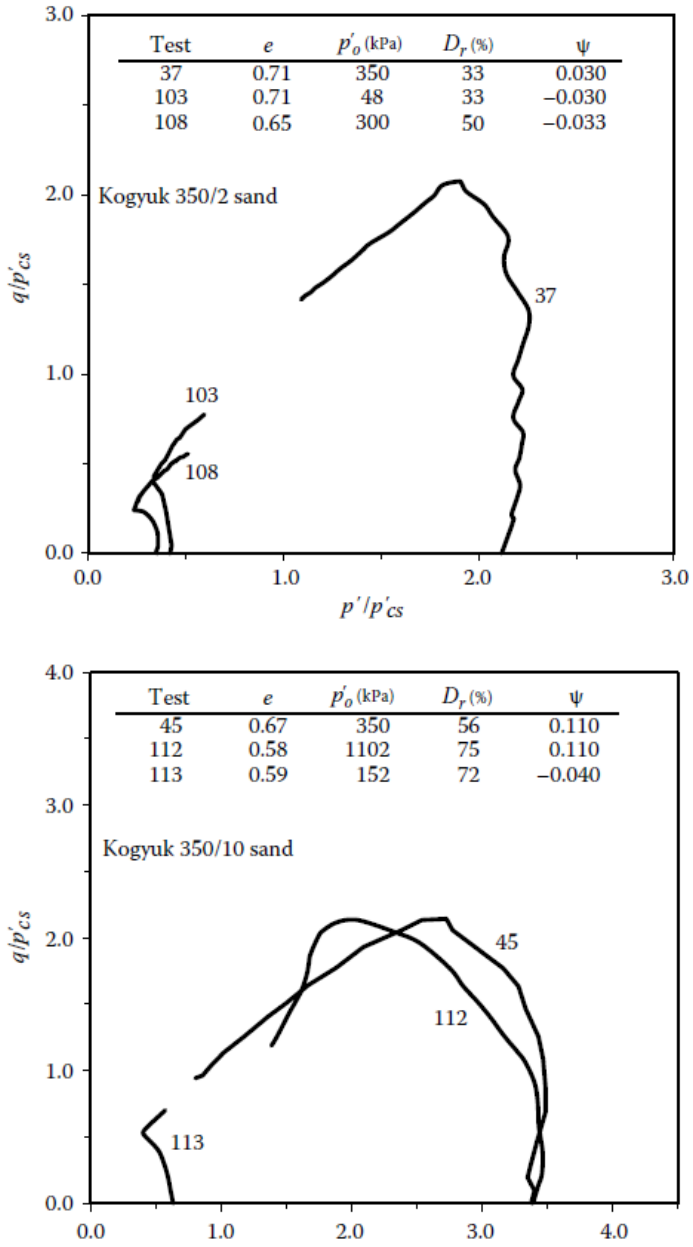

Figure 2.10: Stress paths of undrained triaxial tests on Kogyuk 350/2 and Kogyuk 350/10 sand. Adopted from Jefferies and Been (2016).

Soil property χ

The state parameter allows for the introduction of a new soil property χ. When the state parameter was first introduced by Been and Jefferies (1985) it was thought that a unique relationship existed between D_{min} and ψ_0 (notice that D_{min} here means maximum dilation as dilatancy is negative by convention). When the state parameter was introduced to soils with a broader particle size distribution (PSD) than sand, it became apparent that a soil property relating the state parameter to the maximum dilatancy was involved. This soil property is χ_{tc} (subscript "tc" meaning that it is determined under triaxial compression conditions), relating D_{min} to ψ according to Eq. 2.14 (Jefferies & Been, 2016).

$$D_{min} = \chi_{tc}\psi \tag{2.14}$$

In Eq. 2.14, ψ is the current state parameter (so the value of ψ at which D_{min} occurs). At $\psi = 0$ it follows that $D_{min} = 0$, which is the critical state.

Introducing χ_{tc} improves the accuracy of relating the state parameter to maximum dilation, although it comes at the cost of more complex processing of laboratory tests.

Image condition

One of the findings of Rowe (1962) was that the operating friction angle during shear was not the grain to grain friction ϕ_u, but rather friction angle ϕ_f with $\phi_u \leq \phi_f \leq \phi_c$. This operational friction angle (or friction ratio M) can also be referred to as the image friction angle (or image friction ratio M_i).

The image condition is the condition where $D^p = 0$, but the second requirement of obtaining critical state ($\dot{D}^p = 0$) is not met. When dense sands are sheared they typically first show contractive behaviour as a result of elastic deformation before expanding in volume. At the transition between contraction and dilation, $D^p = 0$, which is the image condition because afterwards the sand will dilate and $D^p \neq 0$ (Jefferies & Been, 2016).

The image condition evolves with strain and moves to the critical state which is formally shown in Eq. 2.15

$$M_i \Rightarrow M \text{ as } \psi \Rightarrow 0 \tag{2.15}$$

There is not one definitive relation relating M_i to M and several have been proposed in literature. The only condition for a definition of M_i must be that the condition in Eq. 2.15 is met.

It turns out that using an operational friction ratio can be useful in constitutive models as an evolving parameter based on ψ.

2.2.4 Original Cam Clay

The Original Cam Clay (OCC) model is one of the first constitutive models developed in the scope of CSSM. Its first description is formulated by Schofield and Wroth (1968). In essence, NorSand is a further development of the ideas of OCC. It is interesting to discuss OCC before looking at NS to compare the similarities and differences between the models.

Starting point of OCC is the relation between the normal compression locus (NCL) and the CSL, shown in Figure 2.11a. A single NCL exists and the CSL is parallel to the NCL, offset by a spacing ratio. Drucker et al. (1957) showed that the NCL must intersect the yield surface, because normal compression leads to irrecoverable strains. The NCL can be viewed as the hardening rule for yield surfaces invoking normality. Because of the parallel relation between the CSL and NCL in OCC, this means that the size of the yield surface is linked to the CSL in OCC.

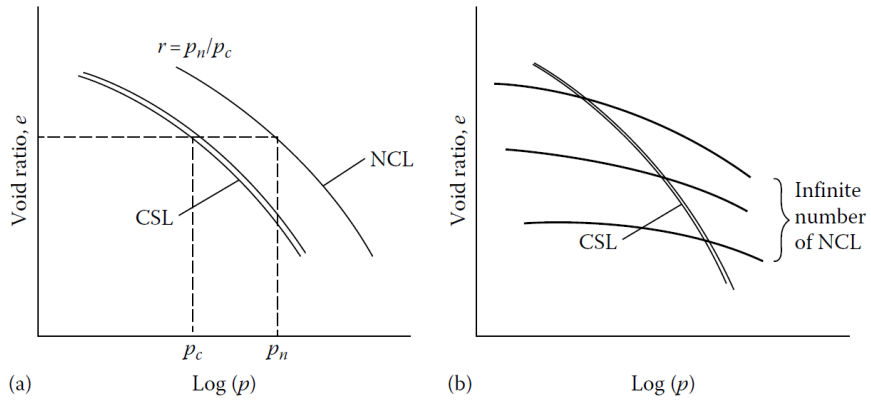

Figure 2.11: Idealisation of NCL compared to the CSL for (a) OCC and (b) NorSand. Adopted from Jefferies and Been (2016).

Flow rule

The flow rule of OCC follows from the idea that shear strength of soil consists of the two components as described in Eq. 2.7. From the idealisation that stress-dilatancy is a work transfer mechanism between principal stresses, the rate of work on a soil element per unit volume is according to Eq. 2.16.

$$\dot{W} = q\dot{\varepsilon}_q + p'\dot{\varepsilon}_v \tag{2.16}$$

Only the plastic work is of interest because elastic strains are recoverable. Strain decomposition allows the plastic work to be written as

$$\dot{W}^p = \dot{W} - \dot{W}^e = q\dot{\varepsilon}_q^p + p'\dot{\varepsilon}_v^p \tag{2.17}$$

Next, $\dot{W}^p$ is divided by the mean effective stress to make it dimensionless, and by the rate of plastic deviatoric strain to normalise the rate of work per unit plastic distortion of the soil.

$$\frac{\dot{W}^p}{p\dot{\varepsilon}_q^p} = \frac{\dot{\varepsilon}_v^p}{\dot{\varepsilon}_q^p} + \frac{q}{p'} = D^p + \eta \tag{2.18}$$

OCC assumes that the dimensionless rate of plastic work dissipation is the constant critical friction ratio M (Schofield & Wroth, 1968).

$$\frac{\dot{W}^p}{p'\dot{\varepsilon}_q^p} = M \tag{2.19}$$

The flow rule is then given by substituting Eq. 2.19 in Eq. 2.18 resulting in

$$D^p = M - \eta \tag{2.20}$$

Yield surface

The OCC yield surface follows from two assumptions: the flow rule from Eq. 2.18 and the normality condition belonging to an associated flow rule. From the definition of the stress ratio $q = \eta p'$, the change in shear stress is obtained

$$\dot{q} = p'\dot{\eta} + \eta\dot{p}' \tag{2.21}$$

The normality condition states that the plastic strain increment vector is perpendicular to the tangent on the yield surface. The tangent to the yield surface is $\dot{q}/\dot{p}'$. Knowing the plastic strain increment vector is $\dot{\varepsilon}_q^p/\dot{\varepsilon}_v^p$, the following expression is obtained from normality

$$\frac{\dot{q}}{\dot{p}'} = \frac{-1}{\dot{\varepsilon}_q^p/\dot{\varepsilon}_v^p} = -D^p \tag{2.22}$$

Substituting Eq. 2.21 in Eq. 2.22 results in

$$\frac{\dot{p}'}{p'} + \frac{\dot{\eta}}{D^p + \eta} = 0 \tag{2.23}$$

After integration of Eq. 2.23 and determining the integration constant at the critical state $\eta = M$, the final form of the yield surface is shown in Eq. 2.24.

$$\frac{\eta}{M} = 1 - \ln\left(\frac{p'}{p_c'}\right) \tag{2.24}$$

Here p_c' is the mean effective stress at critical state.

Hardening law

The hardening law of OCC arises from one of the key ideas of OCC, namely that all yield surfaces intersect with the CSL. Volumetric strain affects the yield surface size by changing the critical void ratio (Jefferies & Been, 2016).

An insightful way to illustrate the hardening law is to look at an idealisation of a compression test. In Figure 2.12, consider point A located on the CSL. Now let the soil consolidate along the CSL to point B. At point B the soil is unloaded. Part of the void ratio change will be recovered, whereas the plastic void ratio change is not recovered (indicated in Figure 2.12). The incremental change of plastic void ratio can then be expressed as follows

$$\dot{e}^p = -(\lambda - \kappa)\frac{\dot{p}_c'}{p_c'} \tag{2.25}$$

where p_c indicates the mean effective stress at the critical state, and κ is the slope of the unloading branch of the NCL.

According to Eq. 2.26, transforming the incremental void ratio change to an increment in volumetric strain results in the hardening law of Eq. 2.27. The term $(1+e)/(\lambda - \kappa)$ is a dimensionless hardening modulus.

$$\dot{e}^p = -(1+e)\dot{\varepsilon}_v^p \tag{2.26}$$

$$\frac{\dot{p}_c'}{p_c'} = \frac{(1+e)}{(\lambda - \kappa)}\dot{\varepsilon}_v^p \tag{2.27}$$

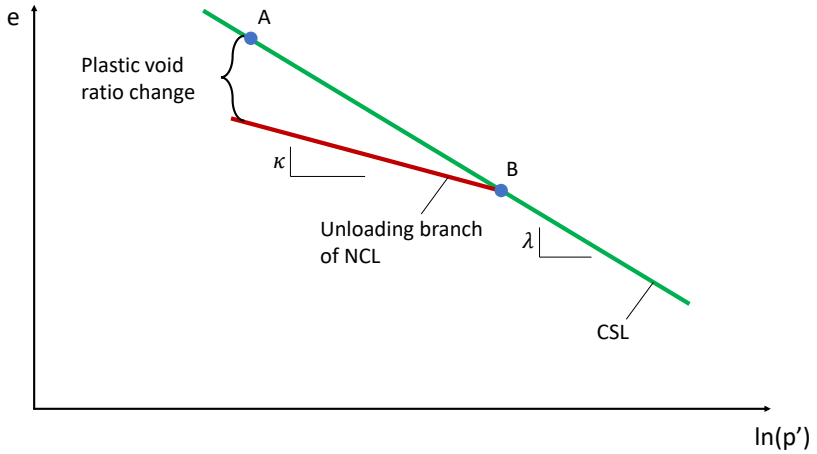

Figure 2.12: Illustration of plastic void ratio change using loading and unloading in ln(p')-e space.

Eq. 2.27 shows that the evolution of the yield surface is controlled by the plastic volumetric strain. A positive value of $\dot{\varepsilon}_v^p$ means a volume decrease (compaction) also resulting in a positive $\dot{p}_c$, which leads to an expansion of the yield surface. The opposite happens for negative values of $\dot{\varepsilon}_v^p$ when dilatancy occurs.

2.2.5 NorSand

Problems when modelling dense sand with OCC

Before discussing NorSands equations, it is interesting to discuss a fundamental shortcoming of OCC. OCC is known for its inability to accurately model dense sands. This leads back to the idealisation of OCC that the NCL is parallel to the CSL, shown in Figure 2.11a.

Consider Figure 2.13. From introducing the state parameter, it follows that the ratio p_c/p can be expressed as in Eq. 2.28. The ratio p_n/p_c follows from the shape of the yield surface. At the NCL isotropic compression conditions are present, i.e. $q = 0 \Rightarrow \eta = 0$. Substituting in the OCC yield surface equation (Eq. 2.24) results in the ratio as shown in Eq. 2.29. Combining Eq. 2.28 and 2.29 results in a formulation of the overconsolidation ratio R as in Eq. 2.30.

$$\frac{p'_c}{p'} = \exp\left(\frac{-\psi}{\lambda - \kappa}\right) \tag{2.28}$$

$$\frac{p'_n}{p'_c} = 2.718 \tag{2.29}$$

$$R = 2.718 \cdot \exp\left(\frac{-\psi}{\lambda - \kappa}\right) \tag{2.30}$$

It is common for sand samples to be as dense as $\psi < -0.2$. Reasonable values for the other parameters at that state are $\lambda = 0.02$ and $0.1\lambda < \kappa < 0.4\lambda$ (Jefferies & Been, 2016). It follows that using parameter inputs of these magnitudes results in a very large overconsolidation ratio of $R > 10^5$. This would imply very high strength and only elastic behaviour for stress ratios in triaxial tests, whereas it is known from testing that plastic strains are generated from the start of loading.

The problem lies with the idealisation of the NCL of OCC. Ishihara et al. (1975) was first to argue that sand samples can be compacted to any initial density between their respective e_{min} and e_{max}. When the samples are then subjected to stress, plastic yielding would arise from the beginning. Therefore, an infinite number of virgin states exist for sand, resulting in an infinite number of NCL between the minimum and maximum densities. This concept is shown in Figures 2.11b and 2.9. Experimental evidence presented in Jefferies and Been (2016) confirms the existence of an infinite number of NCL for sands.

With an infinite number of NCL, it becomes necessary to use two parameters to define the state of a sand. The state parameter is a measure of which individual NCL is applicable. The overconsolidation ratio defines the proximity of a state relative to the yield surface. In Figure 2.9 it is shown how the two parameters represent the state of a sand in e-p space.

With abandoning the OCC idealisation that the NCL and CSL are parallel, the size of the yield surface is decoupled from the CSL. The premise of Drucker et al. (1957) that the NCL presents the hardening rule for associated plasticity models is still applicable, only the description of the NCL and its relation with the CSL has changed.

NorSand adopts the concept of an infinity of NCL. The CSL provides a reference state and is still unique and based on intrinsic soil properties. The state parameter ψ functions like a rate variable. The further away from the final state (critical state), the faster state changes occur (Jefferies & Been, 2016).

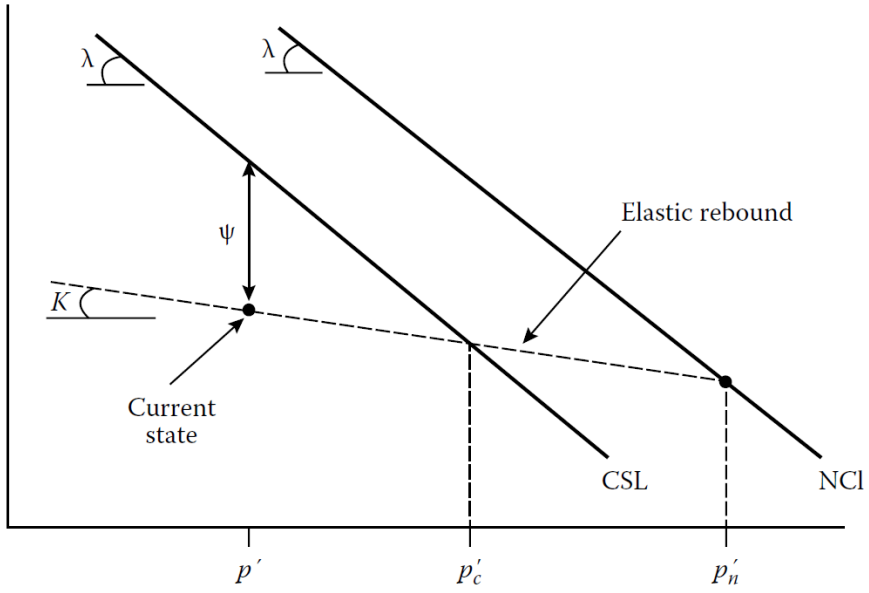

Figure 2.13: Idealisation of OCC. Unloading from the NCL combined with the definition of the state parameter. Adopted from Jefferies and Been (2016).

Volumetric coupling parameter N

NorSand introduces a parameter that is not present in OCC, namely the volumetric coupling parameter N. The parameter N was first introduced by Nova (1982) as cited in Jefferies (1997), shown in Eq. 2.31. Rewriting Eq. 2.31 results in the energy balance shown in Eq. 2.32.

$$D^p = \frac{\dot{\varepsilon}_v^p}{\dot{\varepsilon}_q^p} = \frac{M - \eta}{1 - N} \tag{2.31}$$

$$q\dot{\varepsilon}_q^p + p'\dot{\varepsilon}_v^p = Mp'|\varepsilon_q^p| + Np'\dot{\varepsilon}_v^p \tag{2.32}$$

The term $Mp'|\varepsilon_q^p|$ is the frictional dissipation term from Schofield and Wroth (1968) (see also Eq. 2.17 and 2.19 from OCC). The term $Np'\dot{\varepsilon}_v^p$ represents an inelastic storage term. Test data shows that upon the unloading of dense sand samples a portion of the volumetric strain is recovered. The inelastic storage term becomes negative as $\dot{\varepsilon}_v^p$ becomes negative when the sample changes from contraction to dilation (Jefferies, 1997). Notice that one of the idealisations of OCC is the work dissipation of Eq. 2.19, which is the case $N = 0$ in Eq. 2.31.

NorSand internal variables

In NorSand many parameters revolve around the image condition (see Section 2.2.3). NorSand describes many of the previously discussed soil variables in terms of this image condition. These parameters will be called "internal parameters", as the parameters in itself are not new, but the way they are related to the image condition in NorSand is.

The image state parameter is looked into first, which is according to Eq. 2.33. Here e_i is the critical state void ratio at the image mean effective stress p'_i.

$$\psi_i = e - e_i \tag{2.33}$$

The parameter χ_{tc} can also be expressed in terms of the image condition. The maximum dilatancy would then be according to Eq. 2.34. It must be noted that this maximum dilatancy must be equal to the one previously defined with χ_{tc} in Eq. 2.14, so Eq. 2.35 follows. Here the term ψ_{Dmin} is used to emphasise that this is the state parameter at maximum dilatancy.

$$D_{min} = D^p_{min} = \chi_i \psi_i \tag{2.34}$$

$$\chi_i \psi_i = \chi_{tc} \psi_{Dmin} \tag{2.35}$$

When the linear CSL idealisation is used (Eq. 2.5) it follows that

$$e_{c,i} - e_{c,Dmin} = \Gamma - \lambda \ln(p'_i) - \Gamma + \lambda \ln(p'_{Dmin}) = -\lambda \ln \left(\frac{p'_i}{p'} \right)_{max} \tag{2.36}$$

The state parameter at D_{min} can then be expressed as follows

$$\psi_{Dmin} = \psi_i - \lambda \ln \left(\frac{p'_i}{p'} \right)_{max} \tag{2.37}$$

The term $(p_i/p)_{max}$ is the internal hardening limit of Eq. 2.44. Substitution of the hardening limit in Eq. 2.37 results in

$$\psi_{Dmin} = \psi_i \left(1 + \frac{\chi_i \lambda}{M_i} \right) \tag{2.38}$$

Now, substitution of Eq. 2.38 in Eq. 2.35 results in an expression of the internal NorSand variable χ_i of

$$\chi_i = \chi_{tc} / \left(1 - \frac{\lambda \chi_{tc}}{M_i}\right) \tag{2.39}$$

In Eq. 2.39, M_i is dependent on χ_i. Strictly speaking an additional solving procedure is required to solve for χ_i. Considering the accuracy at which soil properties are determined it is justified to use a simplification to determine χ_i, which is shown in Eq. 2.40 (Jefferies & Been, 2016).

$$\chi_i = \chi_{tc} / \left(1 - \frac{\lambda \chi_{tc}}{M_{tc}}\right) \tag{2.40}$$

In Eq. 2.40, λ represents the slope of the log-linear CSL of Eq. 2.5 which is commonly used to describe the CSL. If a different formulation of the CSL is used the λ term has to be adjusted such that it is still in a linear equivalent form.

Flow rule

NorSand uses a flow rule similar to OCC. The crucial difference is that instead of the critical friction ratio M used in OCC, NorSand uses the operational friction ratio at the image condition M_i. NorSands flow rule is shown in Eq. 2.41.

$$D^p = M_i - \eta \tag{2.41}$$

Here the operational friction ratio M_i is shown in Eq. 2.42. This expression is obtained by substituting Nova's flow rule of Eq. 2.31, NorSands flow rule of Eq. 2.41 and a generalised version (meaning a dependency on the Lode angle θ) of the maximum dilatancy of Eq. 2.34.

The reason an absolute value of ψ_i is used is to make M_i symmetric and applicable to both dense and loose sands. This is because Eq. 2.34 is only applicable to initially dense sands, because loose sands show no dilative behaviour. Another thought was to use $M_i = M(\theta)$ for loose sands and only use M_i for dense sands. However, the symmetric version of Eq. 2.42 shows the best agreement with experimental results (Jefferies & Been, 2016).

$$M_i = M(\theta)\left(1 - \frac{\chi_i N}{M_{tc}} |\psi_i|\right) \tag{2.42}$$

Yield surface

The yield surface is derived in a similar fashion to OCC. From the normality condition of Eq. 2.22, subsequent integration results in the NorSand yield surface as shown in Eq. 2.43.

$$\frac{\eta}{M_i} = 1 - \ln\left(\frac{p'}{p'_i}\right) \tag{2.43}$$

The size of the yield surface is controlled by the mean effective stress at the image state p'_i.

Hardening law

The NorSand yield surface has an inner cap which limits the maximum dilation. Recall that the maximum dilatancy is according to Eq. 2.34. When substituted in the yield surface of Eq. 2.43 it follows that the limit p'_i is defined as

$$\left(\frac{p'_i}{p'}\right)_{max} = \exp\left(-\frac{\chi_i \psi_i}{M_i}\right) \tag{2.44}$$

The hardening law follows from the proposition that all states move towards the critical state with enough deviatoric strain, formally shown as

$$\psi \Rightarrow 0 \text{ as } \varepsilon_q \Rightarrow \infty \tag{2.45}$$

The change in image mean effective stress then becomes

$$\dot{p}'_i = H(p'_{i,max} - p'_i)\dot{\varepsilon}_q \tag{2.46}$$

It is more appropriate to make the hardening law dimensionless, which is shown in Eq. 2.47. The derivation of Eq. 2.47 from 2.46 can be found in Jefferies and Been (2016).

$$\frac{\dot{p}'_i}{p'_i} = H\left(\frac{p'}{p'_i}\right)^2\left[\exp\left(-\frac{\chi_i\psi_i}{M_i}\right) - \frac{p'_i}{p'}\right]\dot{\varepsilon}_q \tag{2.47}$$

The parameter H is the hardening modulus and is a soil parameter. An additional hardening modulus is required because the decoupling of the CSL with the yield surface means that the slope of the CSL cannot longer function as the hardening modulus (as was the case for OCC). H must be determined by calibrating to experimental data.

Elasticity

NorSand adopts isotropic elasticity. A basic form of elasticity is used which consists of a dimensionless shear rigidity parameter I_r and a constant Poisson's ratio ν. I_r is defined in Eq. 2.48.

$$I_r = \frac{G}{p'} \tag{2.48}$$

To account for the void ratio and stress dependency of the stiffness, the shear modulus G is often expressed as the empirical equation of Eq. 2.49 (Yang & Liu, 2016). In Eq. 2.49 F(e) is a function dependent on the void ratio. p_a is the atmospheric pressure. A and n are best-fit parameters.

$$G = AF(e)\left(\frac{p'}{p_a}\right)^n \tag{2.49}$$

From the shear modulus G, the bulk modulus K can be computed according to Eq. 2.50.

$$K = \frac{2(1+\nu)}{3(1-2\nu)}G \tag{2.50}$$

2.2.6 Constitutive model for the modelling of a CPT

The modelling of a CPT has previously been studied using the Anura3D software.

Schuringa (2020) conducted a master's thesis using a Mohr-Coulomb Strain Softening (MCSS) constitutive model. The MCSS model is an alteration of the traditional Mohr-Coulomb (MC) model. MC is an elastic-perfectly plastic model which is not able to model a peak and residual strength. In MCSS the model parameters of MC are changed such that a peak and residual strength can be modelled by introducing a softening term (Ceccato et al., 2019). When modelling a CPT both large and small displacements occur in the domain. For small displacements the peak strength governs soil behaviour, whereas for large strains the critical state is normative. Therefore, MCSS is an improvement over MC when modelling a CPT using the MPM. However, even with the addition of softening it was concluded that the MPM with MCSS is not able to accurately model a CPT. MCSS is still a simple constitutive model which does not

accurately capture the behaviour of a sand. This can be attributed to the fact that the model does not account for density effects, has no stress-dependency of stiffness and cannot describe non-linear soil behaviour (Schuringa, 2020).

Martinelli and Galavi (2021) performed a study on the MPM modelling of a CPT using the Hardening Soil (HS) model. HS is a more advanced model compared to MC (or MCSS). It has the ability to model non-linear soil behaviour and has a stress-dependency on the stiffness. However, it lacks the ability to model softening and is state-independent. The study showed that with proper parameter calibration it is possible to achieve model results that are in agreement with experimental data. Although the parameter calibration results in an agreement between model and experimental results, the parameters used in HS can be contradictory to the actual testing conditions. Sand in a dense state ($D_R = 85\%$) where a volume expansion is expected is e.g. best modelled with a negative dilation angle in HS (Martinelli & Galavi, 2021).

A feature that is not incorporated in the elasticity formulation of NorSand is a strain dependency of the stiffness. At very small strains soils have the tendency to behave stiff. This stiffness decreases with increasing strains. When plotting the stiffness as a function of shear strains γ the stiffness reduction curve generally has a characteristic S-shaped form. When the small strain stiffness is used upon full strain reversal, hysteresis effects can be incorporated in the model. The incorporation of a strain-dependency of the stiffness is especially relevant in situations where very small strains are expected to be encountered such as in vibration problems or settlements at large distances from retaining walls. The strain-dependency is also relevant for dynamic applications because hysteresis leads to energy dissipation and damping (Brinkgreve, 2019). During a CPT, the small strain elastic stiffness has a minor influence as plastic shear strains dominate the soil behaviour after the initial loading due to the large strains involved (Jefferies & Been, 2016). Not including a strain-dependency of the stiffness is therefore not viewed as a major shortcoming. However, it could be interesting to implement a strain-dependency of the stiffness if it is desired to assess displacements at large distances from the cone, but this is outside the scope of this thesis.

NorSand has the potential to be the constitutive model which meets the requirements for accurate CPT modelling. The framework of CSSM on which the model is built allows for accurate modelling of peak and critical state soil behaviour. NorSand has a stress dependency on the stiffness and the incorporation of the state parameter ψ as a governing parameter ensures the state dependency of the model. The ability of NorSand to accurately model a CPT in dry sand will show from the results of this thesis.

In Figure 2.14 the different modelling capabilities of the four models are shown for a stress-strain curve on dense sand.

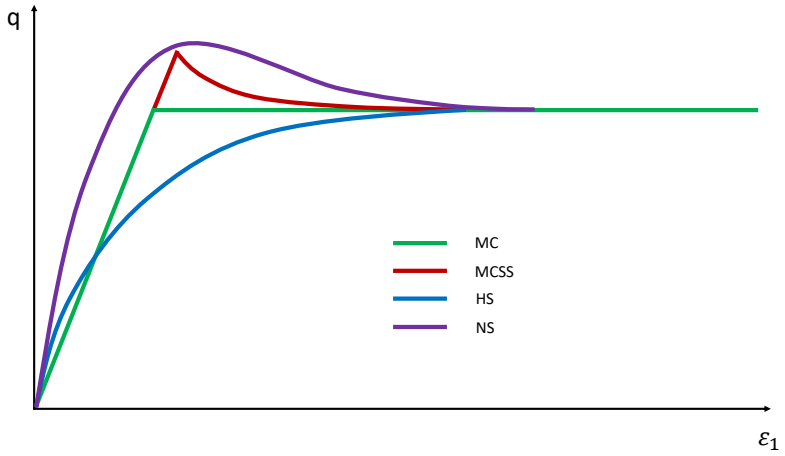

Figure 2.14: Example sketches of stress-strain curves of a drained triaxial test on dense sand for the four different constitutive models. Note: this sketch is purely for illustrative purposes and is only meant to show the different modelling capabilities of the four models. No calibration of the models to a specific sand has been performed and thus readable soil properties from this sketch should not be compared.

2.3 Compression model for cohesionless soils

In this Section the compression model developed by Pestana and Whittle (1995) is outlined. This compression model is used to calibrate CSL's to different types of sand in the absence of sufficient laboratory data (more on this in Chapter 4).

The goal of this part of the literature study is to provide background information on compression behaviour of sands and to familiarise the reader with the most relevant concepts and the input parameters of the compression model. A complete derivation of the model will not be provided. For this, the reader is referred to the paper of Pestana and Whittle (1995).

2.3.1 Model background

From experimental data it is known that freshly deposited sand samples which are compressed from different initial densities converge towards a unique void ratio - stress behaviour. This unique relation is called the Limit Compression Curve (LCC). The concept of the LCC is shown in Figure 2.15. The LCC is linear in log(e)-log(p′) space.

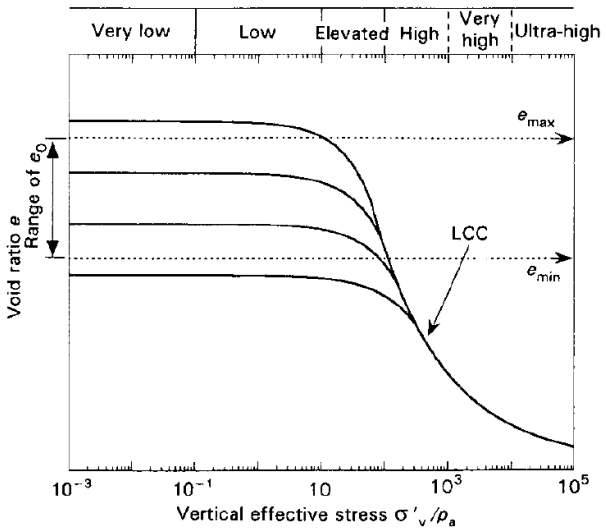

Figure 2.15: Concept of the LCC. Compression from different initial densities results in convergence towards the LCC. Adopted from Pestana and Whittle (1995).

There is consensus in literature that volume changes at low confining stress levels are due to elastic compression and particle rearrangements, whereas the LCC is governed by particle crushing. Generally speaking, compression behaviour of sands depends on many aspects (e.g. fabric, mineralogy, particle size distribution, angularity) (Pestana & Whittle, 1995). Capturing (most of) these aspects while maintaining a certain degree of simplicity is challenging. Nevertheless, this is accomplished by Pestana and Whittle (1995) who find that the developed compression model is able to provide a reliable description of compression behaviour with only four input parameters, which can be obtained from laboratory testing.

2.3.2 Hydrostatic compression formulation

The model distinguishes elastic and plastic strains and combines them later through strain decomposition similar to Eq. 2.3.

In a hydrostatic situation the unloading produces primarily elastic stains. The formulation used in the model assumes that hydrostatic unloading is elastic but non-linear. The increment of elastic volumetric strains is given by Eq. 2.51.

$$d\varepsilon^e = \frac{n}{C_b}\left(\frac{p'}{p_a}\right)^{-1/3}\frac{dp'}{p_a} \tag{2.51}$$

The term C_b is a constant defining the unloading behaviour and must be determined from laboratory testing.

When loading in the LCC regime occurs, plastic strains are developed. The volumetric plastic strain increment is according to Eq. 2.52.

$$d\varepsilon^p = n\left(\rho_c - \frac{(p'/p_a)^{2/3}}{C_b}\right)(1-\delta_b^{\theta_{pes}})\frac{dp'}{p'} \tag{2.52}$$

Here ρ_c is the slope of the LCC in log(e)-log(p') space. θ_{pes} is a constant exponent requiring $\theta_{pes} > 0$. δ_b is the distance between the current mean effective stress p' and the equivalent mean effective stress at the LCC p'_b at the same void ratio. This distance is calculated as

$$\delta_b = 1 - \frac{p'}{p'_b} \tag{2.53}$$

where the equivalent stress is

$$p'_b = p'_r\left(\frac{1}{e}\right)^{1/\rho_c} \tag{2.54}$$

The parameter p'_r is an input parameter defining the linearisation of the LCC, as it is the value of the mean effective stress of the LCC at a void ratio of $e = 1$.

Combining Eq. 2.51 and Eq. 2.52 through strain decomposition results in a complete description of the evolution of volumetric strains according to Eq. 2.55.

$$d\varepsilon = n\left[\frac{\delta_b^{\theta_{pes}}}{C_b(p'/p_a)^{1/3}} + \frac{\rho_c}{p'/p_a}(1-\delta_b^{\theta_{pes}})\right]\frac{dp'}{p_a} \tag{2.55}$$

Eq. 2.55 cannot be solved analytically and therefore requires a numerical solution.

2.3.3 One-dimensional compression formulation

Most compression data is acquired from one-dimensional (1-D) compression tests. There are quantitative differences between hydrostatic and 1-D compression. The LCC in 1-D compression (K_0-LCC) is parallel to the LCC in hydrostatic compression (H-LCC). At the same stress level the void ratio at the K_0-LCC is lower than for the H-LCC. This can be seen in Figure 2.16. An explanation for this is that there are shear stresses in 1-D compression. Shear stresses enhance particle crushing, causing a greater density at the same stress level.

Figure 2.16 implies that the only parameter that is affected when changing from hydrostatic to 1-D conditions is p'_r, which is changed to $p'_{r,1D}$. In 1-D compression tests the horizontal stress

is generally not measured. It is therefore convenient to write an expression in terms of the vertical effective stress σ'_v. The expression for 1-D compression is shown in Eq. 2.56.

$$d\varepsilon = n\left[\frac{[(1+2K_0)/3]^{2/3}}{C_b(\sigma'_v/p_a)^{1/3}}\delta_b^{\theta_{pes}} + \frac{\rho_c}{\sigma'_v/p_a}(1-\delta_b^{\theta_{pes}})\right]\frac{d\sigma'_v}{p_a} \tag{2.56}$$

Here, an approximation of δ_b as shown in Eq. 2.57 is sufficient.

$$\delta_b = 1 - \left(\frac{1+2K_0}{1+2K_{0NC}}\right)\frac{\sigma'_v}{\sigma'_{vb}} \approx 1 - \frac{\sigma'_v}{\sigma'_{vb}} \tag{2.57}$$

Compared to hydrostatic conditions the input parameter p'_r changes to σ'_{vr}. The equivalent stress at the K_0-LCC is then calculated according to Eq. 2.58.

An overview of all the different notations of σ'_v and what stress it represents is presented in Figure 2.17.

$$\sigma'_{vb} = \sigma'_{vr}\left(\frac{1}{e}\right)^{1/\rho_c} \tag{2.58}$$

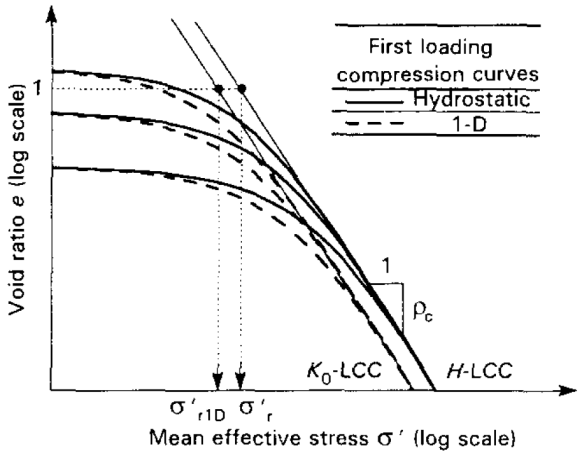

Figure 2.16: Comparison between hydrostatic LCC and one-dimensional LCC. Adopted from Pestana and Whittle (1995).

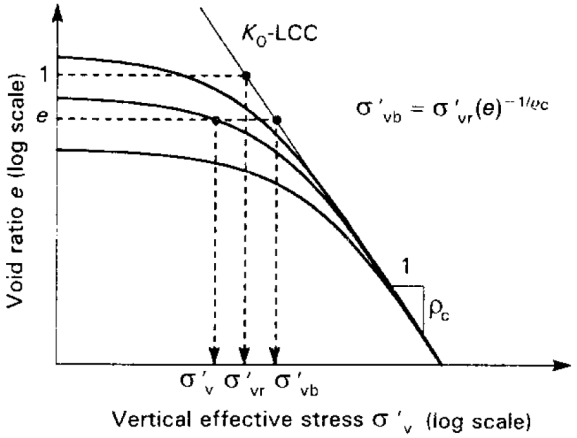

Figure 2.17: Overview of the different notations of σ'_v and what stress it represents. Adopted from Pestana and Whittle (1995).

3

Model Setup

In this Chapter the setup of the model is discussed. Various features of the model are explained which fall outside the literature study but are important to obtain a complete understanding of the model.

3.1 Domain description

3.1.1 Geometry

The geometry of the domain is drawn using the program GiD v14. Lines can be drawn, which define the domain and the geometry within. Between a closed group of lines a surface can be created. On lines and surfaces various aspects can be defined. On lines e.g. reaction forces and contact formulations, on surfaces e.g. mesh characteristics and type of material can be defined. A typical domain with a drawn geometry and defined surfaces is shown in Appendix A in Figure A.1.

3.1.2 Material layers

In the model four material layers are distinguished:

1. Soil layer: This layer represents the soil in the domain. The constitutive model used for this layer is NorSand.
2. Pile layer: This layer represents the CPT in the simulation. It is pushed into the soil layer with a constant speed. The layer is modelled as linear elastic with a Poisson's ratio of $\nu = 0.33$, which is common for most metals.
3. Surcharge layer: in Section 3.2 a more detailed description of the surcharge layer and its purpose in the model is provided.
4. Boundary layer: in Section 3.3 a more detailed description of the boundary layer and its purpose in the model is provided.

Figure 3.1 presents an overview of how the materials are defined in the domain.

3.1.3 Domain enlargement

It is possible to enlarge the domain. This is achieved by modifying the width of the area denoted with 'X' in Figure 3.1. The ability to enlarge the domain is useful to investigate the effects of the boundary conditions on modelling results (see Chapter 6).

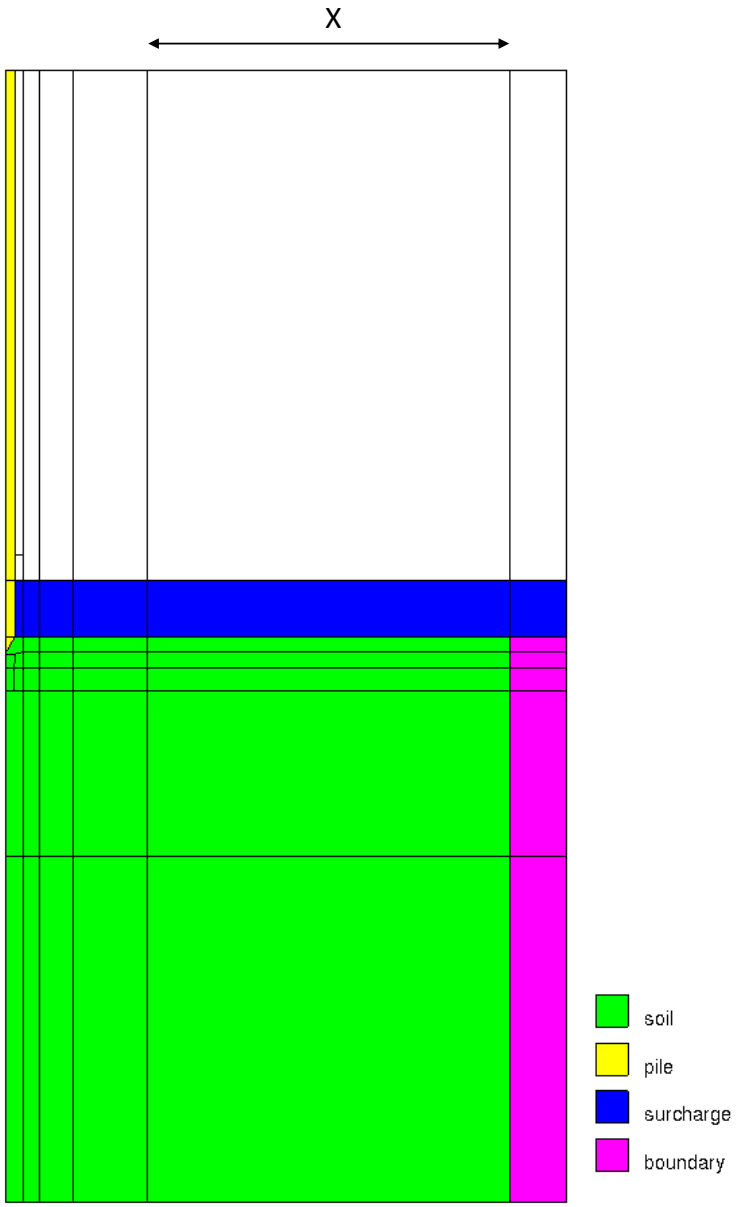

Figure 3.1: Overview of where the different materials are located in the domain.

3.2 Surcharge layer

In the model a surcharge layer is defined in order to simulate different initial vertical stress levels. The surcharge layer lies on top of the soil and is defined as a linear elastic material. Properties of the layer are shown in Table 3.1. A perfectly smooth contact is assumed between the surcharge layer and the CPT.

By changing the density of the surcharge layer the vertical effective stress at the top of the

soil layer is changed. In Eq. 3.1 it is shown how the vertical effective stress is calculated. In Eq. 3.2 an example is shown of what value the density of the surcharge ρ_{sur} should be to achieve a vertical effective stress of 250 kPa.

Table 3.1: Properties of the surcharge layer.

Description	Symbol	Unit	Value
Layer thickness	D	m	0.1
Porosity	n	-	0.5
Earth pressure coefficient at rest	K_0	-	0.5
Young's modulus	E	MPa	100
Poisson's ratio	ν	-	0

$$\sigma'_v = \frac{(1-n)\cdot\rho_{sur}\cdot 9.81\cdot D}{1000}\ [\text{kPa}] \tag{3.1}$$

$$\rho_{sur} = \frac{250\cdot 1000}{(1-0.5)\cdot 9.81\cdot 0.1} = 509684\ [\text{kg/m}^3] \tag{3.2}$$

3.3 Boundary layer

The boundary layer is an optional layer depending on what type of boundary condition needs to be modelled. The boundary layer is a very soft linear elastic layer. The properties of the layer are shown in Table 3.2. When the boundary layer is used in the model, constant stress boundary conditions are simulated. More information on the boundary conditions is reported in Chapter 6.

Table 3.2: Properties of the boundary layer.

Description	Symbol	Unit	Value
Layer width	W	m	0.1
Earth pressure coefficient at rest	K_0	-	0.5
Young's modulus	E	MPa	0.001
Poisson's ratio	ν	-	0.3

3.4 Reaction forces

An important feature of the program is that it is able to calculate reaction forces on specified surfaces. In this model reaction forces are used to calculate the cone resistance q_c and shaft friction f_s.

The penetration speed of the cone is kept at a constant value of 2 cm per timestep.

3.4.1 Geometry overview

Figure 3.2 shows a close-up of the geometry around the cone. The dimensions of the cone are according to standard NEN-EN-ISO22476-1 (2012) and are indicated in Figure 3.2. On line 1 in red the reaction forces are determined from which the value of the cone resistance q_c can be calculated. From the reaction forces determined on line 2 in green the shaft friction f_s can be determined. In Figure 3.3 a sketch is shown with the determined reaction forces on the areas.

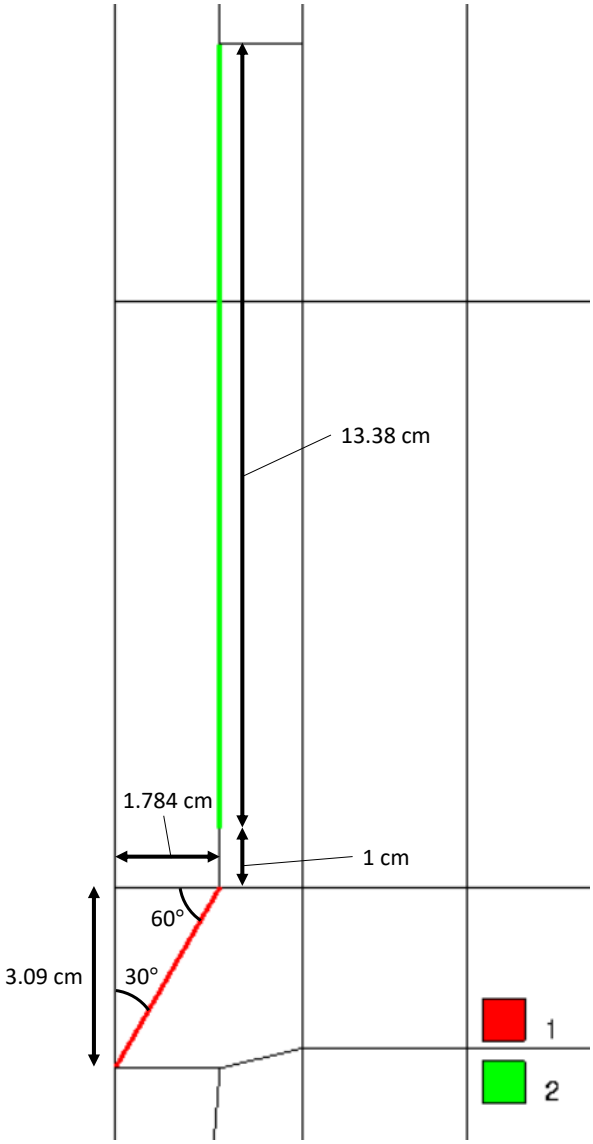

Figure 3.2: Close-up of the geometry of the cone. Reaction forces on line 1 (red) are used to calculate q_c. Reaction forces on line 2 (green) are used to calculate f_s.

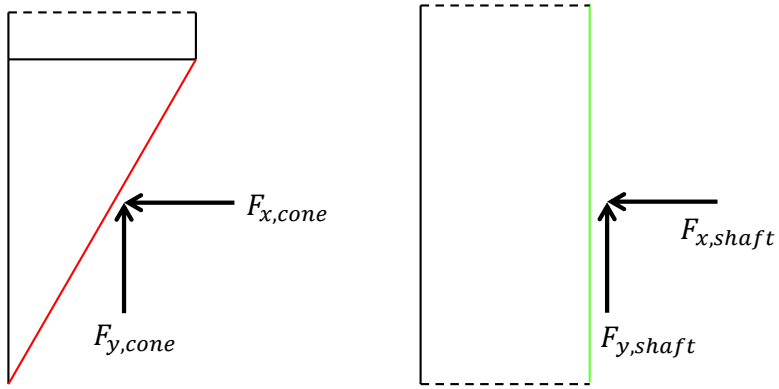

Figure 3.3: Sketch of the reaction forces determined by the model on the specified lines. (Left) the reaction forces on the cone. (Right) the reaction forces on the shaft.

3.4.2 Transition from 2D axisymmetric to 3D

The model outputs the reaction forces for a 2D axisymmetric situation. In an axisymmetric situation the volume of each material point represents one radian around the axis of symmetry (the centre of the cone). To obtain the equivalent forces in a 3D situation, the forces from the 2D axisymmetric situation have to be multiplied by a factor of 2π. The equivalent 3D reaction forces can subsequently be used to determine q_c and f_s.

3.4.3 Cone resistance

The cone resistance is obtained by dividing the equivalent 3D vertical force acting on the cone $F_{y,cone}$ by the cross-sectional area of the cone A_{cone}, see Eq. 3.3. Standard NEN-EN-ISO22476-1 (2012) states that in a standard case the cross-sectional area of the cone is 1000 mm^2. This requirement is maintained in the model as the radius of the cone is 17.84 mm, resulting in $A_{cone} = \pi \cdot 17.84^2 = 999.86$ mm^2. Most of the CC tests used to validate the model later on in Chapter 7 are also performed with the standard cone. Using the standard cone in the model therefore ensures consistency between the experimental tests and the model.

$$q_c = \frac{F_{y,cone}}{A_{cone}} \tag{3.3}$$

The cone resistance can be normalised with respect to the initial stress level according to Eq. 3.4 (Been et al., 1986). This normalisation will mainly be used to compare MPM results with calibration chamber test data.

$$Q = \frac{q_c - p_0}{p_0'} \tag{3.4}$$

3.4.4 Shaft friction

The shaft friction is obtained by dividing the equivalent 3D vertical force acting on the shaft $F_{y,shaft}$ by the area of the shaft A_{shaft}, see Eq. 3.5. Standard NEN-EN-ISO22476-1 (2012) states that the nominal surface area of the shaft on which the shaft friction is determined must be 15000 mm^2. This requirement is maintained in the model with a shaft radius of 17.84 mm and a shaft length of 133.8 mm, resulting in $A_{shaft} = 2\pi \cdot 17.84 \cdot 133.8 = 14997.91$ mm^2.

$$f_s = \frac{F_{y,shaft}}{A_{shaft}} \tag{3.5}$$

3.5 Material point clusters

The material points are defined in rectangular clusters in the domain, called material point clusters (MPCs). Every MPC has a certain density of material points. The density of the MPCs increases when closer to the CPT. This is to ensure that there are no empty elements in surfaces that are defined as a material and to provide a more detailed description of the processes around the cone (which is the most relevant area in the domain). The material points are not only assigned to the soil layer in the domain but also to the surcharge and boundary layers, as these layers are also defined as a material in the model and therefore cannot have empty elements.

MPC 4 has a variable number of material points. This is because this area in the domain is changed when boundary effects are investigated. To keep the density of material points constant, more material points are added when the domain size is increased.

In Table 3.3 the MP densities are shown. For MPC 4, 'X' is the horizontal length of MPC 4 in meters. A sketch of the MPCs in the domain is shown in Figure 3.4.

Table 3.3: Material point density overview.

Cluster number	MP density [hor x ver]
MPC 1	70×650
MPC 2	30×400
MPC 3	30×300
MPC 4	$(x[m] \cdot 100) \times 250$
MPC 5	10×200

The specification of MPs in rectangular clusters results in the amount of MPs being different for each element. The finer elements near the cone will have less MPs in each element than the coarser elements below in the domain. This is in particular the case for MPC 1, because in this region the mesh refinement near the cone will be concentrated. A larger amount of MPs in coarser elements is not a problem because of the mixed integration method that is used for elements that are fully-filled with MPs (see Section 5.2.1 for more information about the mixed integration method).

One aspect that is interesting to investigate is to see if changing the MP density of MPC 1 affects output results. Only MPC 1 is considered because that is the relevant area for the determination of q_c and f_s. For this investigation, three calculations are performed: one with the original MP density of Table 3.3, one where the MP density of MPC 1 is increased with 50% and one with an increase of 100%. The results of this sensitivity analysis are presented in Figure 3.5. The results show that there is virtually no difference between the considered scenarios. The original MP density of Table 3.3 will be adopted for all remaining calculations.

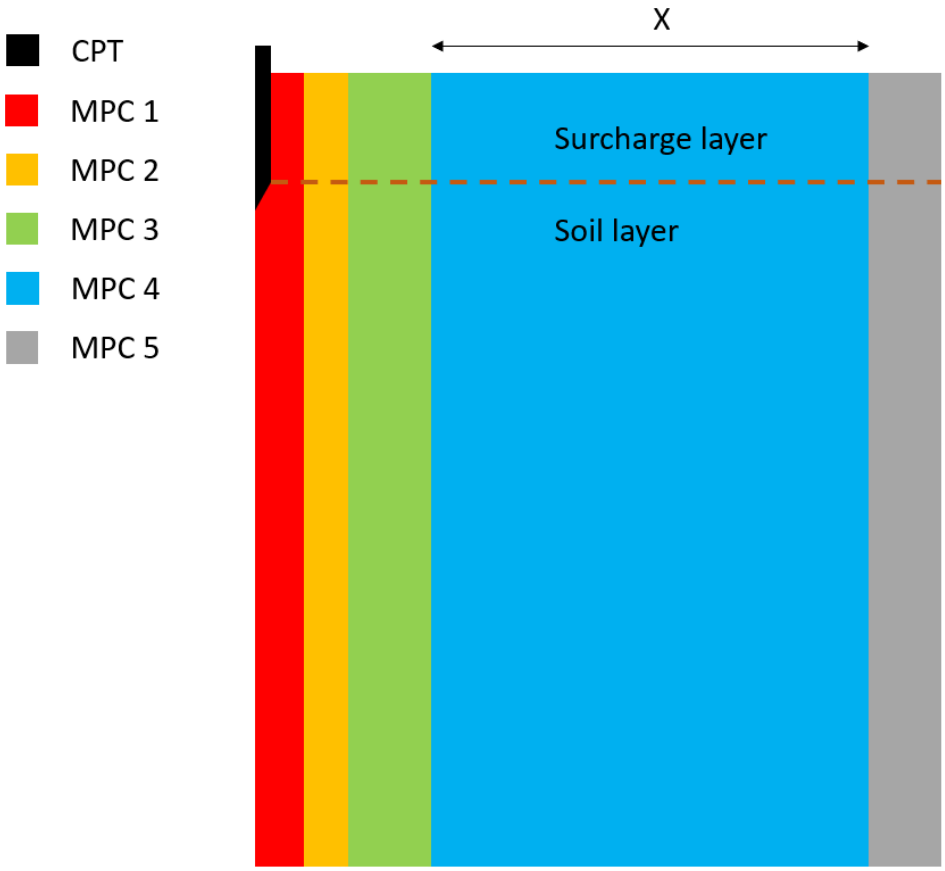

Figure 3.4: Sketch of the material point clusters in the domain (to scale).

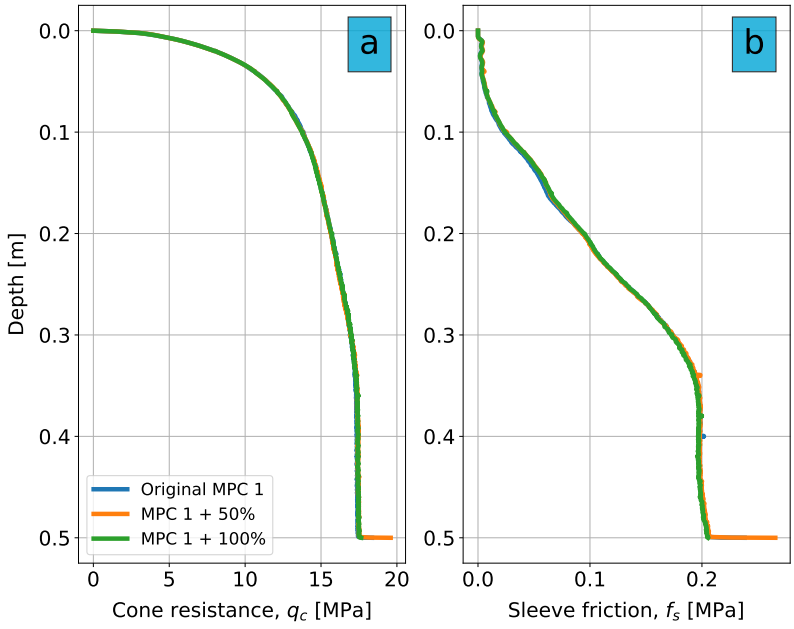

Figure 3.5: Results of the sensitivity analysis of the MP density of MPC 1.

4

Input Parameters

The version of NorSand used in this thesis is an implementation by Deltares. The input parameters in this implementation are largely the same as reported in Section 2.2. This Chapter will provide a complete overview of all input parameters of the NorSand implementation.

It will furthermore be discussed how these input parameters can be determined for different types of sand. Conventionally, the determination of NorSand parameters involves extensive laboratory testing. However, in the absence of testing results for this thesis and difficulties related to the determination of the critical state at high stress levels (most conventional triaxial tests are not able to reach the stress levels which are generally experienced by the soil directly under the cone of a CPT), an alternative method is used to determine the NorSand input parameters. The determination of the CSL parameters will be discussed in particular detail.

The essence of this Chapter is to explain how the input parameters are determined in the absence of triaxial test data, as this is mostly the case in this thesis. The strategy and methods that are used in this process will be elaborated on. This Chapter will not explain how NorSand parameters can be determined from triaxial test data. For this, the reader is referred to Jefferies and Been (2016) where a detailed description of the determination of NorSand parameters from laboratory experiments is presented.

4.1 Input parameters overview

In Table 4.1 an overview of all relevant NorSand input parameters of the implementation used in this thesis is presented. The parameter symbol is shown alongside a description of the parameter. The final column references to the Equation in Section 2.2 of the literature study in which that particular parameter is explained in greater detail. If a certain parameter has not been discussed in Chapter 2, it means that that parameter is specific to this implementation of NorSand and will be elaborated on in the current Chapter.

Table 4.1: Overview of NorSand input parameters.

Parameter [unit]	Description	Chapter 2 reference
G_{ref} [-]	Shear modulus coefficient	Eq. 2.49 (equiv. of A)
ν [-]	Poisson's ratio	Eq. 2.50
a [-]	Exponent in stiffness relation	Eq. 2.49
Γ [-]	Critical state void ratio at $p' = 1$ kPa for a log-lin CSL	Eq. 2.5
e_Γ [-]	Critical state void ratio at $p' = 1$ kPa for a curved CSL	N/A
λ [-]	Slope of log-lin CSL in e-p' space	Eq. 2.5
λ_c [-]	Slope of curved CSL in e-p' space	N/A
ξ [-]	Exponent of curved CSL	N/A
ϕ_c [°]	Critical state friction angle	Eq. 2.10
N [-]	Volumetric coupling parameter	Eq. 2.31 & Eq. 2.32
H [-]	Hardening modulus	Eq. 2.47
χ_{tc} [-]	Coefficient of maximum dilatancy in triaxial compression conditions	Eq. 2.14
ψ_0 [-]	Initial state parameter	Eq. 2.13
$F_{e,fac}$ [-]	Factor for void ratio in elastic stiffness	Eq. 2.49
$e_{el,min}$ [-]	Minimum void ratio where volumetric strains are negligible	Eq. 2.49

4.2 Input parameters determination

The input parameters from Table 4.1 are divided into three categories:

1. Plasticity parameters: N, H, χ_{tc}.
2. Elasticity parameters: G_{ref}, ν, a, $F_{e,fac}$, $e_{el,min}$.
3. CSL parameters: Γ, e_Γ, λ, λ_c, ξ, ϕ_c.

The initial state parameter ψ_0 is the parameter defining the state of the soil and is not assigned to one of the three categories above.

As an example, the parameters for Ticino 4 sand are determined to illustrate the parameter determination process.

4.2.1 Plasticity parameters

The plasticity parameters are all obtained from literature. In Ghafghazi and Shuttle (2008) the plasticity parameters for several sands are reported. These values are used to determine the plasticity parameters.

For Ticino 4 sand the plasticity parameters are reported in Table 4.2. The hardening modulus H is a function of the initial state parameter. This is not uncommon and is also described in Jefferies and Been (2016).

Table 4.2: Plasticity parameters for Ticino 4 sand obtained from Ghafghazi and Shuttle (2008).

Parameter [unit]	Value
N [-]	0.40
H [-]	$70 - 200\psi_0$
χ_{tc} [-]	3.0

4.2.2 Elasticity parameters

The elasticity parameters are partly obtained from literature and partly from a parameter optimisation analysis. From Ghafghazi and Shuttle (2008) an expression of the rigidity index I_r and a value of the Poisson's ratio are obtained.

In Ghafghazi and Shuttle (2008) the rigidity index is determined from the initial mean effective stress p'_0 and is therefore an invariable. For the modelling of a CPT it is viewed to be more appropriate to use the current value of the mean effective stress p' instead. This is deemed more suitable to account for the expected large variations in stresses during a CPT.

The elasticity parameters for Ticino 4 sand are reported in Table 4.3.

Table 4.3: Elasticity parameters for Ticino 4 sand obtained from Ghafghazi and Shuttle (2008).

Parameter [unit]	Value
I_r [-]	$\frac{650}{e^{1.3}}\left(\frac{p'}{p_{ref}}\right)^{-0.52}$
ν [-]	0.2

In the implementation of NorSand used in this thesis the elasticity implementation is closely related to Eq. 2.49. Eq. 4.1 shows the implementation used in this thesis. The expression for F_e is shown in Eq. 4.2. $F_{e,fac}$ is a factor ranging from 0 to 1. If $F_{e,fac} = 0$ the standard Eq. 4.2 is used. If $F_{e,fac} = 1 \rightarrow F_e = 1$, see Eq. 4.3. This means that the elastic stiffness will have no dependency on the void ratio.

$$G = G_{ref} F_e p_{atm} \left(\frac{p + p_t}{p_{atm}}\right)^a \tag{4.1}$$

$$F_e = \frac{1}{e - e_{el,min}} \tag{4.2}$$

$$F_e = F_e + (1 - F_e)F_{e,fac} \tag{4.3}$$

By default the void ratio is taken into consideration for the determination of the elastic stiffness, meaning that $F_{e,fac} = 0$. p_t is a small offset of the stress of $p_t = 1$ kPa. The atmospheric pressure is by default $p_{atm} = 100$ kPa. It is assumed that at a void ratio of 0.2 the volumetric strains will

be negligible, resulting in $e_{el,min} = 0.2$. By default the exponent a in the stiffness relation is set to $a = 0.5$.

This leaves G_{ref} as the only input parameter that still needs to be determined. G_{ref} is determined by means of parameter optimisation. For this procedure the Nelder-Mead function optimisation method (Nelder & Mead, 1965) is used. In this procedure an optimal value of G_{ref} is determined such that Eq. 4.1 will fit as good as possible to the known stiffness relation from literature (in the case of Ticino 4 sand reported in Table 4.3). The shear modulus can be obtained from Eq. 2.48.

From Eq. 4.1 it is apparent that the shear modulus is dependent on both the stress level and the void ratio. The rigidity index of Ticino 4 sand shown in Table 4.3 also has a dependency on both the stress level and void ratio. Most other sands reported in Ghafghazi and Shuttle (2008) also have this dual stiffness dependency.

To take the dual stiffness dependency into account for the determination of the elasticity the following is considered:

- The range of effective stress over which the parameter optimisation will be performed is $0 \text{ kPa} < p' < 5000 \text{ kPa}$. The selected range of p' represents both the high stress levels under the cone as well as the lower stress levels in the domain.
- The parameter optimisation will be performed for four different void ratios: the minimum and maximum void ratio, and two intermediate void ratios. Subsequently, the four obtained values of G_{ref} will be averaged to obtain a generalised value of G_{ref}. Values of e_{min} and e_{max} can be obtained from Ghafghazi and Shuttle (2008).

For Ticino 4 sand minimum and maximum void ratios are respectively $e_{min} = 0.6$ and $e_{max} = 0.89$. The two intermediate void ratios are $e = 0.7$ and $e = 0.79$.

Figure 4.1 shows the results of the parameter optimisation for Ticino 4 sand. The dotted line is the result of the expression reported in literature. The solid line is the result of Eq. 4.1 with the optimised value of G_{ref} for that specific void ratio (shown in the red box in each plot). The average of the four G_{ref} values is shown at the top of the figure as $G_{ref,avg}$. This is ultimately the value that will be used as input in the model.

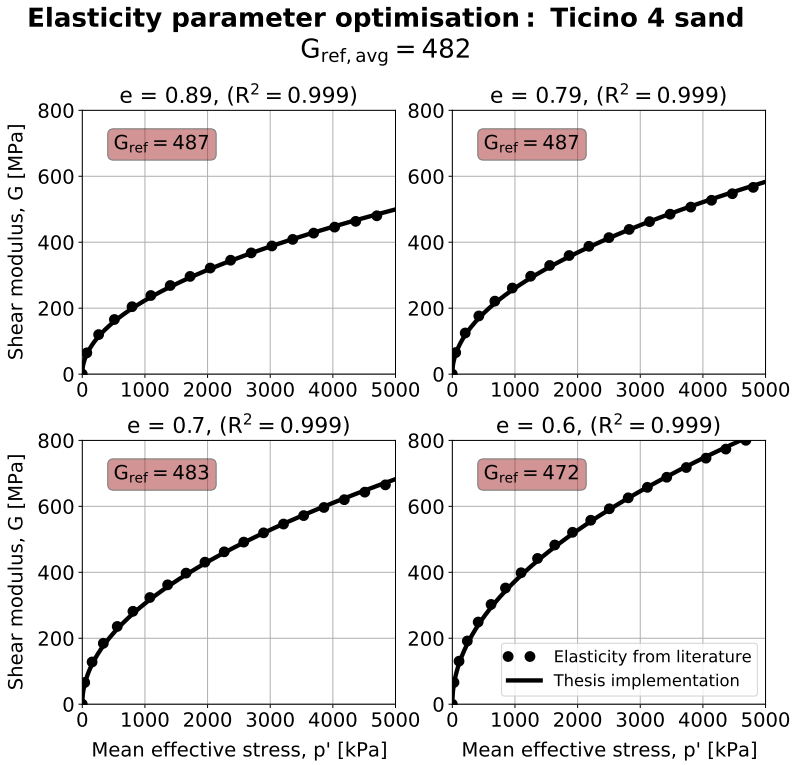

Figure 4.1: Results of the parameter optimisation for Ticino 4 sand.

Figure 4.1 shows that Eq. 4.1 is able to describe the stiffness relation in literature very well. This is easily observed from the two lines overlapping in plots. Also, a quantitative description of the quality of the optimisation is presented in the form of the coefficient of determination R^2.

A simple form of the coefficient of determination is used, shown in Eq. 4.4. SS_{res} is the sum of the squares of the residuals. SS_{tot} is the total sum of squares, which is proportional to the variance of the data.

A residual is defined as the difference between the data and the fitted function. In this optimisation analysis the data is the relation from literature and the fitted function the elasticity implementation of Eq. 4.1. A small residual implies a better fit of a function to the data. The best possible situation is that the data and the fitted function are identical. This would mean that the residual would be zero and $SS_{res} = 0$ as well. From Eq. 4.4 it follows that for $SS_{res} = 0 \rightarrow R^2 = 1$. Theoretically speaking the R^2 value can thus not be larger than one. The closer R^2 is to one, the better the fit and the optimisation.

$$R^2 = 1 - \frac{SS_{res}}{SS_{tot}} \tag{4.4}$$

Figure 4.1 shows a near perfect fit of Eq. 4.1 to the relation from literature with coefficient of determination values for all void ratios of $R^2 = 0.999$, indicating an excellent optimisation of G_{ref}.

4.2.3 CSL parameters

In the model a choice can be made between two different types of CSL. The traditional log-linear CSL of Eq. 2.5 (repeated below) and a curved CSL formulated with Eq. 4.6.

$$e_c = \Gamma - \lambda \ln(p') \tag{4.5}$$

$$e_c = e_\Gamma - \lambda_c \left(\frac{p'}{p_{ref}} \right)^{\xi} \tag{4.6}$$

As discussed earlier in the literature research, the type of CSL formulation does not affect the workings of the state parameter in NorSand. It merely changes the value of e_c at a certain stress level. In principle, any equation as a function of mean effective stress could be used to represent the CSL, as long as it accurately represents soil data.

Eq. 4.6 is a popular equation to add a curvature to the CSL at high stress levels. In Figure 4.2 it can be seen how Eq. 4.6 is used to accurately represent the CSL of Toyoura sand (Verdugo, 1992). The laboratory measurements shown in Figure 4.2 clearly show a sharper decrease in critical void ratio for $p' > 500$, which is accurately captured by Eq. 4.6.

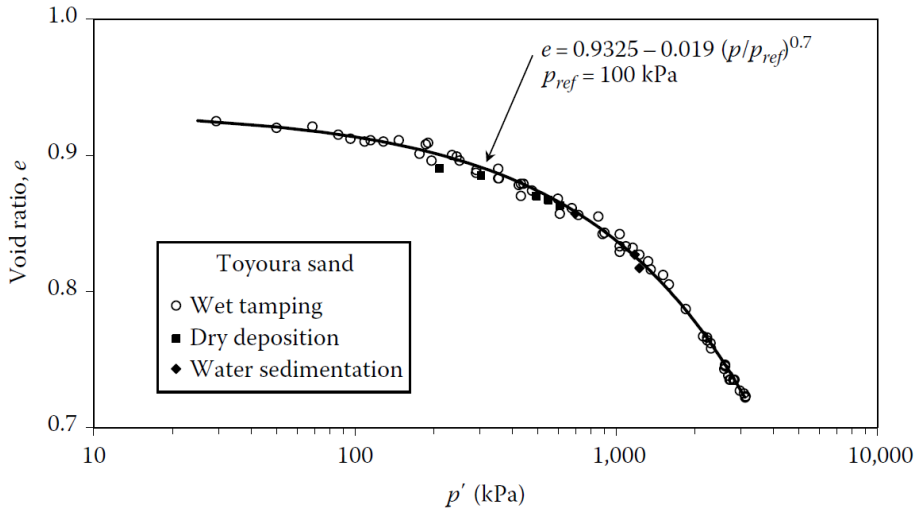

Figure 4.2: Illustration of how a curved CSL relates to laboratory measurements at high stress levels. Adopted from Jefferies and Been (2016), data from Verdugo (1992).

Critical friction ratio

In Ghafghazi and Shuttle (2008) the critical friction ratio determined under triaxial compression conditions M_{tc} is reported. Using Eq. 2.10, the critical friction angle ϕ_c can be determined from M_{tc}. ϕ_c will be used as an input parameter in the model.

Log-linear CSL parameters

The log-linear CSL parameters are determined in a similar fashion as the plasticity parameters. In the paper of Ghafghazi and Shuttle (2008) Γ and λ values for several different sands are reported. If a log-linear CSL is selected these values will be used as input parameters. For Ticino 4 sand these parameters are $\Gamma = 0.986$ and $\lambda = 0.0243$.

Curved CSL parameters

The determination of the curved CSL parameters is more complex. The main reason for this is that beside the formulation for Toyoura sand from Figure 4.2 no formulations for other sand types are reported. The high mean effective stress levels at which the critical void ratio must be determined is a limiting factor. Conventional testing equipment is often not capable of reaching these high stress states.

In the absence of laboratory data, the curved CSL parameters are determined differently. For certain sands the parameters of the compression model of Pestana and Whittle (1995) are reported in literature (see Section 2.3). With these parameters the 1-D compression of that sand can be modelled. Subsequently an oedometer test is simulated with NorSand using the incremental driver single element program developed by Niemunis (2007). The three curved CSL parameters e_Γ, λ_c and ξ are then manually iterated until the two compression curves are comparable in e-p' space. The calibration is performed at an initial void ratio corresponding to $D_R = 50\%$. In this process two requirements must be maintained:

1. The results from the NorSand oedometer simulation must be in agreement with the 1-D compression model from Pestana and Whittle (1995). The assessment of the agreement between the two results is determined by a visual inspection of the compression curves in e-p' space and by a form of a coefficient of determination R_*^2, as explained in Appendix B.

2. The curved CSL falls within the indicative bounds of the CSL, proposed by Robertson (2017). Robertson (2017) states that at high stresses the compression line for sands tends towards the LCC of the compression model of Pestana and Whittle (1995), and that the LCC becomes parallel to the CSL. It is stated that the CSL can be assumed to be parallel to the LCC with a spacing ratio of about 2 to 4.

   When the curved CSL formulation of Eq. 4.6 is used it is not possible to obtain a parallel CSL at high stresses. However, it is possible to let the CSL fall in the region of the 2 to 4 spacing ratio parallel to the LCC. This is maintained as the criterion to assure that the CSL is represented in a correct manner at high mean effective stress levels.

Figure 4.3 shows the results of the calibration of the curved CSL parameters. Notice in Figure 4.3a that at high values of p' the curved CSL falls within the 'spacing ratio region', implying that the second requirement described above is met. In Figure 4.3b the oedometer simulations are compared with the 1-D compression model. The oedometer simulation shows similar results as the 1-D compression model. The value of $R_*^2 = 0.643$ is also sufficient (see Appendix B.1). The curved CSL parameter values used to obtain this simulation result are $e_\Gamma = 0.93$, $\lambda_c = 0.045$, $\xi = 0.56$ and are also shown above Figure 4.3a.

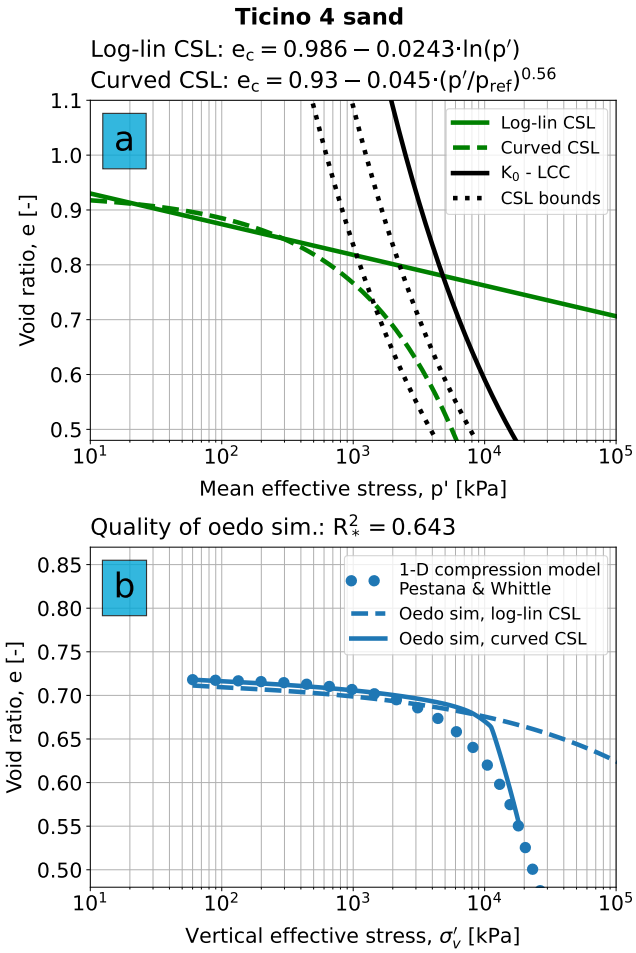

Figure 4.3: Results of the curved CSL parameter calibration for Ticino 4 sand. (a) shows the two different CSL's in e-p' space. The K_0-LCC with the corresponding CSL bounds following from the spacing ratio region is shown. (b) shows the result of the 1-D compression model from Pestana and Whittle (1995). The oedometer simulation is shown for both the log-linear and the curved CSL.

Necessity of the curved CSL

From Figure 4.3b it becomes apparent that using the traditional log-linear CSL results in widely different 1-D compression results compared to the compression model of Pestana and Whittle (1995). At lower stress levels the differences between the log-linear and the curved CSL are not too large (see Figure 4.3a). This results in a very similar results of the oedometer simulation for low stress levels. However, at very high stress levels the curved CSL sharply decreases in e-p' space whereas the log-linear CSL continues to decrease steadily. This translates into the large differences of the oedometer simulation from Figure 4.3b.

With the large increase of σ'_v in an oedometer simulation, eventually the critical state will be reached. The curvature of the curved CSL allows for a much sharper decrease in void ratio compared to the log-linear CSL. In Section 2.3 it is pointed out the the LCC regime of the compression model by Pestana and Whittle (1995) is governed by particle crushing. The crushing of particles is the reason for the sharp decrease in void ratio when high stresses are obtained. The log-linear CSL is not able to account for this decrease in void ratio when critical state is reached, which causes the oedometer simulation to not accurately describe the compression model of Pestana and Whittle (1995).

Beside the inability of the log-linear CSL to accurately simulate an oedometer test it is interesting to investigate how the different CSL formulations influence the MPM modelling results. For this purpose a set of MPM calculations has been performed with both the log-linear CSL and the curved CSL for Ticino 4 sand at an initial vertical effective stress of $\sigma'_{v0} = 323.73$ kPa and $\sigma'_{v0} = 107.91$ kPa, for a range of different initial state parameters ψ_0. The results presented in Figure 4.4 show that the choice of the CSL formulation has a large influence on the MPM results. Depending on ψ_0 the differences can be larger than a factor 2 between the two CSL formulations. The reason for this large difference is similar as the differences observed in the oedometer simulation. The use of a curved CSL allows for compaction under the cone when critical state is reached under high stress states. This results in a loss of support of the surrounding soil and thus less resistance is present, leading to lower values of q_c.

When looking at the results of $\psi_0 = -0.30$ a value of $q_c \approx 100$ MPa is obtained when using the log-linear CSL. Even though a state parameter of $\psi_0 = -0.30$ indicates a very dense sand, and the stress level of $\sigma'_v = 323.73$ kPa is rather high, a q_c value of 100 MPa seems excessive when comparing with empirical relations from literature (Robertson, 2010).

To further investigate the suitability of the log-linear CSL for the modelling a CPT a comparison is made with calibration chamber (CC) tests reported by Baldi et al. (1986), shown in Figure 4.5. In this Figure the normalised cone resistance Q is plotted against the initial state parameter ψ_0. In the reported data from Baldi et al. (1986), among other properties, the initial void ratio and mean effective stress are reported. ψ_0 is not reported in the original data, but is determined from the critical void ratio which can be obtained from the CSL. To be consistent, ψ_0 for the CC tests is determined with the same CSL as is used in the MPM simulations. This is the reason that the CC test data looks different between Figures 4.5a and 4.5b. The same test data is used, only ψ_0 is calculated using a different CSL formulation.

The CC test data show a decrease of the normalised cone resistance Q with an increasing stress level. This can be attributed mainly to the larger increase of stress level in the denominator term of Eq. 3.4 relative to the increase of q_c in the numerator. When comparing the two CSL formulations it can be clearly seen that when using a curved CSL, Q decreases when the initial stress level is increased. This is not the case for the log-linear CSL, where the difference between the initial vertical effective stress of $\sigma'_{v0} = 107.91$ and $\sigma'_{v0} = 323.73$ is minor. The MPM results with the log-linear CSL for higher stress levels are not in agreement with reported CC test data, whereas the curved CSL MPM results show better similarities.

It is concluded that using the log-linear CSL does not result in MPM results which are in agreement with CC test data due to the inability to accurately represent the critical state at the high stress levels occurring under the cone of the CPT. The curved CSL is, however, able to achieve this. The sharp decrease of the CSL at high stress levels incorporates to some extent the particle crushing effects under the CPT. For the remainder of this thesis the curved formulation of the CSL will be adopted.

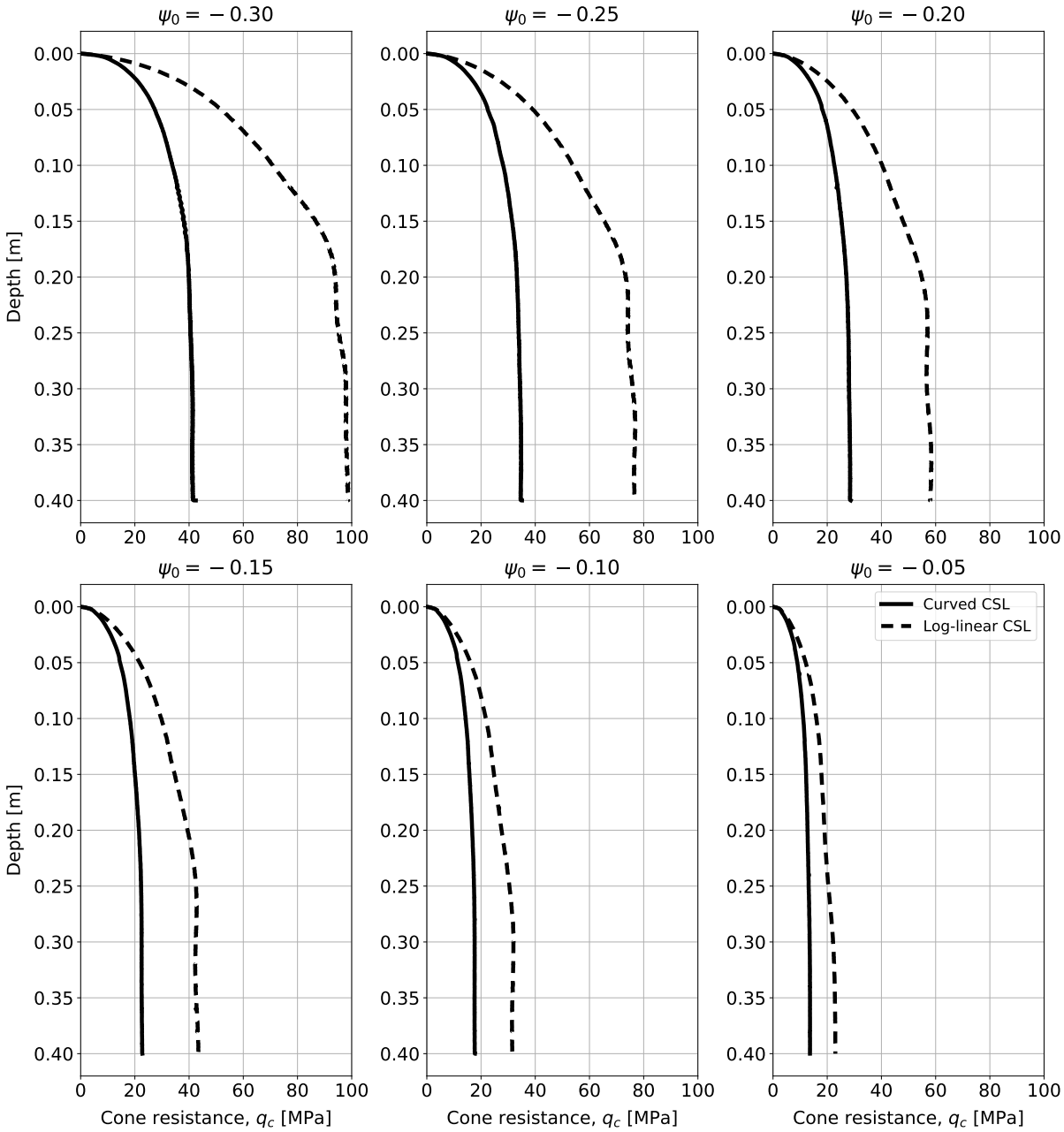

Figure 4.4: q_c−depth results of the different CSL for an initial vertical stress of $\sigma'_{v0} = 323.73$ kPa.

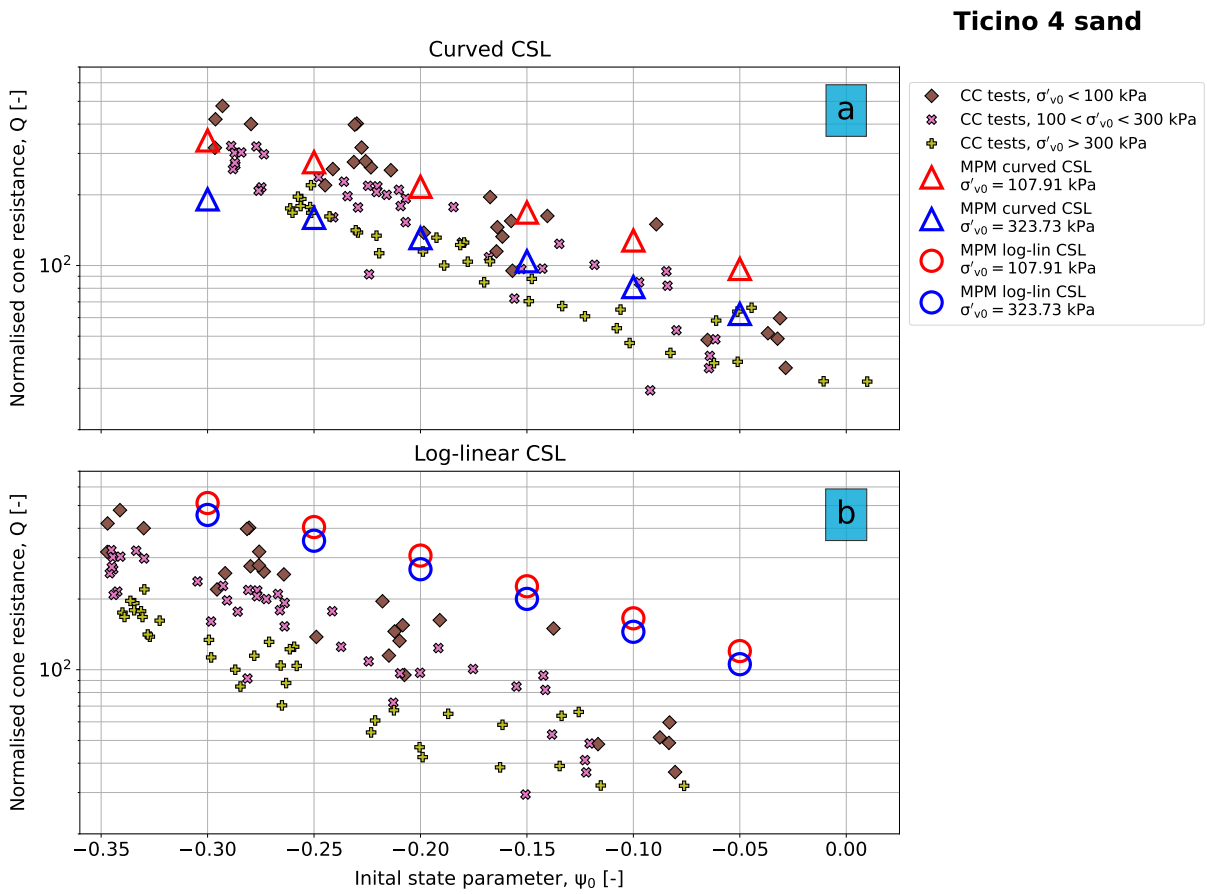

Figure 4.5: Comparison of the different CSL formulations with respect to CC data. (a) for a curved CSL, (b) for a log-linear CSL. CC data from Baldi et al. (1986).

5

Numerical Verification

In this Chapter the results of the numerical verification phase are presented. The goal of this phase is to determine the optimal numerical calculation settings and setup before the validation of the model can be performed. If changing the numerical setup leads to quantitative differences of model results, it should be investigated why this occurs and whether the new setup should be used in the validation phase or not.

Roughly speaking the numerical verification can be subdivided into three parts:

1. Investigation of the calculation settings: the program offers certain numerical settings which can be modified. Changing these settings requires small sensitivity analyses to investigate the influence on the model results.
2. Investigation of the mesh size: changing the size of the mesh has implications on modelling results and must be assessed to obtain an optimal mesh size.
3. Investigation of the element type: results of the previous parts showed that the type of element used (triangular or quadrilateral) has a quantitative effect on model results and requires an additional investigation.

To keep this Chapter concise, only results which are reason for discussion or which directly support statements will be reported in this Chapter. All other results will be reported in Appendix C to give a complete overview.

5.1 Initialisation

As a starting point of the numerical verification phase the article of Martinelli and Galavi (2021) is consulted. In this article an investigation of the numerical setup has been performed for the Hardening Soil (HS) constitutive model. Using Martinelli and Galavi (2021) as a reference point the following numerical setup is used to initialise the verification phase:

- Triangular elements will be used in the analysis;
- The MPM-Mixed integration method is used (see Section 5.2.1 for an elaboration on the different integration methods the program offers);
- The strain smoothing (SS) procedure will be applied;
- The initial mesh size around the cone tip is 4.5 mm (equal to 0.13 times the cone diameter D_c);

- The initial mass scaling factor (MSF) is set to 3000 (see Section 5.2.2 for an elaboration on the MSF);
- The initial damping factor is set to 0.1 (see Section 5.2.3 for an elaboration on the damping factor).

Furthermore, the following boundary conditions are used in the numerical verification phase (see Chapter 6 for a more detailed description of the boundary conditions):

- The size of the domain is equal to a chamber cone ratio (CCR) of 50;
- A constant stress boundary condition is used at the outer vertical boundary of the domain;
- At the bottom horizontal boundary a zero displacement boundary condition is maintained.

5.1.1 NorSand parameters

For the numerical verification phase a set of NorSand parameters for Ticino 4 sand is used, shown in Table 5.1. The parameters are obtained according to the parameter determination procedure described in Chapter 4.

Compared to the examples shown in Chapter 4, a slight difference in the parameters is observed. This is mainly due to the parameter $e_{el,min}$, which is not kept at a constant value of 0.2. At the time of the determination of the parameter set of Table 5.1 the $e_{el,min}$ parameter was also a variable included in the parameter optimisation just like G_{ref}. Later on it was decided to keep $e_{el,min}$ constant because elasticity fits would still be excellent and G_{ref} values would be more consistent. Despite the slight difference in the parameter determination procedure, the parameter set of Table 5.1 still describes Ticino 4 sand as all requirements named in Chapter 4 are maintained. Therefore, the parameter set of Table 5.1 is still suitable for performing the numerical verification.

The initial state parameter ψ_0 is set to a value of -0.15.

Table 5.1: Ticino 4 NorSand parameters used for the numerical verification phase.

Parameter [unit]	**Value**	**Parameter [unit]**	**Value**
G_{ref} [-]	504	N [-]	0.40
ν [-]	0.2	H [-]	$70 - 200\psi_0$
a [-]	0.5	χ_{tc} [-]	3.0
e_Γ [-]	0.93	ψ_0 [-]	-0.15
λ_c [-]	0.055	$F_{e,fac}$ [-]	0
ξ [-]	0.54	$e_{el,min}$ [-]	0.194
ϕ_c [°]	31.6		

5.2 Calculation settings

5.2.1 Integration method

Beside the calculation of stresses and state variables at all material points, the program offers another integration method called mixed integration. In mixed integration the stresses and state variables of all MPs are averaged per element. Internal forces are then calculated using Gauss integration, as is the case in FEM. The average stress and state variables are subsequently assigned back to the MPs (Ceccato et al., 2019).

The Gauss integration is only applied when an element is fully-filled, meaning that the volume of the sum of MPs should be greater or equal than 90% of the volume of the element. If this condition is not met, standard material point integration is used. In the current program this mixed integration method is called MPM-Mixed, whereas the standard material point integration is called MPM-MP.

When an element is fully-filled, the stresses and state variables are the same for all MPs because they are averaged. This allows for only one MP to be used for stress integration, reducing the computational cost considerably compared to standard MP integration where stresses have to be calculated for every MP. However, it must be noted that the MPM-Mixed method when used with complex constitutive models could lead to discrepancies due to incompatibilities between stresses and state variables when averaged (Martinelli & Galavi, 2021). Because of this, a comparison between the two integration methods is made, with the results shown in Figure 5.1.

From Figure 5.1 it becomes clear that the differences between the two integration methods are relatively small. The difference of q_c between the methods is around 7.5%, and the difference of f_s is around 14%. The computational time of the MPM-MP method is approximately 5 times higher than that of the MPM-Mixed method on the same machine. Considering the large decrease in computational cost with limited effect on the results, it is decided that all simulations in this thesis will be performed with the MPM-Mixed integration method.

Previous studies from Schuringa (2020) and Martinelli and Galavi (2021) also justify using the MPM-Mixed method over the MPM-MP method where the MCSS and HS constitutive models were used respectively. This is now also shown for the NorSand constitutive model.

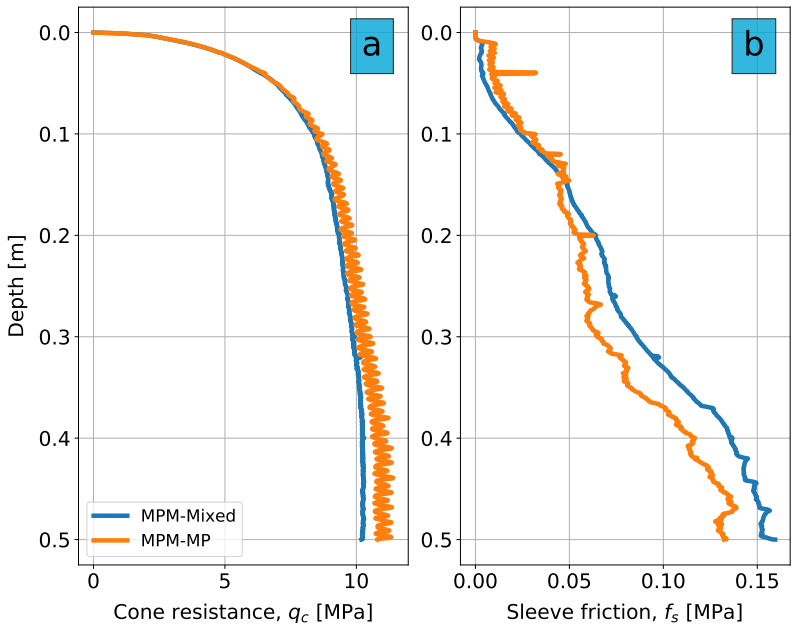

Figure 5.1: Results of integration method comparison. Constitutive model used: NorSand.

5.2.2 Mass scaling factor

The computational efficiency of quasi-static problems with a dynamic explicit code can be low due to limitations of the time step size. However, the time step size can be artificially increased. This is accomplished by applying a mass scaling factor (MSF). The critical time step is manually increased by a factor $\sqrt{\text{MSF}}$ of the MSF specified by the user. Mass scaling is an effective tool to increase the efficiency of the program. However, high values of the MSF can significantly impact the results, and a sensitivity analysis of the MSF is required before use (Ceccato et al., 2019).

In this sensitivity analysis three different values of the MSF are evaluated: 3000, 10000, 20000. All other conditions are kept the same for the three simulations. In Figure 5.2 the results of the MSF sensitivity analysis are shown. Figure 5.2a shows that the MSF has practically no influence on the cone resistance. From Figure 5.2b it can be seen that the MSF has more effect on the shaft friction, but the end results are very similar although not yet stable for MSF $=$ 10000 and MSF $=$ 20000.

It is decided to continue to use a value of MSF $=$ 10000. The computational time is significantly reduced compared to MSF $=$ 3000 (approx. 2 times faster on the same machine), while cone resistance and shaft friction results are comparable. Knowing that results for MSF $=$ 20000 also do not significantly impact the results, it can be concluded that a MSF of 10000 is an acceptable value to use in further analyses. A MSF of 20000 was not selected because a value of MSF $=$ 10000 proved sufficient to run the simulations with acceptable duration.

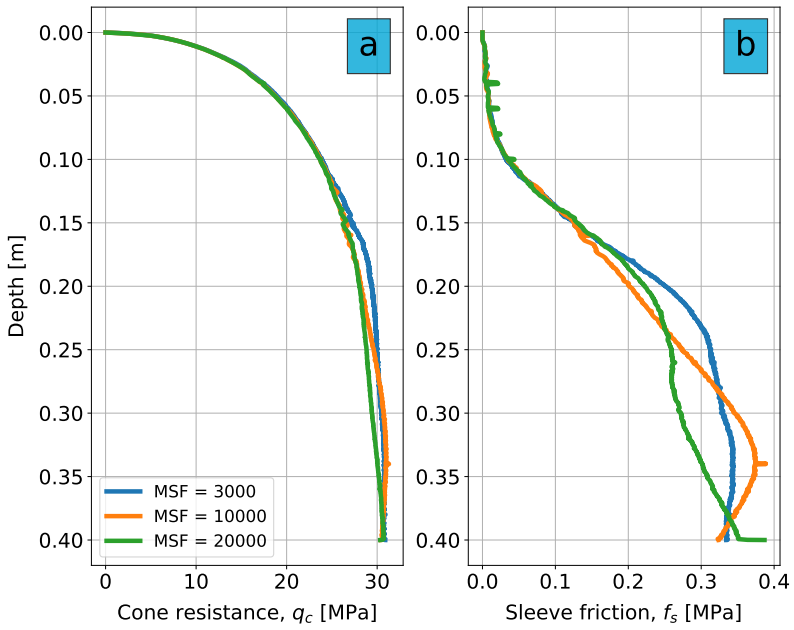

Figure 5.2: Results of MSF sensitivity analysis. Constitutive model used: NorSand.

5.2.3 Damping factor

A natural dynamic system contains damping of the vibrating energy. If that were not the case the system would continue to oscillate when forces are applied. In a numerical simulation the damping in the system should reproduce the energy loss which occurs in a natural system. It is difficult to numerically reproduce the natural damping, but when a constitutive model is able to accurately model the dissipation of energy in the system no additional numerical damping is necessary (Ceccato et al., 2019). NorSand is a nonlinear constitutive model which dissipates energy due to hardening plasticity. It is therefore expected that purely numerical damping has a limited influence on the modelling results. To support this statement a short sensitivity study on the damping factor is performed.

Numerical damping is controlled by a damping factor. The local damping force is proportional to this damping factor. A damping factor of zero means that no numerical damping is present in the system.

In Figure 5.3 the results of the damping factor sensitivity analysis is presented. It can be observed that increasing the damping factor from the starting value of 0.1 has almost no effect on the cone resistance and sleeve friction. Disabling numerical damping (i.e. damping factor of 0) does not affect the cone resistance, whereas it causes instability on sleeve friction results. It is decided to maintain a low value of the damping factor of 0.1. The combination of a constitutive model which dissipates energy with the relatively low penetration speed of the cone allow for a low damping factor to be sufficient to account for damping in the system.

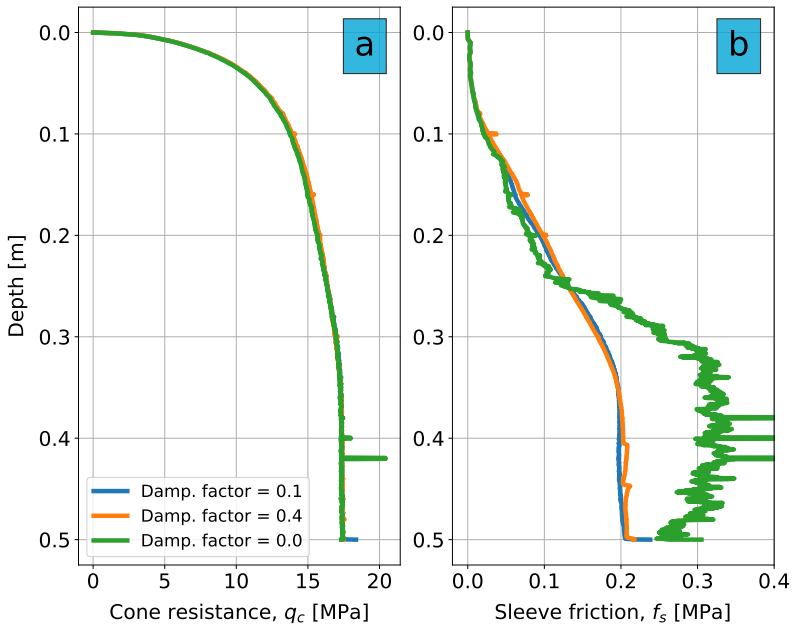

Figure 5.3: Results of the damping factor sensitivity analysis. Constitutive model used: NorSand.

5.3 Mesh size analysis

5.3.1 Approach

On the surfaces shown in Figure A.1 the average mesh size of the surface can be specified. The mesh is then automatically generated for that surface. Multiple surfaces in the domain are combined to create areas. A drawing of these areas is shown in Figure 5.4. Each area is assigned a specific mesh size.

The areas are defined such that a mesh refinement can be achieved near the cone. It is desired to have a finer mesh near the cone. A finer mesh means that there are more nodes at this location, resulting in more calculations to be performed. Generally speaking, this results in a higher accuracy of the results at these locations. The drawback of using a finer mesh is that the calculation time increases because of the additional calculations that are needed at the added nodes.

The optimal mesh size is always a trade-off between accuracy of the results and computational time. At a certain mesh size, further refinement of the mesh does not necessarily result in a large improvement of the accuracy, whereas the calculation time can still increase significantly. The results converge towards a final value. The point at which this convergence occurs is considered to be the optimal mesh size: the results are accurate because further refinement does not lead to (a large) change in model results, and the calculation time is not unnecessary high.

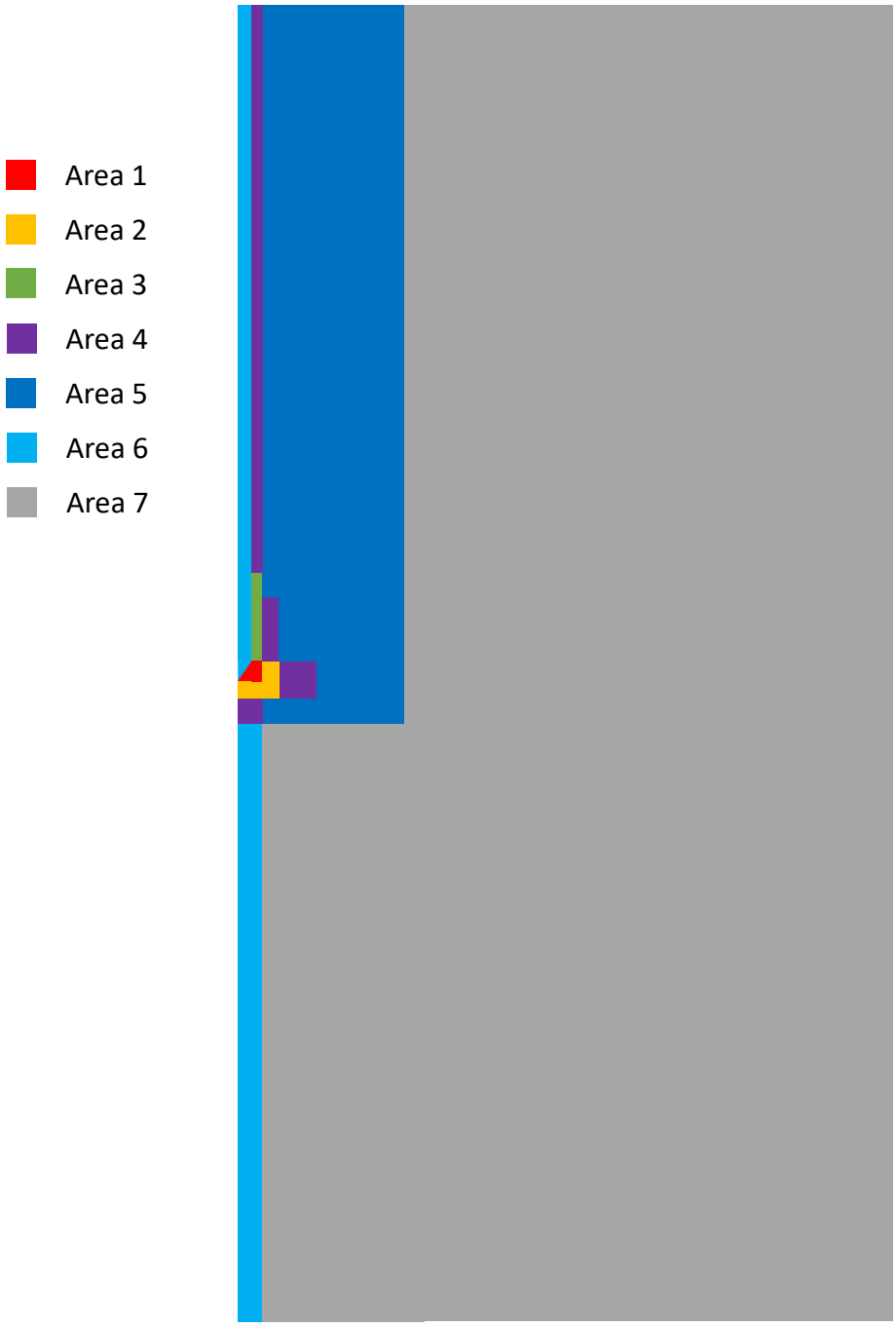

Figure 5.4: Sketch of the defined areas in the domain.

To investigate what the effect is of changing the mesh size of a specific area, different scenarios are modelled. This is conducted as follows:

1. A base mesh is defined as a starting point. This mesh is called Mesh 00.
2. To investigate the influence of Area 1 on the model results, a scenario is modelled where Area 1 is refined with 33% compared to Mesh 00, and a scenario is modelled where the mesh size is enlarged with 33% compared to Mesh 00. The refined mesh of Area 1 is called Mesh 1a. The enlarged mesh of Area 1 is called Mesh 1b.
3. The refinement and enlargement of 33% is repeated for Areas 2-6. These meshes are then respectively named in similar fashion Mesh 2a, Mesh 2b, etc. Area 7 is not considered in the mesh optimisation. This is because Area 7 has a default mesh size to fill up the domain.
4. The average mesh size of each area is reported for each scenario in terms of a ratio with the cone diameter D_c in Table 5.2.

Table 5.2: Overview of the average mesh size for the different scenarios of the mesh size analysis. The mesh size is shown in ratio to the cone diameter $D_c = 35.68$ mm.

	Area 1	**Area 2**	**Area 3**	**Area 4**	**Area 5**	**Area 6**	**Area 7**
Mesh 00	0.126	0.224	0.126	0.420	0.561	0.841	1.401
Mesh 1a	0.084	0.224	0.126	0.420	0.561	0.841	1.401
Mesh 1b	0.168	0.224	0.126	0.420	0.561	0.841	1.401
Mesh 2a	0.126	0.150	0.126	0.420	0.561	0.841	1.401
Mesh 2b	0.126	0.298	0.126	0.420	0.561	0.841	1.401
Mesh 3a	0.126	0.224	0.084	0.420	0.561	0.841	1.401
Mesh 3b	0.126	0.224	0.168	0.420	0.561	0.841	1.401
Mesh 4a	0.126	0.224	0.126	0.280	0.561	0.841	1.401
Mesh 4b	0.126	0.224	0.126	0.561	0.561	0.841	1.401
Mesh 5a	0.126	0.224	0.126	0.420	0.373	0.841	1.401
Mesh 5b	0.126	0.224	0.126	0.420	0.748	0.841	1.401
Mesh 6a	0.126	0.224	0.126	0.420	0.561	0.561	1.401
Mesh 6b	0.126	0.224	0.126	0.420	0.561	1.118	1.401

5.3.2 Results

The results of Area 1 and 3 are shown in Figure 5.5. The results of the remaining areas are shown in Figures C.1 and C.2.

From Figures C.1 and C.2 it becomes apparent that Areas 2, 4, 5 and 6 have very little to no influence on q_c and f_s. These results are not surprising as the reaction forces defined on a surface in the model (see Section 3.4) are determined by the forces on the adjacent nodes of an element to that surface. The areas which are in direct contact with the surfaces on which the reaction forces are determined (Area 1 for q_c and Area 3 for f_s) are therefore expected to have the largest influence.

In Figure 5.5a it can be seen that convergence of the results is achieved for q_c. The refinement from Mesh 1b to Mesh 00 results in a noticeable difference in q_c, whereas further refinement of

Area 1 from Mesh 00 to Mesh 1a has almost no effect on q_c. Interestingly, a change in mesh size of Area 1 also leads to changes in f_s, as can be seen in Figure 5.5b.

Figure 5.5c shows that a different mesh size of Area 3 has very little influence on cone resistance results. However, the sleeve friction results of Figure 5.5d are peculiar. f_s values are quantitatively in an expected order of magnitude with the friction ratio being around 1% to 2%, which is common for sands according to Robertson (2010). However, instead of a convergence of the results when Area 3 is refined, it seems to cause inconsistencies of f_s. Mesh 3a and 3b are very comparable, whereas the intermediate mesh size Mesh 00 shows a large deviation. It would be expected that results from Mesh 3a and Mesh 00 are more closely related to each other than to Mesh 3b, but the opposite appears to be the case. This begs the question what the cause of these discrepancies in sleeve friction results could be, also because quantitatively speaking the results differ substantially. Without a proper explanation as to why the numerical setup leads to large differences, sleeve friction results cannot be reliably obtained from the model. A further investigation into the sleeve friction is required.

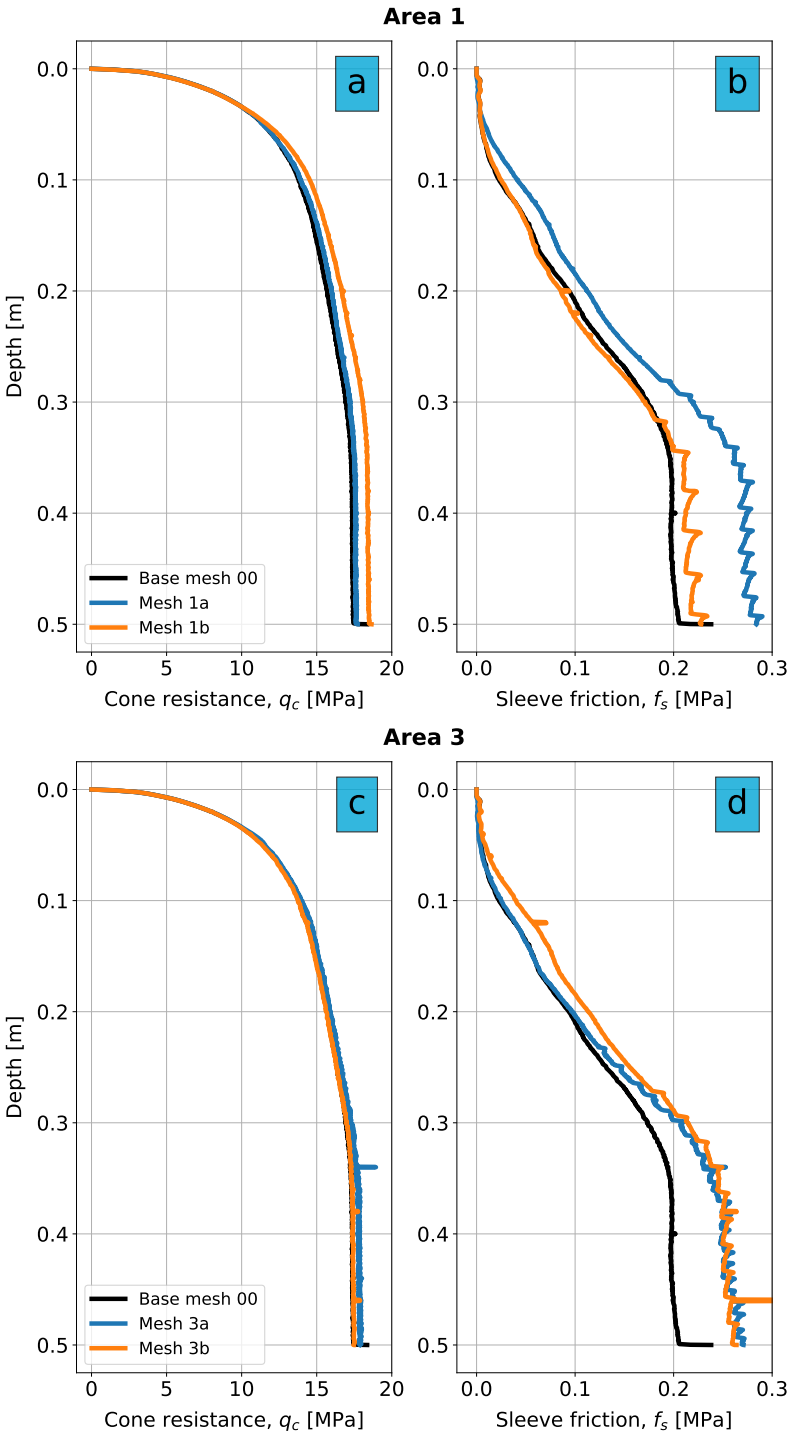

Figure 5.5: Depth vs. cone resistance and sleeve friction results of the mesh size analysis for Area 1 and 3. Constitutive model used: NorSand.

Beside Areas 1 and 3, it is also relevant to investigate whether a finer or coarser mesh deeper in the domain results in a difference in results at those locations. To investigate this, three contour plots of the mean effective stress are shown in Figure 5.6 for Mesh 00, Mesh 5a and Mesh 5b. Here it can be seen that changing the mesh deeper in the domain results in little difference in the stress distribution around the cone. To further support this, Figure 5.7 shows the mean effective stress for the three meshes plotted over two different horizontal lines through the domain. The depth of the horizontal lines is indicated in the Figures with H. Figure 5.7 shows that the influence of the mesh size on the mean effective stress distribution deeper in the domain is negligible. It is therefore concluded that Mesh 00 has a sufficient mesh size for areas located deeper in the domain.

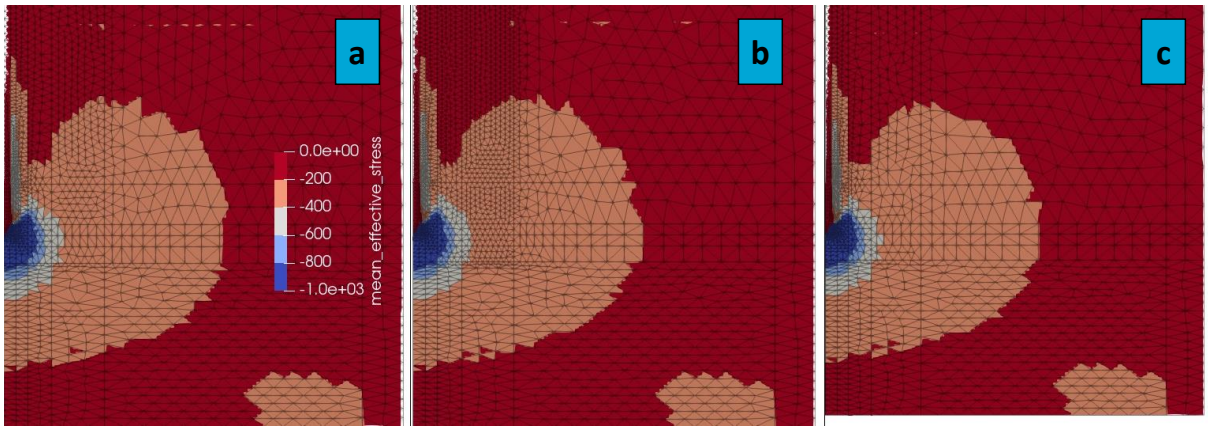

Figure 5.6: Contour plot of the mean effective stress for (a) Mesh 00, (b) Mesh 5a, (c) Mesh 5b. Constitutive model used: NorSand.

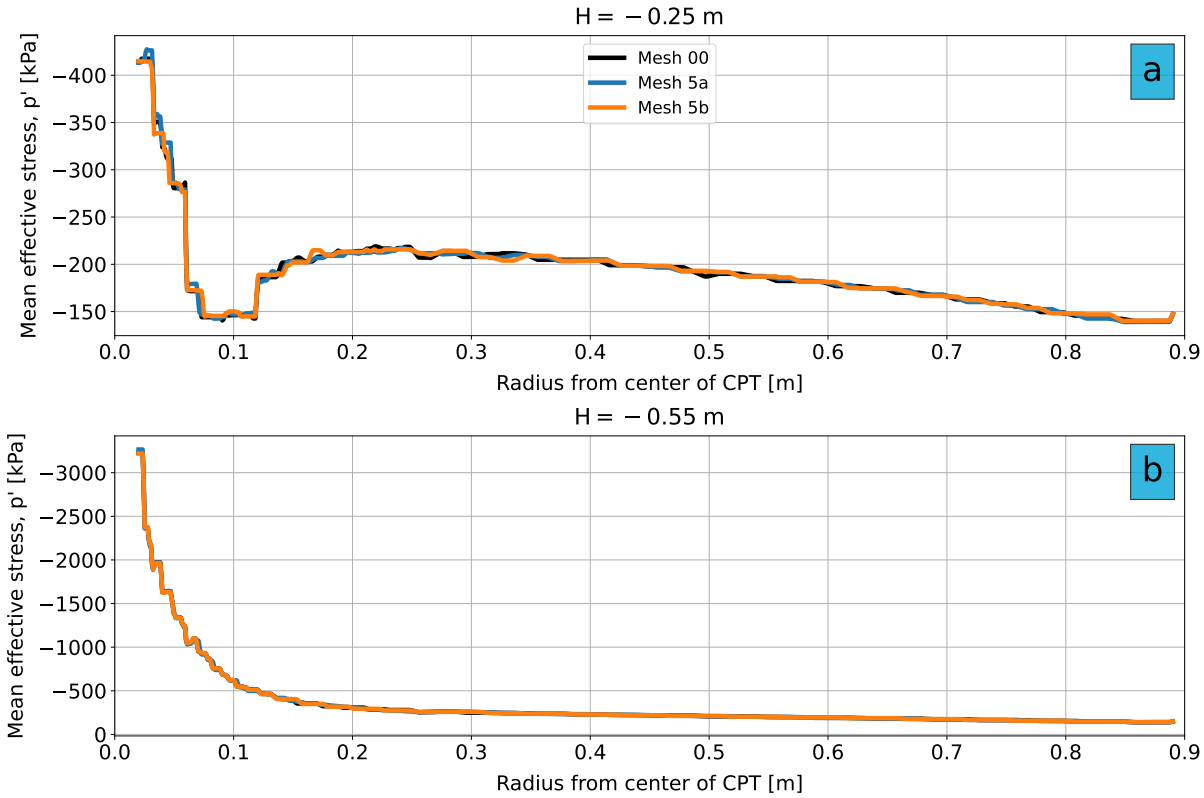

Figure 5.7: Mean effective stress evolution through the domain at a depth of (a) −0.25 m, and (b) −0.55 m. Constitutive model used: NorSand.

5.3.3 Sleeve friction investigation

Because of the complexity of the MPM program it is difficult to immediately identify the cause of the discrepancies of the sleeve friction results. Three possible explanations are proposed and further investigated:

1. The sharp edge of the cone causes a localisation in the domain around this sharp edge. This can result in inaccuracies of the calculations at this location. When a MP is pushed through this localisation it can translate into inaccurate calculations along the shaft.

2. The current implementation of NorSand is not able to accurately account for the rapid unloading behaviour occurring next to the shaft.

3. The triangular elements with linear shape functions are too simplistic for the complex processes at the edge of the cone tip and next to the shaft.

Sharp cone edge

Sometimes sharp edges in the domain of the MPM can cause localisation to occur around that sharp edge. One possibility for the discrepancies observed in the sleeve friction results could be that such a localisation occurs at the transition region from the cone to the sleeve. At this location the cone makes a sharp angle of 60° (see Figure 3.2). If a localisation were to be present around this sharp edge, a change in mesh size next to the sleeve could alter the localisation and by doing so affect sleeve friction results.

To investigate if a localisation is present due to the sharp edge of the cone an experimental new cone shape is introduced, shown in Figure 5.8. This new cone shape is more rounded. Instead of a sudden sharp angle of 60° the rounded cone transitions towards the shaft more gradually. The expectation is that if the sharp edge is cause of a localisation, the rounded cone mitigates this because now no sharp edges are present at the transition between cone and shaft.

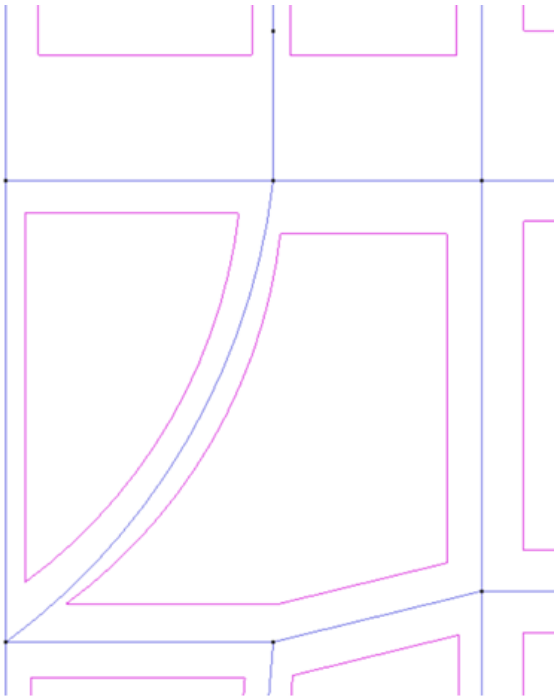

Figure 5.8: Geometry of the experimental round cone.

A series of new calculations are performed with the rounded cone for Areas 1 and 3. The results of these calculations are shown in Figure 5.9. When focusing on Figure 5.9d it can be clearly seen that the inconsistencies in f_s results are still present when the round cone is used in the simulations. Therefore, it is concluded that a localisation due to the 60° angle at the edge of the cone is not the cause of the discrepancies observed in f_s results.

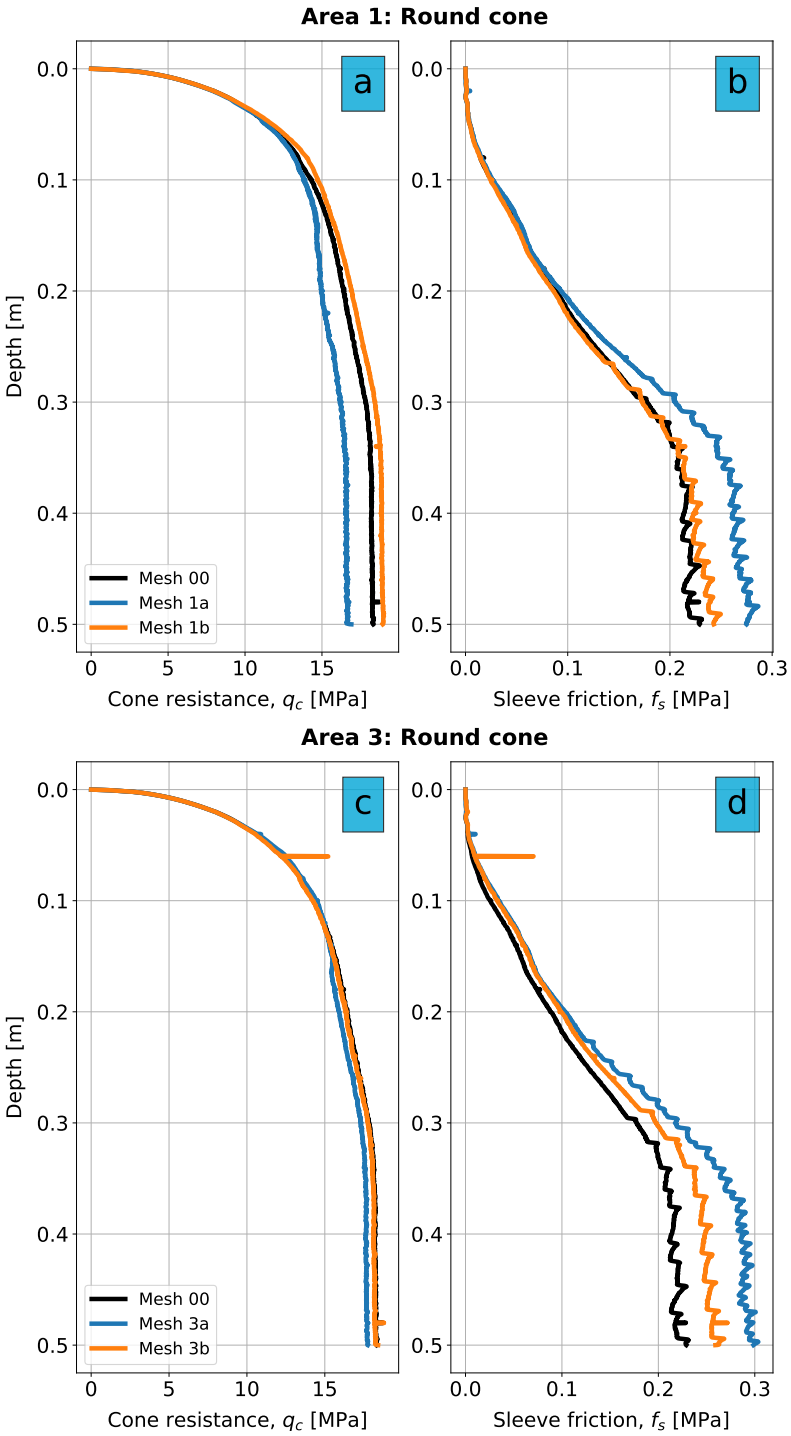

Figure 5.9: Depth vs. cone resistance and sleeve friction results of the mesh size analysis for Area 1 and 3 using the experimental round cone. Constitutive model used: NorSand

Constitutive model

Another potential cause which is suggested is the inability of the constitutive model to accurately model the unloading behaviour of the soil next to the shaft. When a MP is pushed aside by the cone the stresses at that MP decrease rapidly because the cone is no longer exerting a force on the MP. It could be that the magnitude and the speed of the unloading next to the shaft are cause for inconsistencies in the constitutive equations and that the current implementation of NorSand is not adequately capable in modelling this soil behaviour. If the mesh size is then changed it could lead to the inconsistencies shown in Figure 5.5d.

To evaluate if the fault lies with the constitutive model a comparison is made with another, more simple constitutive model from which it is known that the implementation is correct. This model is the Mohr-Coulomb (MC) model. If the inconsistencies are caused by the constitutive model it is expected that sleeve friction results become more consistent when the MC model is used.

Before discussing the results it must be noted that the results of the two different constitutive models should not be quantitatively compared to each other. Besides the fact that the two models are completely different, they are also not calibrated to the same sand and therefore comparing the two quantitatively is meaningless. The only comparison that should be made is to see if sleeve friction results become more consistent and show convergence or not when using MC, qualitatively speaking.

The results of the calculations using the MC model are shown in Figure 5.10. Figure 5.10d shows that the change in mesh size of Area 3 does not result in the deviations of the sleeve friction as is the case in Figure 5.5d. The refinement of Mesh 3a also seems to lead to convergence. Unfortunately it could not be tested if a final convergence has occurred by further refining Mesh 3a, because that would lead to empty active elements. Nevertheless, it can be concluded that the simulations of f_s with MC are more consistent and that the current implementation of NorSand can be the cause for the discrepancies in sleeve friction results.

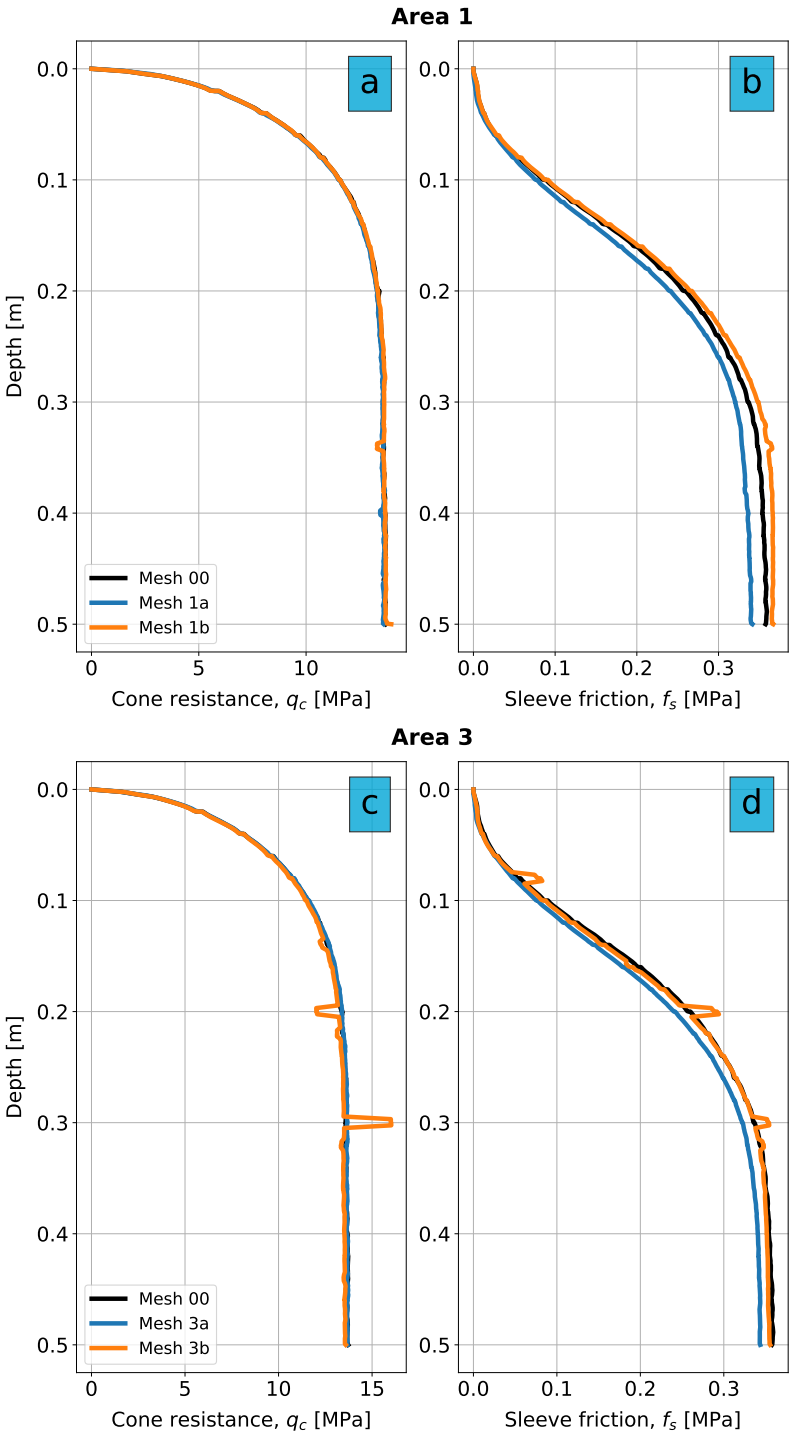

Figure 5.10: Depth vs. cone resistance and sleeve friction results of the mesh size analysis for Area 1 and 3. Constitutive model used: Mohr-Coulomb.

Element type

The last possibility that is investigated is the type of element that is used in the analysis. Up until now triangular elements are used in all analyses. This is initially the case because this element type is also used in previous research (Martinelli & Galavi, 2021). Another element type that could be used are quadrilateral elements. Quadrilateral elements are generally more robust as they contain 4 Gauss points compared to a single one in triangular elements, and an additional node (4 compared to 3). The mesh size used in the quadrilateral mesh is of a comparable size of the ones reported in Table 5.2, so an accurate comparison between the different mesh types can be made. The B-Bar method is used in quadrilateral elements to prevent anti-volumetric locking in the system if that were to be present.

The results when using quadrilateral elements are shown in Figure 5.11. From Figures 5.11b and 5.11d it becomes apparent that using quadrilateral elements does not result in more consistent f_s values. There is also no convergence when Area 3 is refined, as can be seen in 5.11d. It is therefore concluded that the type of element which is used is not the cause of the discrepancies in sleeve friction results.

Beside the sleeve friction results another interesting aspect is visible. This is the quantitative difference in q_c between triangular and quadrilateral elements, visible in Figures 5.11a and 5.11c. This quantitative difference is larger than 10% and is something that cannot be ignored. Because of this, a second investigation in the numerical verification phase is performed to see whether it can be determined what the cause of this difference is.

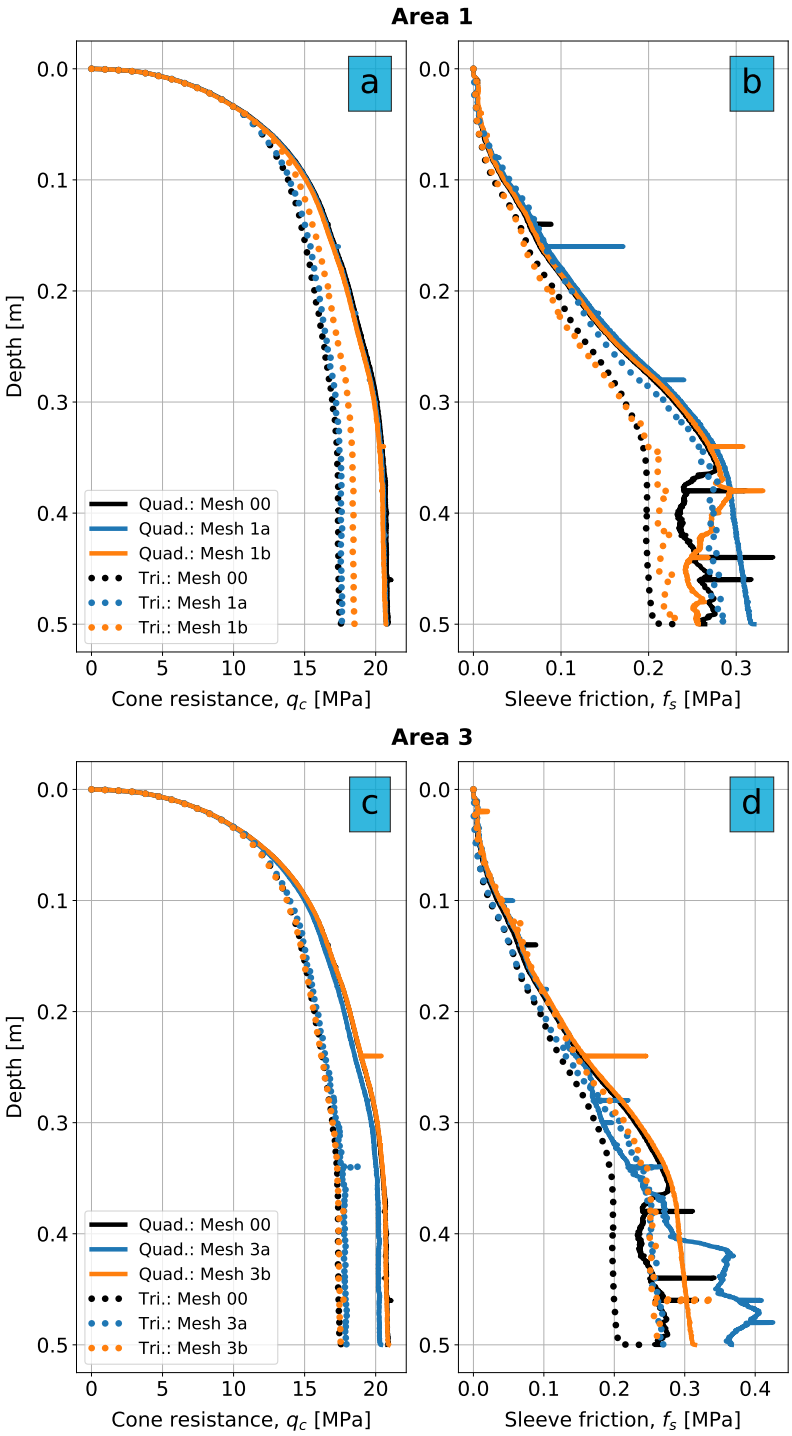

Figure 5.11: Depth vs. cone resistance and sleeve friction results of the mesh size analysis for Area 1 and 3 using quadrilateral elements. Constitutive model used: NorSand.

5.4 Element type analysis

Initially two causes can be identified for the quantitative difference of q_c between the different element types:

1. The mesh size of Area 1 is not enough refined and convergence of q_c still has to occur.
2. The different anti-volumetric locking techniques used for the different types of elements is the reason for the different q_c results.

The first possibility can be discarded as a possible cause by examining Figure 5.11a. Here it can be seen that there is no noticeable difference between Mesh 00, 1a and 1b for quadrilateral elements, which implies that convergence of the results has occurred and that Mesh 00 can already be regarded as an optimal mesh size for Area 1.

This leaves the anti-volumetric locking techniques to be investigated.

5.4.1 Investigation into anti-volumetric locking techniques

To prevent volumetric locking in the system anti-volumetric locking techniques can be selected (see Section 2.1.6). For triangular elements this is the strain smoothing (SS) procedure. For quadrilateral elements the B-Bar method is used.

To determine what the effect of the different techniques is on cone resistance results a series of model runs are performed using the two element types and disabling or enabling the anti-volumetric locking technique. This is also performed for different soil states. In this analysis only the cone resistance is considered because the sleeve friction was previously determined to be quantitatively inconsistent. The results of the investigation for NorSand are shown in Figure 5.12.

Figures 5.12a, 5.12b and 5.12c show the results for different initial state parameters. From these Figures it becomes evident that the quantitative difference between triangular and quadrilateral elements observed in Figure 5.11a is also present in these plots. When SS is used for triangular elements q_c decreases compared to disabling SS. This can be explained by looking in more detail to what exactly happens under the cone when SS is enabled.

If SS is used, volumetric strains are averaged between elements which share nodes. This is useful because by doing so it eliminates the volumetric locking of an element, but it neglects the fact that during a CPT there are large differences in stresses and strains in a close area around the cone. An example of this can be seen in Figure 5.7b, where it is clearly visible that a small move into the domain when close to the cone (1 to 2 cm) results in a large decrease of mean effective stress. The averaging of volumetric strains over adjacent elements will have a noticeable effect on stresses near the cone, as the average element size in Area 1 is around 0.5 cm. Ultimately the use of SS will result in a decrease of the volumetric strains and stresses near the cone, leading to a lower cone resistance when SS is used. Quadrilateral elements do not experience this phenomenon because instead of SS the B-Bar method is used to mitigate volumetric locking. The B-Bar method solves volumetric locking internally in the element, and there is no averaging between adjacent elements. This is why the results in Figure 5.12 with quadrilateral elements are almost identical to the results of triangular elements when SS is disabled.

Having identified strain smoothing as the cause of the quantitative difference in q_c between the element types it raises the question of whether it should be used in the calculations or not. To gain further insight into the way strain smoothing influences q_c values, a comparison with a different constitutive model is made. This time a more advanced constitutive model is desired compared to the sleeve friction investigation, as stress dependency of the stiffness now also needs to be taken into consideration. This is because q_c is a function of the stress and stiffness

under the cone and a more advanced description of these will help to obtain a better understanding of how SS influences q_c. The constitutive model that will be used for this investigation is the Hardening Soil (HS) model (Schanz et al., 1999). The results of this investigation are shown in Figure 5.13. It must be noted that the results of NorSand and HS should not be quantitatively compared to each other and only the effect the anti-volumetric locking on the results should be assessed.

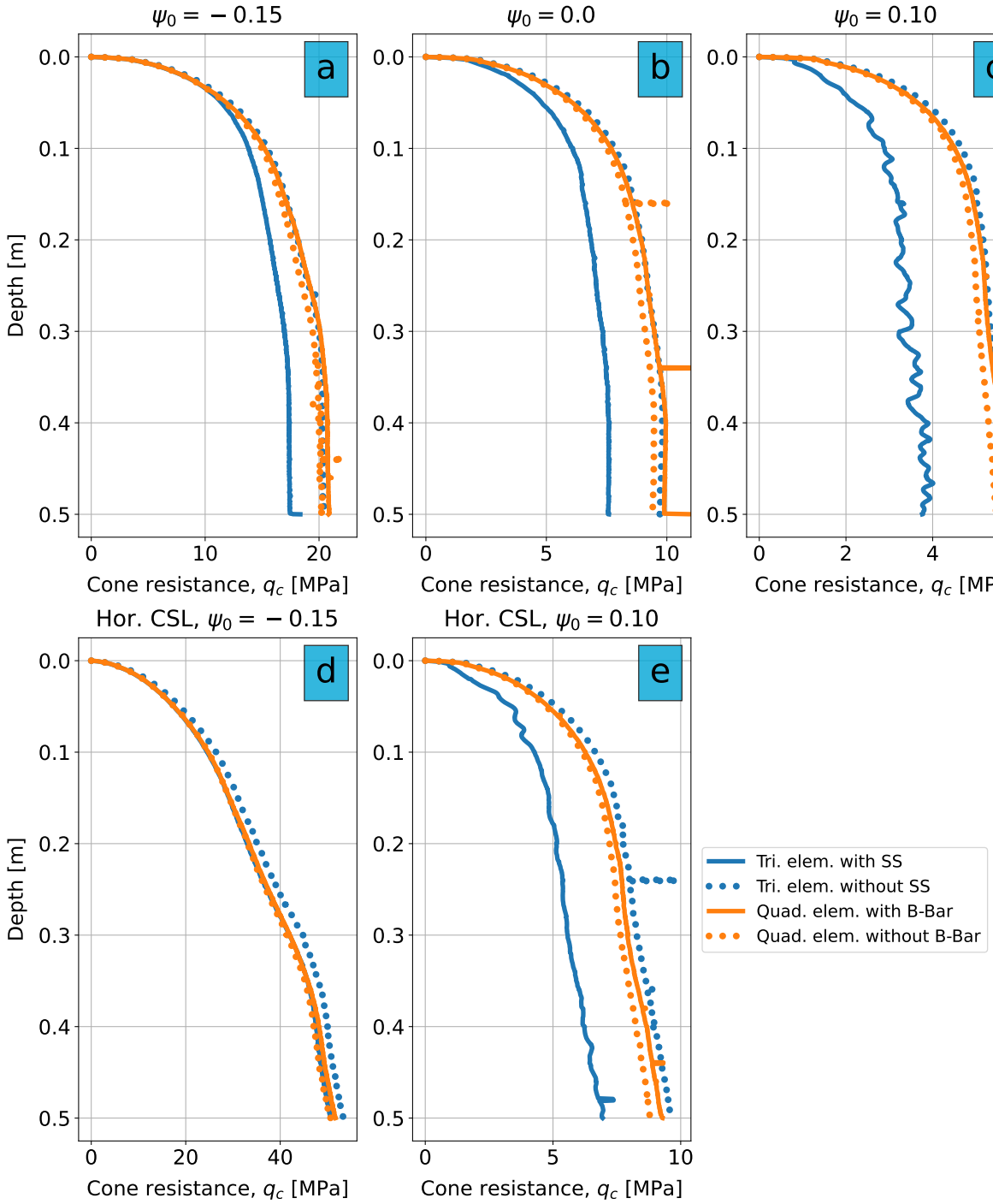

Figure 5.12: Results of the investigation into the anti-volumetric locking techniques. Constitutive model used: NorSand.

The simulations with HS are performed for a series of different dilation angles. The dilation angle in HS controls the dilatancy in the system. A positive dilation angle describes dense sand with a volume expansion and a negative dilation angle loose sand with volume contraction.

Interestingly, it can be seen in Figures 5.13a and 5.13b that when a dense sand is modelled the difference between using SS or not is almost negligible when HS is used, in contrast to when NorSand is used (Figure 5.12a). When lower and eventually negative values are used it can be seen that the difference between using SS increases. In all scenarios the differences between using the B-Bar method or not for quadrilateral elements are relatively small.

The presence of a localisation under the cone can be an explanation for the observed results. The prescribed velocity of the CPT can be cause for the development of this localisation layer directly under the cone. In hindsight, the presence of a localisation layer under the cone is likely also the reason why there are such large differences in stress distribution directly under the cone, and why SS has such a large effect on the cone resistance when NorSand is used in Figure 5.12. The results with HS show that the dilatancy associated with dense sand mitigates the localisation for a large part because there is hardly any difference between enabling or disabling SS. In contrast, the compaction associated with looser sand seems to enhance the localisation layer. Figures 5.13c, 5.13d and 5.13e show that when SS is not used the compacted localisation layer results in a higher cone resistance. If SS is used, the cone resistance is reduced. The effect of SS becomes larger as the compaction in the system increases (i.e. the dilation angle decreases), showing the enhancement of the loose sand on the localisation. When quadrilateral elements are used the results are more consistent and it looks like the enhancement of the localisation is less prominent when loose sand is modelled.

Results of HS show that the dilatancy of the soil influences the localisation under the cone. However, this is not observed for NorSand in Figures 5.12a, 5.12b and 5.12c. For an initially dense sand, the use of SS still leads to a decrease in q_c, in contrast to HS results. The reason for this is the curvature of the CSL in NorSand. When the stress path touches the CSL in e-p' space, the curvature of the CSL ensures that there will always be some sort of compaction under the cone. Because of this the compacted localisation layer is maintained and SS will reduce the cone resistance. To confirm this hypothesis two tests with NorSand are performed with an experimental horizontal CSL (i.e. with soil parameters $\lambda_c = 0$ and $\xi = 0$) for a dense and loose sand. By doing this the CSL becomes independent of the stress level and no compaction due to the curvature of the CSL can occur. The results of this analysis are shown in Figures 5.12d and 5.12e. Again, it is observed that for a dense sand the localisation is mitigated whereas it is maintained in a loose sand. This confirms once more the influence of dilatancy on the localised compaction under the cone, but this time with NorSand.

Figure 5.14 shows a contour plot of the volumetric strains around the cone. It can be clearly seen from Figure 5.14a that when SS is enabled the localisation of volumetric strains at the cone tip is reduced. Figure 5.15 shows how the smoothing of volumetric strains changes the stress distribution under the cone. Clearly lower stress levels are observed in Figure 5.15a compared to 5.15b where SS is disabled.

It is decided to perform the simulations in the validation phase with quadrilateral elements using the B-Bar method. The results with quadrilateral elements are consistent for a wide range of scenarios. Figure 5.12 shows little difference between using the B-Bar method or not, indicating that little volumetric locking is present when using quadrilateral elements. Nevertheless, it is decided to enable the B-Bar method to prevent volumetric locking if it were to be present in different situations.

The mesh size that will be used in the quadrilateral mesh is equivalent to Mesh 00 of triangular elements. Figure 5.11a showed that there is practically no difference in q_c between Mesh 00 and Mesh 1a used quadrilateral elements. Changing the mesh size of Area 1 does slightly

change the localisation under the cone, as can be seen in Figure C.3. However, this does not seem to affect the obtained q_c values. A comparison of the mesh size deeper in the domain of Area 5 is also conducted for quadrilateral elements. The contour plot of different mesh sizes for Area 5 is shown in Figure C.4. Little difference is observed between the stress distribution deeper into the domain, indicating that Mesh 00 for Area 5 is a sufficient mesh size.

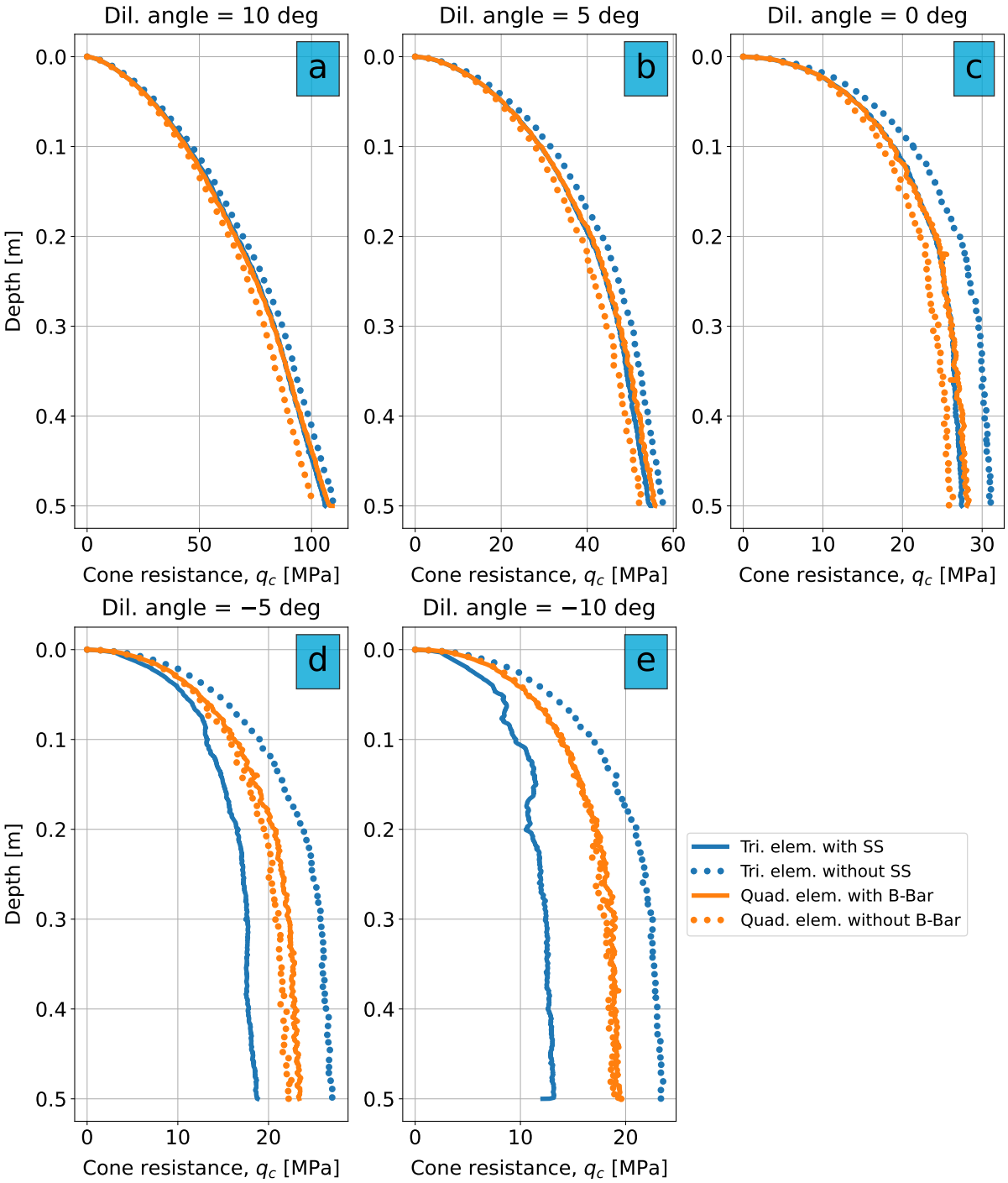

Figure 5.13: Results of the investigation into the anti-volumetric locking techniques. Constitutive model used: Hardening Soil.

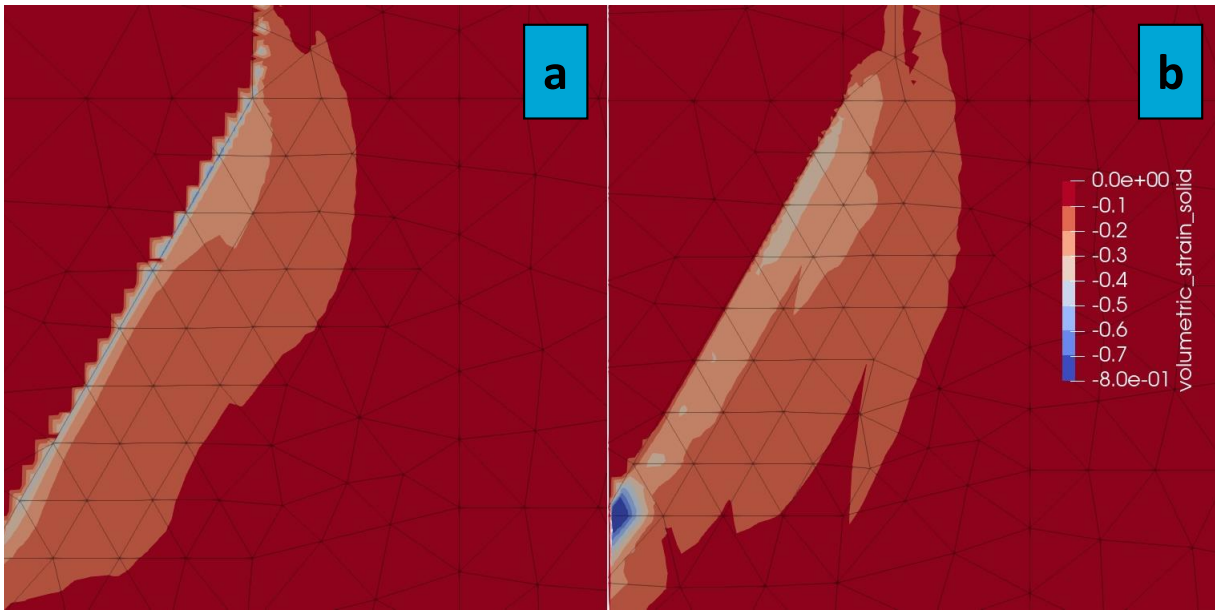

Figure 5.14: Contour plot of the volumetric strain around the cone tip for triangular elements at the last time step with (a) strain smoothing enabled, (b) strain smoothing disabled. Constitutive model used: NorSand.

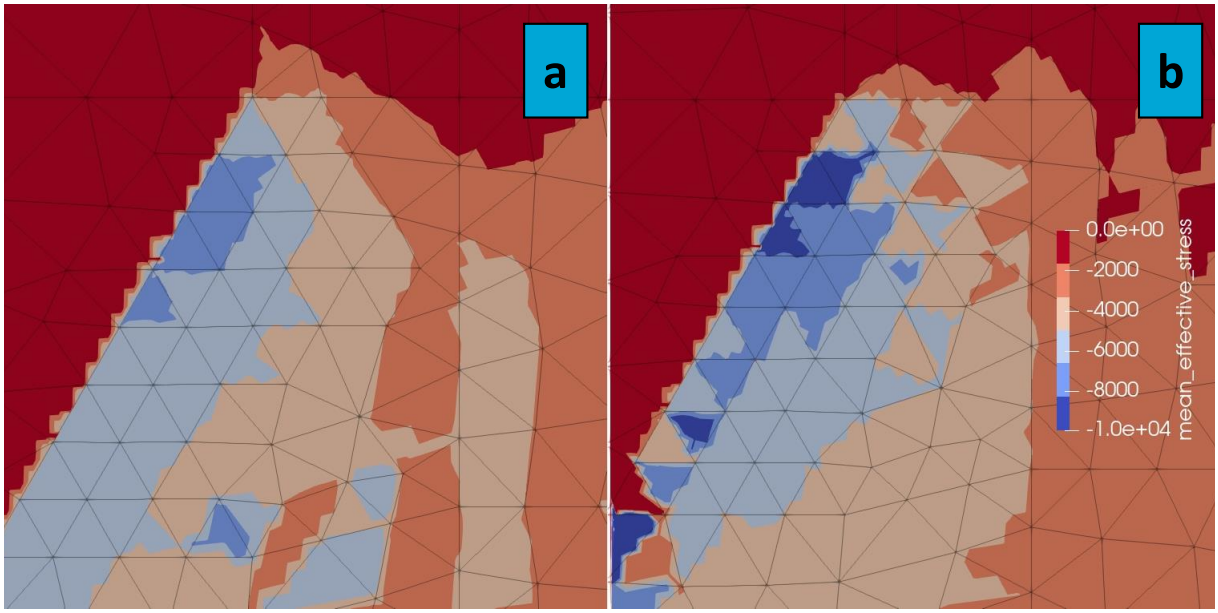

Figure 5.15: Contour plot of the mean effective stress around the cone tip for triangular elements at the last time step with (a) strain smoothing enabled, (b) strain smoothing disabled. Constitutive model used: NorSand.

5.5 Conclusion of the numerical verification phase

The goal of the numerical verification phase was to determine the optimal numerical calculation settings and setup.

For the determination of the numerical calculation settings three sensitivity analyses were performed.

1. It has been shown that the difference between the MPM-Mixed and MPM-MP integration method is minor, while the computational time of the MPM-Mixed method is considerably lower. Therefore, the MPM-Mixed integration scheme will be used for future analysis.

2. The MSF sensitivity analysis showed that is was possible to increase the MSF to a value of $\text{MSF} = 10000$ to reduce the calculation time without compromising model results.

3. The investigation into the damping factor proved that a damping factor of 0.1 in combination with an energy dissipation constitutive model is sufficient to account for the damping in the system.

The optimal numerical setup was determined by performing a mesh size analysis. The mesh size analysis showed that sleeve friction results cannot be reliably quantified because the numerical setup influences these results substantially. A further investigation showed that the cause of these discrepancies is related to the constitutive model.

Furthermore, a quantitative difference was observed between using triangular and quadrilateral elements. The cause of this quantitative difference was identified to be the strain smoothing procedure used for triangular elements to prevent volumetric locking. A deeper investigation into the different anti-volumetric locking techniques resulted in the discovery of a localisation layer due to compaction of the prescribed penetration of the CPT under the cone. The localisation is found for both the NorSand and HS constitutive models. The effects of the localisation are reduced when dense sand is modelled but are enhanced for loose sand. Due to the curvature of the CSL in NorSand the localisation is maintained, even when dense sand is modelled.

The optimal numerical setup proved to be the use of quadrilateral elements with the B-Bar method enabled to mitigate any potential volumetric locking. This setup avoids sharing volumetric strains with adjacent elements, as would be the case when applying triangular elements with the strain smoothing procedure. A mesh size equivalent to Mesh 00 was sufficient to accurately perform the simulation.

6

Boundary Condition Analysis

In this Chapter the results of the boundary condition (BC) analysis are presented. The goal of this phase is to assess how different boundary conditions affect model results and whether this corresponds to what has been reported in literature about the boundary conditions of calibration chamber (CC) tests. The insights that can be obtained in this phase are useful to optimally set up the model domain in future analyses if it is desired to model free-field conditions.

The boundary condition analysis can be divided into two parts:

1. Investigation into the bottom boundary.
2. Investigation into the lateral boundary.

In this Chapter the most important results will be shown and discussed. The additional results are shown in Appendix D.

Because the numerical settings are kept constant for all scenarios in this Chapter, changes in model results can be completely attributed to a change in boundary conditions.

6.1 Bottom boundary condition

The bottom boundary is indicated by the red line in Figure D.1. Two boundary conditions can be selected for the bottom boundary:

1. Smooth boundary condition.
2. Rough boundary condition.

A smooth boundary condition means that the boundary is fixed for movements perpendicular to the boundary, but the material is able to move parallel to the boundary. For the rough boundary both movements perpendicular and parallel to the boundary are fixed.

To investigate what the effects are of using these different boundary conditions a calculation is performed for both situations. The results are compared with a situation where the depth of the chamber is enlarged from 1 m to 2 m, and the CPT penetration is increased from 0.5 m to 1 m. Subsequently all results will be compared at a depth of 0.5 m. In the enlarged domain the bottom boundary will have a smaller influence on the model results at a depth of 0.5 m.

The results of the investigation of the bottom boundary conditions are shown in Figure 6.1. From examining Figures 6.1a and 6.1b it becomes apparent that using a rough boundary condition for the bottom boundary results in almost identical q_c values compared to the results of the deeper domain. At deeper penetration depths the smooth boundary condition shows a decreasing cone resistance. The explanation for this is that when a smooth boundary condition is used the bottom boundary is less capable in mobilising a reaction force due to the movement of the soil parallel to the bottom boundary. Similar results are observed for the sleeve friction in Figures 6.1c and 6.1d.

Due to the close agreement in results between the simulation with a deeper domain and a rough bottom boundary condition, it can be concluded that using the rough boundary condition results in q_c values which are closest to a situation where less boundary effects are present. Therefore, if it is desired to model free field conditions the rough bottom boundary condition can best be applied.

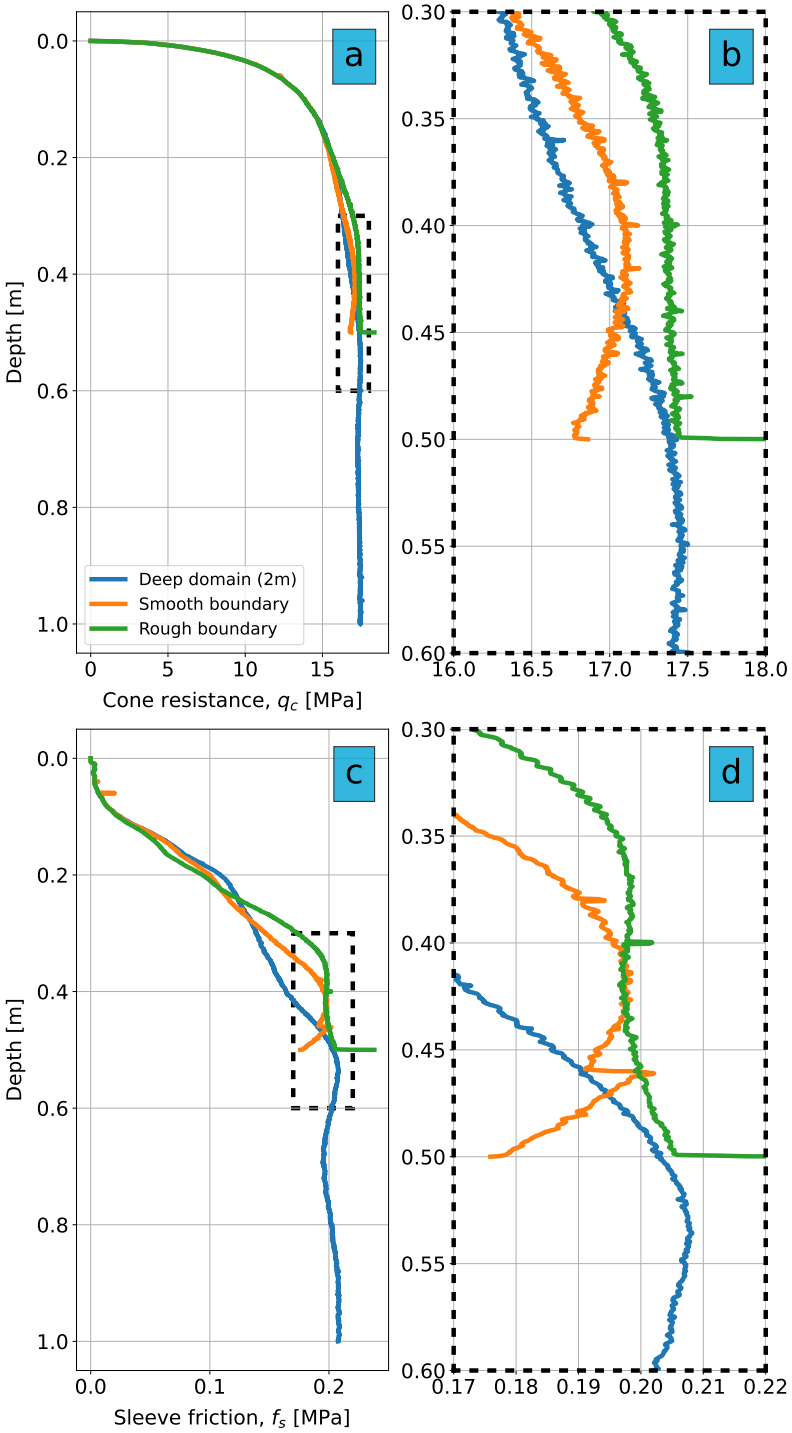

Figure 6.1: Results of the different bottom boundary conditions. (a) q_c results, (b) close up of q_c results, (c) f_s results, (d) close up of f_s results.

6.2 Lateral boundary condition

The investigation of the lateral boundary is more complicated than that of the bottom boundary. The lateral boundary has a more significant influence on the cone resistance than the bottom boundary (Parkin & Lunne, 1982). Depending on the type of lateral boundary condition that is used and the size of the chamber, cone resistance results can be substantially affected. A more thorough investigation is necessary to investigate the lateral boundary condition effects.

6.2.1 Type of lateral boundary condition

Two types of lateral boundary conditions are used in CC tests:

1. Constant lateral stress condition.
2. Zero displacement condition (in literature also referred to as constant volume boundary condition).

In a CC test the lateral stress is controlled by a water jacket. The pressure is build up to give an initial K_0 value. It may be further increased for sand in an overconsolidated state. The lateral stress is maintained at a constant level during the test if a constant lateral stress BC is applied (Parkin & Lunne, 1982). In the MPM model a constant stress BC is achieved by applying a soft additional layer next to the soil. This layer is called the boundary layer in the model. Figures 3.1 and D.1 show where the boundary layer is located in the domain. The properties of the boundary layer are reported in Table 3.2. Because of the additional layer next to the soil, the lateral stress level at the soil boundary is kept approximately constant throughout the simulation, whereas if the boundary layer would be removed the restrictions imposed by the side boundary condition on the soil would cause a change in stress level.

During a CC test, the zero displacement BC is obtained by allowing the water pressure to increase during the testing (Parkin & Lunne, 1982). In the model, the zero displacement boundary condition is obtained by removing the boundary layer from the domain and by applying the rough BC on the side boundary (see Figure D.1).

6.2.2 Chamber size

The size of the chamber has a great impact on results, both during a CC test and in the MPM model. The smaller the chamber, the more noticeable the boundary effects are. A measure to indicate the chamber size is the chamber cone ratio (CCR). The CCR relates the diameter of the chamber to the diameter of the cone. A standard cone has a diameter of $D_c = 3.568$ cm. A chamber with a diameter of e.g. 1.2 m will have a CCR of $120/3.568 = 33.6$.

During CC tests the diameter of the chamber can usually not be changed. The CCR can then still be changed by using a cone with a different diameter. By switching to a cone of e.g. $D_c = 2$ cm (from $D_c = 3.568$ cm), the CCR of the test is changed from 33.6 to $120/2 = 60$. In the MPM model, the CCR of a simulation can be changed by increasing the size of the domain as explained in Section 3.1.3.

The influence of boundary conditions related to the chamber size is often reported in terms of the CCR (Been et al., 1987; Been et al., 1986; Parkin & Lunne, 1982). This will also be the case in this thesis.

6.2.3 Approach and results

To obtain a complete overview of how the lateral boundary effects influence model results, a vast set of calculations are performed as follows:

- Four different CCR values are determined to assess the influence of the chamber size on the model results. These CCR values are 25, 50, 75 and 100.
- At these CCRs, two calculations are performed using BC 1: the constant stress side boundary condition, or BC 2: the zero displacement side boundary condition.
- To investigate the effect of the state of the soil, these calculations are performed for three initial state parameters: $\psi_0 = -0.25$, $\psi_0 = -0.15$ and $\psi_0 = -0.05$.
- To investigate the effect of the initial stress level, the calculations above are performed for two initial effective vertical stress levels: $\sigma'_{v0} = 250$ kPa and $\sigma'_{v0} = 50$ kPa.

The results of the side boundary conditions for the cone resistance are shown in Figure 6.2. Additional results of q_c and f_s over depth plots are shown in Figures D.2, D.3, D.4 and D.5.

Figure 6.2 shows conclusive results of the side boundary condition investigation, which are summarised below.

- Sand in a dense state experiences more effects of boundary conditions than sand in a loose state. The denser the state of a sand, the larger the volume expansion in the system will be due to the penetration of the CPT. This means that the zone of influence in the domain will be greater for dense sands, compared to loose sands. The boundary conditions (regardless if BC 1 or BC 2 is used) will therefore have a larger effect on q_c for dense sand. In Figure 6.2 this can be clearly seen by comparing the results of $\psi_0 = -0.25$, $\psi_0 = -0.15$ and $\psi_0 = -0.05$. The difference in q_c when the CCR is increased from 25 to 50 is greater for $\psi_0 = -0.25$ than for $\psi_0 = -0.15$. In the smaller chamber size of CRR $= 25$ the larger zone of influence for a $\psi_0 = -0.25$ results in a stronger response of the side boundary condition. The response of the BC is less for $\psi_0 = -0.15$, where the looser state of the soil results in a smaller zone of influence. For $\psi_0 = -0.05$ the zone of influence is so small that here is no apparent difference between a CCR of 25 and 50.
- When boundary effects are not negligible, using a constant lateral stress BC results in an underestimation of q_c compared to free-field conditions, whereas a zero displacement side BC results in an overestimation. This can be explained as follows: when the CPT is pushed into the soil, the soil mobilises a reaction force. This force propagates through the domain until it reaches the boundary. The use of a constant lateral stress BC prevents further mobilisation of stresses at the boundary, whereas in free-field conditions this would have been allowed to happen. The reduction of the mobilisation of reaction forces at the boundary results in the underestimation of q_c. The opposite occurs for a zero displacement BC, where a greater mobilisation of reaction forces can be achieved compared to free-field conditions, because in free-field conditions displacements are allowed at the location where the boundary is located in the model, leading to an overestimation of q_c. In the results of Figure 6.2 this can be clearly seen by examining the results at CCR $= 25$. Here q_c for BC 1 is lower than at e.g. CCR $= 75$ (i.e. a better simulation of free-field conditions) if the zone of influence is substantial enough to generate a response from the boundary. The opposite is noticed for BC 2, where q_c is higher at CCR $= 25$ than at e.g. CCR $= 75$.

- For Ticino 4 sand, a value of CCR $= 50$ will be sufficient to mitigate most boundary effects. In Figure 6.2 it can be seen that the q_c values for BC 1 and BC 2 converge towards the same values at larger CCRs. This convergence indicates that free-field conditions have been obtained. At that point there is no difference between the two different types of side boundary conditions, which implies that the influence of the boundary conditions on the MPM results is mitigated. For most scenarios shown in Figure 6.2 this point of convergence is obtained at CCR $= 50$. However, for soil in a state of $\psi_0 = -0.05$ a CCR of 25 is already sufficient to mitigate the boundary effects, due to the small zone of influence of loose sands. On the contrary, soil in a dense state at $\psi_0 = -0.25$ at a lower stress level of $\sigma'_{v0} = 50$ kPa still has about a 10% difference between the different types of BC, indicating that boundary effects still affect q_c at that state.

- Increasing the stress level results in a less noticeable effect of the boundary conditions at lower CCRs. The difference between BC 1 and BC 2 is smaller at $\sigma'_{v0} = 250$ kPa compared to $\sigma'_{v0} = 50$ kPa for $\psi_0 = -0.15$ and $\psi_0 = -0.25$. This can be explained by the differences in the zone of influence between the different stress states. An increase in stress level tends to suppress dilatancy of the soil (Jefferies & Been, 2016). The stronger confinement leads to a decrease in void ratio and prevents volume expansion in the system, therefore decreasing the zone of influence in the domain. The smaller zone of influence at higher stress levels results in a less noticeable effect of the BC on q_c results, decreasing the difference between BC 1 and BC 2 at CCRs when boundary conditions cannot be neglected.

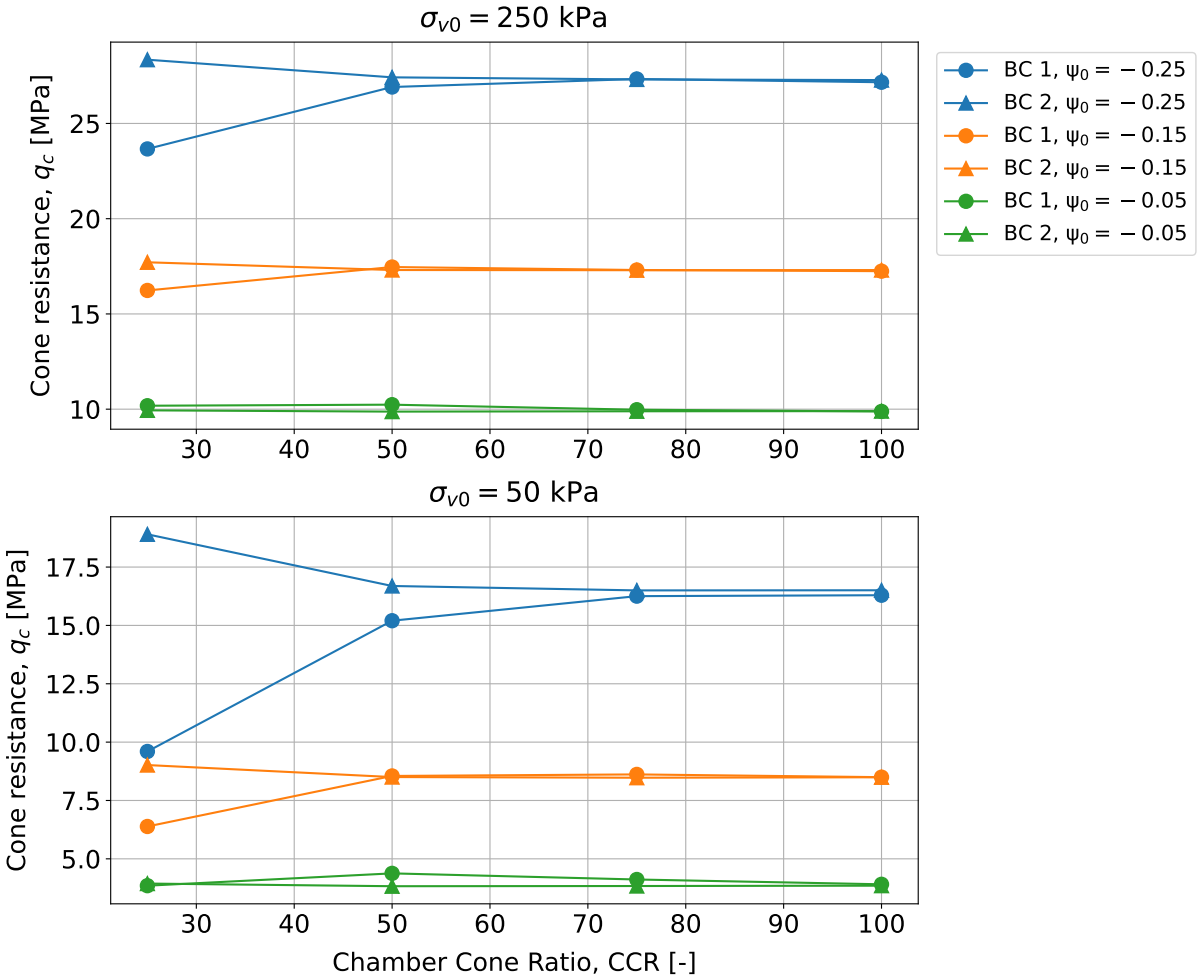

Figure 6.2: Cone resistance results of the lateral boundary condition investigation.

6.3 Conclusion of the boundary condition analysis

The goal of the boundary condition analysis was to evaluate how different types of boundary conditions and domain size affect modelling results. To achieve this goal an investigation into the bottom boundary and the lateral boundary were performed.

The bottom boundary analysis showed that using a rough bottom boundary condition results in the closest similarities to a calculation where the domain is deepened, which indicates the best description to a situation with less boundary effects. In a situation where it is desired to model free field conditions, the rough boundary condition should therefore be used.

The lateral boundary condition investigation confirmed that a number of features regarding boundary conditions in CC tests which are known from literature are applicable to the MPM model, listed below:

- The state of the sand is an important factor influencing the boundary conditions, with dense sand leading to a larger response of boundary effects than loose sand (Been et al., 1986; Parkin & Lunne, 1982).
- The use of a constant lateral stress side BC results in an underestimation of q_c compared to free-field conditions, whereas a zero displacement side BC results in an overestimation (Ahmadi & Robertson, 2008; Parkin & Lunne, 1982).
- An increase in stress level results in the suppression of dilatancy with a smaller zone of influence and less noticeable boundary effects as a result, compared to lower stress levels at a similar CCR (Jefferies & Been, 2016).

The boundary condition analysis qualitatively confirms the correct functioning of the boundary conditions in the MPM model with NorSand. Which type of lateral boundary condition or which CCR should be used in a calculation is specific for the problem at hand. The results of this analysis can provide guidance in making an appropriate choice in selecting the boundary conditions for future analyses.

7

Model Validation

In this Chapter the results of the model validation phase are presented. The goal of this phase is to evaluate whether the cone resistance results of the MPM model are quantitatively in agreement with experimental calibration chamber (CC) test results. The comparison of the model with experimental results will give insight in how well the MPM model is able to produce results which resemble reality.

The validation of the model is performed for four different types of sand, which can be categorised in two groups based on how NorSand parameters are determined and how CC test data is obtained:

1. Sands for which the NorSand parameters are determined from literature according to the parameter determination procedure described in Chapter 4. For these sands the CC test data is also obtained from literature (electronically provided by Jefferies and Been (2016)). These include:
   (a) Ticino 4 sand;
   (b) Ottawa sand;
   (c) Hokksund sand.
2. A sand for which laboratory test data is available. This allows for the direct determination of NorSand parameters. CC tests have also been performed on this sand. This sand is called:
   (d) GEBA sand.

The friction contact angle is set to a value of $\frac{2}{3}\phi_c$ for all different sands.

7.1 CC test data

7.1.1 Stress levels

The CC test data will be filtered on vertical effective stress with a margin of $\sigma'_{v0} \pm 20\%$ to allow for a sufficient amount of datapoints to be present for the validation. The amount of stress levels that are filtered depends on the CC data at hand (e.g. for Ticino 4 sand sufficient data is available to filter three stress levels, whereas for Ottawa sand a representative filter can only be applied to two stress levels). Subsequently, three MPM calculations are performed at different initial densities, similar to the CC test data. The obtained cone resistance results are normalised with respect to the stress level according to Eq. 3.4.

7.1.2 Boundary effects

To account for the different types of boundary conditions that are used for different CC tests, a correction factor is applied to the normalised cone resistance. This correction factor is proposed by Been et al. (1986). The correction factor standardises the cone resistance data to a value that would be obtained when using a chamber size equal to CCR = 50. To ensure consistency between the conducted CC tests and the MPM model, the correction factor is applied to the CC tests in combination with a domain size of CCR = 50 in the MPM model.

A smooth bottom boundary condition is used in all calculations. Using the rough bottom boundary condition led to systematic overestimation of all MPM results, whereas the smooth bottom boundary significantly improved these. It is therefore determined that using a smooth bottom boundary best resembles the conditions of a CC test and it is used in the calculations.

7.1.3 Cone diameter

In the CC test data, sometimes different diameters are used for different tests. To be consistent in the comparison between the MPM model and the CC tests, only CC tests performed with the same cone diameter as is used in the MPM model will be considered. This is the standard cone diameter of $D_c = 3.568$ cm, with a surface area of 10 cm^2 (see also Section 3.4).

7.1.4 Measurement uncertainty

Before discussing the results it is worthwhile to take a look at the uncertainties related to the CC test data. The initial void ratio e_0 is reported for each test. e_0 is normally determined from the dry unit weight γ_d of the sand. For this validation study it is decided to include a margin of uncertainty to the dry unit weight of sand due to measurement errors. The measurement errors in the determination of the unit weight of a soil are usually small compared to other soil properties. Nevertheless, a coefficient of variation of COV $= 1\%$ in unit weight due to measurement errors is not uncommon (Phoon & Kulhawy, 1999). This margin of uncertainty of the dry unit weight due to measurement errors translates further into the calculation of e_0. Based on previous experiences, it is deemed appropriate to assume that a COV $= 1\%$ results in an uncertainty in initial relative density of $\pm 5\%$ (in absolute terms). Knowing this, a margin of uncertainty of the initial void ratio is determined and plotted for each CC test datapoint.

The margin of uncertainty emphasises the importance to acknowledge that it is unrealistic to expect a 'one-on-one' match between MPM results and CC test data. Rather, if the MPM results fall within the region of the uncertainty range, it can be viewed as a sufficient agreement between model results and experimental tests.

7.2 Ticino 4 sand

7.2.1 NorSand parameters

The NorSand parameters of Ticino 4 sand have already been determined in Chapter 4 to illustrate the parameter determination process (see Figures 4.1 and 4.3, repeated in Figures E.1 and E.2).

Table 7.1: NorSand parameters for Ticino 4 sand used in the validation phase.

Parameter [unit]	**Value**	**Parameter [unit]**	**Value**
G_{ref} [-]	482	ϕ_c [°]	31.6
ν [-]	0.2	N [-]	0.40
a [-]	0.5	H [-]	$70 - 200\psi_0$
e_Γ [-]	0.93	χ_{tc} [-]	3.0
λ_c [-]	0.045	$F_{e,fac}$ [-]	0
ξ [-]	0.56	$e_{el,min}$ [-]	0.20

7.2.2 Validation results

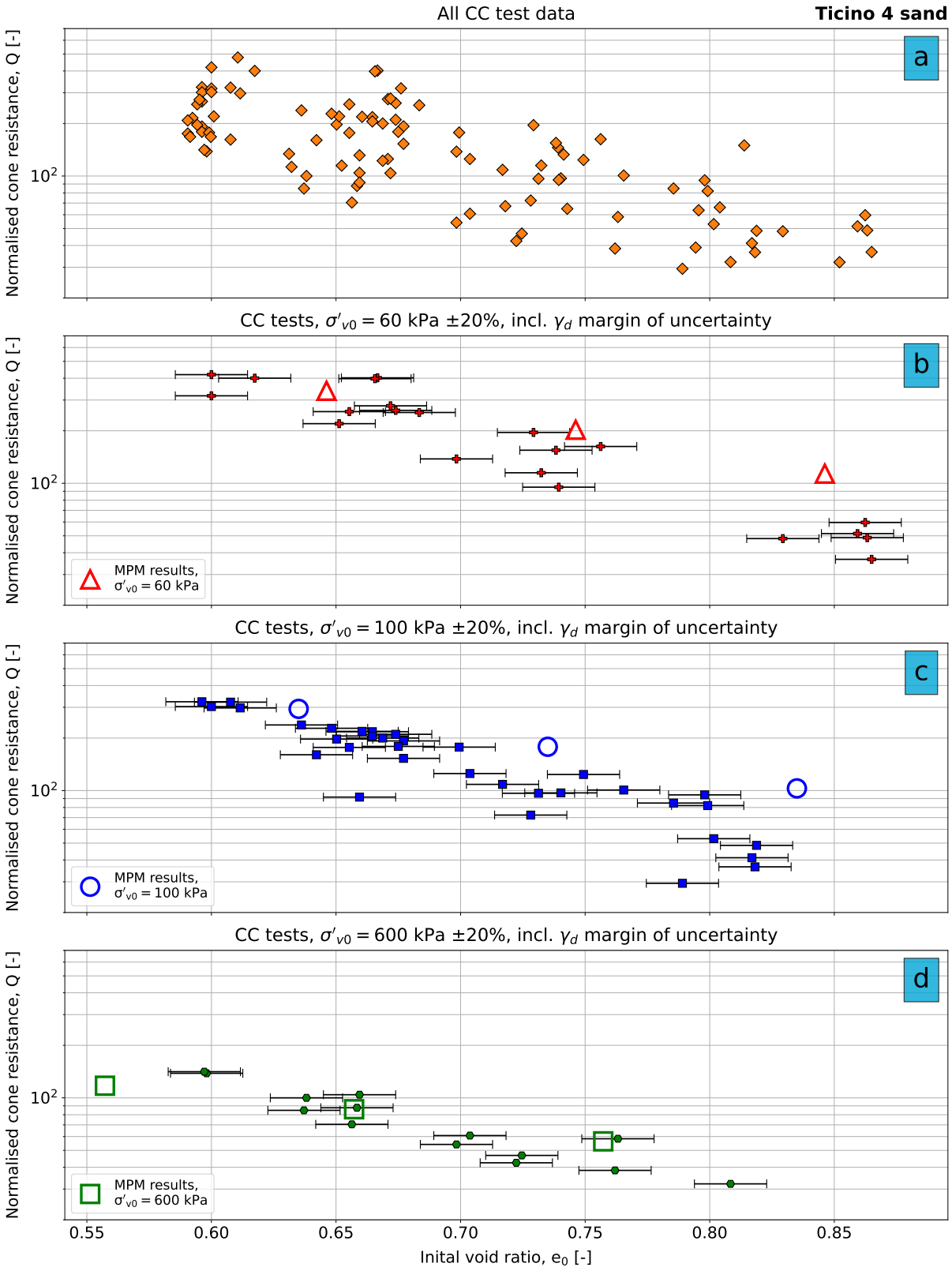

Figure 7.1: Results of the validation of Ticino 4 sand. CC test data from Baldi et al. (1986). Electronically shared by Jefferies and Been (2016).

For Ticino 4 sand the largest amount of CC tests are conducted of all sands in this validation phase (see Figure 7.1a). This allowed to perform the MPM calculations at three different stress levels, namely $\sigma'_{v0} = 60$ kPa, $\sigma'_{v0} = 100$ kPa and $\sigma'_{v0} = 600$ kPa. The CC tests are performed and reported by Baldi et al. (1986), and electronically shared by Jefferies and Been (2016).

Figure 7.1b shows that at $\sigma'_{v0} = 60$ kPa for a low and intermediate initial void ratio the MPM results are in good agreement with the CC test data. At a higher initial void ratio the difference between the MPM results and CC tests is larger. The decrease of Q with increasing e_0 is larger for the CC tests than for the MPM calculations. This is similar at a slightly higher stress level of $\sigma'_{v0} = 100$ kPa, as can be seen in Figure 7.1c. When the stress level is increased substantially to $\sigma'_{v0} = 600$ kPa in Figure 7.1d there is hardly any difference between the MPM results and CC test data, even at higher values of e_0.

Overall, the MPM results of Ticino 4 sand show a good agreement with CC test results for sand states which can be categorised as moderately-dense to dense (corresponding to approximately $\psi_0 \leq -0.10$). At lower relative densities there seems to be an overestimation of the cone resistance at the lower stress levels of $\sigma'_{v0} = 60$ kPa and $\sigma'_{v0} = 100$ kPa. This overestimation for looser sand is not the case when the stress level is increased to $\sigma'_{v0} = 600$ kPa.

7.3 Ottawa sand

7.3.1 NorSand parameters

In Table 7.2 the NorSand parameters for Ottawa sand are presented. In Figures E.3 and E.4 the results of the parameter determination for Ottawa sand are shown.

Table 7.2: NorSand parameters for Ottawa sand used in the validation phase.

Parameter [unit]	Value	Parameter [unit]	Value
G_{ref} [-]	418	ϕ_c [°]	30.9
ν [-]	0.2	N [-]	0.45
a [-]	0.5	H [-]	$180 - 400\psi_0$
e_Γ [-]	0.72	χ_{tc} [-]	4.0
λ_c [-]	0.018	$F_{e,fac}$ [-]	0
ξ [-]	0.56	$e_{el,min}$ [-]	0.20

7.3.2 Validation results

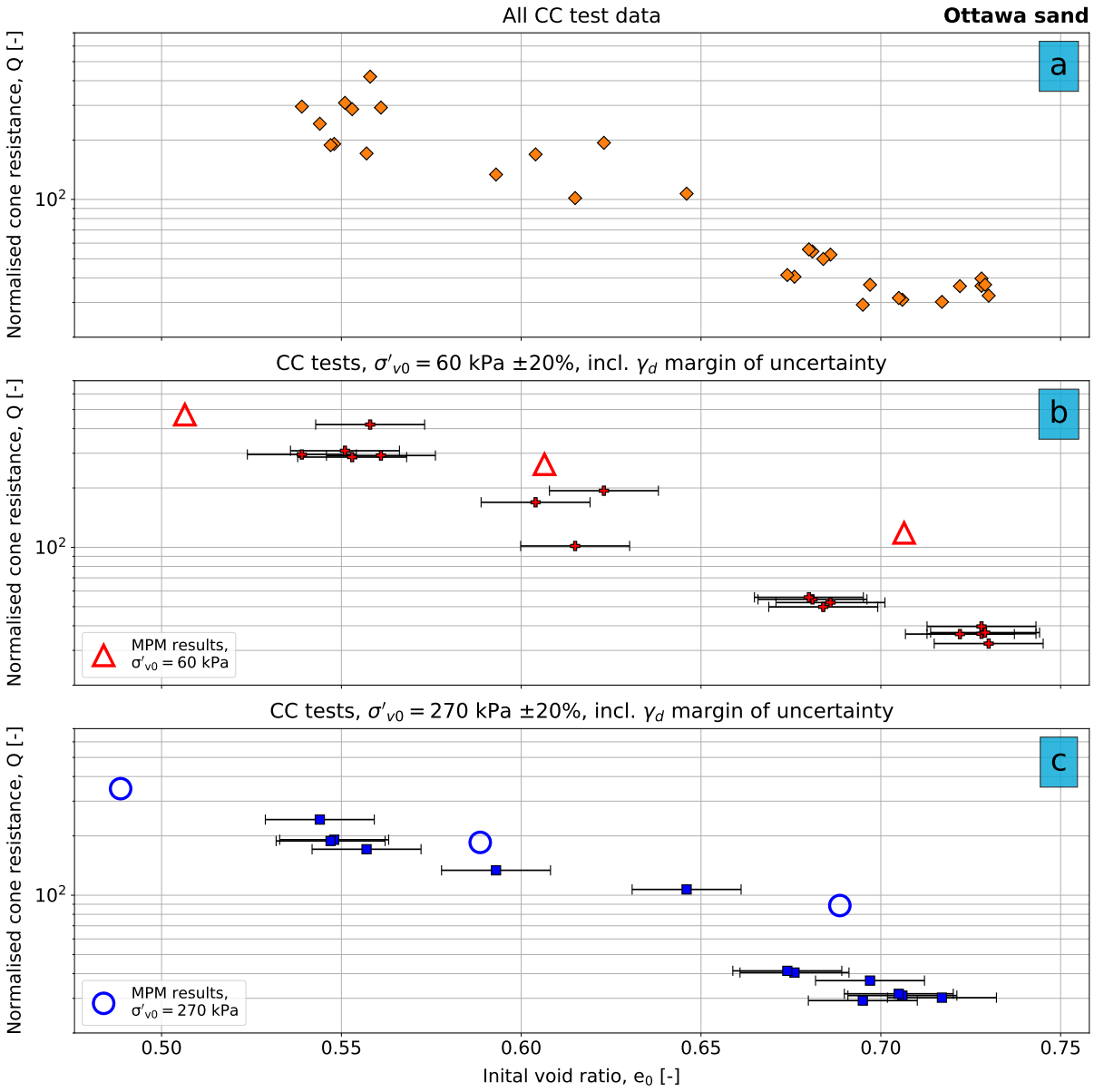

Figure 7.2: Results of the validation of Ottawa sand. CC test data from Harman (1976), as cited in Jefferies and Been (2016). Electronically shared by Jefferies and Been (2016).

The CC tests of Ottawa sand are filtered for two stress levels: $\sigma'_{v0} = 60$ kPa and $\sigma'_{v0} = 270$ kPa. The CC tests are conducted by Harman (1976), as cited and electronically shared by Jefferies and Been (2016).

Figure 7.2b shows that for low and intermediate values of the initial void ratio there is a good match between the MPM results and CC test data at $\sigma'_{v0} = 60$ kPa. At higher values of e_0 there is a larger difference between the MPM model and CC tests. Very similar results are observed in Figure 7.2c when the stress level is increased to $\sigma'_{v0} = 270$ kPa, with matching Q values of the MPM model and CC tests at lower initial void ratios and a larger difference at higher ones.

7.4 Hokksund sand

7.4.1 NorSand parameters

In Table 7.3 the NorSand parameters of Hokksund sand are reported. In Figures E.5 and E.6 the results of the parameter determination for Hokksund sand are shown.

Table 7.3: NorSand parameters for Hokksund sand used in the validation phase.

Parameter [unit]	**Value**	**Parameter [unit]**	**Value**
G_{ref} [-]	496	ϕ_c [°]	25.4
ν [-]	0.2	N [-]	0.40
a [-]	0.5	H [-]	$138 + 513\psi_0 + 2250\psi_0^2$
e_Γ [-]	0.87	χ_{tc} [-]	4.0
λ_c [-]	0.031	$F_{e,fac}$ [-]	0
ξ [-]	0.53	$e_{el,min}$ [-]	0.20

7.4.2 Validation results

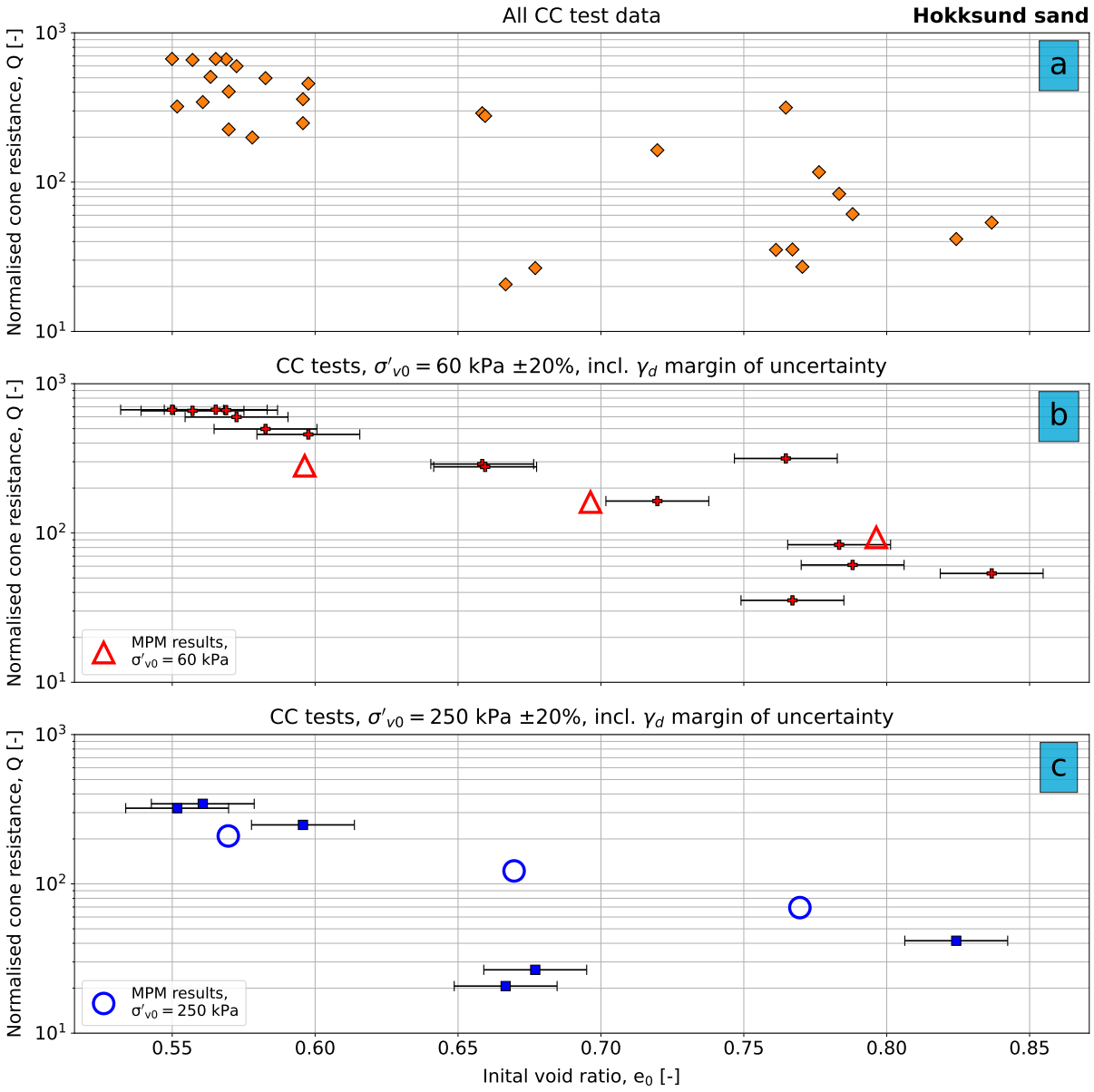

Figure 7.3: Results of the validation of Hoksund sand. CC test data from Baldi et al. (1986) and Lunne (1986), as cited in Jefferies and Been (2016). Electronically shared by Jefferies and Been (2016).

The CC tests of Hokksund sand are filtered for two stress levels: $\sigma'_{v0} = 60$ kPa and $\sigma'_{v0} = 250$ kPa. The CC tests are conducted by Baldi et al. (1986) and Lunne (1986) the latter source as cited by Jefferies and Been (2016).

Figure 7.3b shows that at a stress level of $\sigma'_{v0} = 60$ kPa there is a good agreement between MPM results and conducted CC tests, also at higher values of e_0. In Figure 7.3c it can be seen that at $\sigma'_{v0} = 250$ kPa, only six CC tests are available. The two CC tests in the range $0.65 \leq e_0 \leq 0.70$ are not consistent with the other four measurements. The difference with the MPM results at this initial void ratio is also large. It could be that these two CC tests are outliers for specific reasons. Unfortunately, this could not be checked at the time of writing this thesis, as the two tests are conducted by Lunne (1986) of which the original paper is not available.

The MPM results show a good agreement with the other four CC tests, with an approximately similar downward trend of Q with increasing e_0, although this could be biased given the limited number of CC tests available at this stress level.

7.5 GEBA sand

The validation for GEBA sand is different compared to the sands previously discussed. Instead of obtaining most NorSand parameters from literature as explained in Chapter 4, the NorSand parameters of GEBA sand are determined from laboratory tests conducted by Deltares and Fugro.

Four different CC tests are also conducted in the laboratory of Deltares. The results of these tests are used to validate the obtained model results. The specifications of the CC tests are shown in Table 7.4. The model domain is adjusted such that it resembles the actual CC test specifications.

Table 7.4: Specification of the conducted CC tests on GEBA sand.

Cone radius	23.5 mm
Chamber radius	448 mm
CCR	19
Lateral boundary condition	BC 1: constant lateral stress

7.5.1 NorSand parameters

In Table 7.5 the NorSand parameters of GEBA sand are reported. The NorSand plasticity parameters are determined from conducted drained triaxial tests. To determine the elasticity parameters, resonant column tests and bender element tests are performed. For the curved CSL parameters an oedometer test is conducted.

In Appendix E.4 the results of these tests are shown. It is also shown how from the conducted tests the NorSand parameters are determined.

Table 7.5: NorSand parameters for GEBA sand used in the validation phase.

Parameter [unit]	**Value**	**Parameter [unit]**	**Value**
G_{ref} [-]	385	ϕ_c [°]	31.8
ν [-]	0.2	N [-]	0.42
a [-]	0.5	H [-]	150
e_Γ [-]	0.953	χ_{tc} [-]	4.06
λ_c [-]	0.060	$F_{e,fac}$ [-]	0
ξ [-]	0.32	$e_{el,min}$ [-]	0.20

7.5.2 Validation results

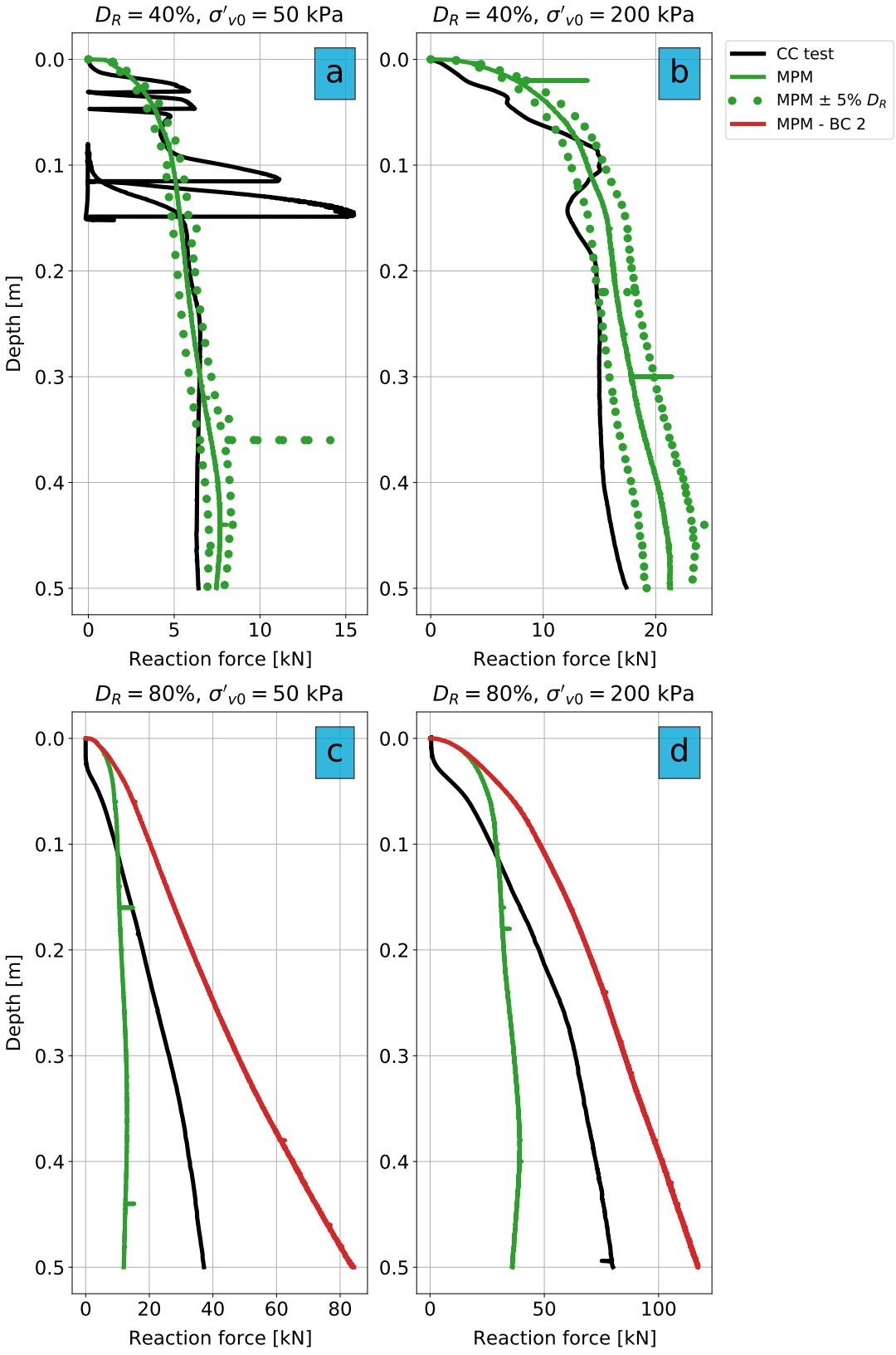

Figure 7.4: Results of the validation of GEBA sand.

Figure 7.4 shows the results of the GEBA validation. Four different CC tests are conducted at two initial densities for two initial vertical effective stress levels.

Figures 7.4a and 7.4b show the results for $D_R = 40\%$. For this density the 5% uncertainty in the determination of the relative density is considered and indicated with the dotted lines. A good agreement between the conducted CC tests and MPM model is visible for both $p' = 50$ kPa and $p' = 200$ kPa.

Figures 7.4c and 7.4d show the results for $D_R = 80\%$. It can be clearly seen that at this density there is a large difference between the CC tests and the MPM model. Considering the good agreement at $D_R = 40\%$, this begs the question of what is causing this. A hypothesis is that the boundary effects are cause of the deviations. The CC tests are conducted with CCR = 19, and from Chapter 6 is has become clear that at this CCR the boundary conditions affect the model results severely at denser soil states. To see if this is indeed the case, a second model calculation is performed at $D_R = 80\%$ but this time with the zero displacement lateral boundary condition (BC 2). The results show that the reaction force of the CC test falls in between the results of the MPM model with BC 1 and BC 2. With BC 1 and BC 2 representing the two extremes of the possible boundary conditions, this is reason to believe that the constant lateral stress boundary condition of the CC test is not properly maintained during the execution of the test. To confirm this, a visual inspection is performed at the calibration chamber and it is observed that if the horizontal displacement at the lateral boundary becomes larger than 2 mm the membrane makes contact with the steel of the chamber. If this occurs, it implies that the constant lateral stress BC cannot be optimally maintained and that the testing conditions between the CC test and the MPM model are different. This would mean that the CC test and the MPM model cannot be quantitatively compared to each other.

To assess if the horizontal displacement at the boundary is larger than 2 mm, a horizontal displacement vs. depth plot is made for the constant lateral stress BC scenarios of the MPM model. The results are shown in Figure 7.5. It can be clearly seen that at $D_R = 80\%$ for both $\sigma'_{v0} = 50$ kPa and $\sigma'_{v0} = 200$ kPa the horizontal displacement exceeds the 2 mm horizontal displacement limit by far. For $D_R = 40\%$ this limit is also breached, but far less significant and only around the depth of the cone. That the horizontal displacement is larger for $D_R = 80\%$ than for $D_R = 40\%$ is not surprising, as more dilation is expected when the soil is in a denser state resulting in a larger horizontal displacement.

Based on the magnitude by which the horizontal displacement limit is exceeded for sand at a density of $D_R = 80\%$, it is concluded that at $D_R = 80\%$ the constant lateral stress BC cannot be maintained during the CC test. Rather, a combination of initially BC 1 which continues into BC 2 when the horizontal displacement becomes too large is present. The obtained CC test results of Figure 7.4c and 7.4d fall in between the two extreme BCs, therefore confirming this statement. The excess of the 2 mm horizontal displacement for $D_R = 40\%$ is to a smaller extent, and BC 1 can be maintained better at this density. The results in Figure 7.4a and 7.4b confirm this by showing a good agreement between the CC test and the MPM model.

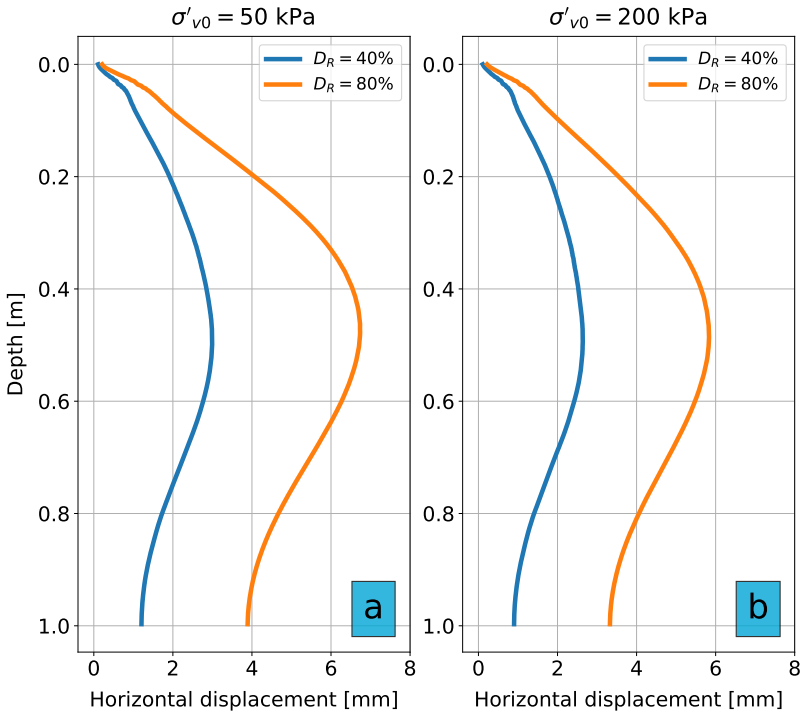

Figure 7.5: Horizontal displacement of GEBA sand obtained from the MPM model at the boundary for a constant lateral stress boundary condition.

7.6 Conclusion of the validation phase

The goal of the validation phase was to evaluate whether the cone resistance results of the MPM simulation are in agreement with experimental tests performed at real sands in the laboratory. Different sands with different soil properties were simulated at different initial stress levels and initial state parameters. The sands that were tested are Ticino 4 sand, Ottawa sand, Hokksund sand and GEBA sand.

For Ticino 4 sand, the MPM model provides normalised cone resistance results which are very similar to the CC test data for lower to intermediate values of e_0 at stress levels where $\sigma'_{v0} \leq 100$ kPa. At this stress level there is a larger difference between the MPM results and CC test data at higher values of e_0. The downward trend of Q with increasing e_0 is larger for the CC test data then for the MPM results. When the stress level is increased to $\sigma'_{v0} = 600$ kPa, a good agreement between the MPM model and CC test data is obtained for all considered initial densities. However, the downward trend of Q of the CC test data is slightly larger here as well.

The results of Ottawa sand are very similar to Ticino 4 sand. At lower and intermediate initial void ratios a good agreement between MPM results and CC test data exists, whereas at higher values of e_0 there is an overestimation of Q. This is also the case at a more intermediate stress level (compared to the considered stress levels of Ticino 4 sand) of $\sigma'_{v0} = 270$ kPa.

The MPM results of Hokksund sand showed a good agreement with the CC test data. However, it must be noted that the results at the stress level of $\sigma'_{v0} = 250$ could be biased due to the small number of CC tests available at this stress level.

For GEBA sand, a good agreement is obtained between the conducted CC tests and the MPM model at a density of $D_R = 40\%$. At $D_R = 80\%$ it has been shown that the constant lateral stress boundary condition cannot be properly maintained during the CC test. Therefore, the different boundary conditions during the CC test and the MPM model do not allow for an accurate comparison between the two. To further validate the GEBA sand at a higher density it is advised to redo the CC tests at $D_R = 80\%$, this time with the correct application of the boundary conditions.

Overall, it can be concluded that when NorSand parameters are properly determined and boundary conditions are properly applied, the MPM model produces results which resemble actual experimental results. Caution is advised when modelling loose sand, because in certain cases the MPM overestimates the normalised cone resistance. For the sands considered in this validation phase, that is mostly the case for soil states of $\psi_0 \geq -0.05$. The validation of GEBA sand is a promising sign for the validation of looser sand, as $D_R = 40\%$ is looser than the moderately-dense to dense soil state at which Ticino, Ottawa and Hokksund sand showed good agreements between the CC tests and MPM model. However, concluding that the MPM produces accurate results in loose sand solely based on the results of GEBA sand at $D_R = 40\%$ is premature, and further research is required to investigate the cause of the larger differences for looser sand.

8

NorSand Parameters Sensitivity Analysis

In this Chapter the results of the NorSand parameter sensitivity analysis are presented. The goal of this phase is to obtain insight in how NorSand parameters affect cone resistance results. It is also interesting to investigate the sensitivity of the parameters on q_c results, meaning: if a parameter is changed by a certain percentage, how large will the subsequent change in q_c be?

8.1 Approach

To investigate the sensitivity of NorSand soil and state parameters on q_c results a reference scenario is determined. This reference scenario does not reflect the NorSand parameters of a specific sand. Rather, approximate median values of NorSand parameters are used, based on the typical value range of NorSand parameters for sand as reported in Jefferies and Been (2016). Only the H parameter is relatively low compared to the typical value range. This is because the H values encountered for the sands in this thesis are generally at the lower side of this range. Using a lower H value is therefore deemed appropriate. A realistic value of the G_{ref} parameter is based on the parameter determination of the different sands in the validation phase of Chapter 7. The curved CSL parameters of Toyoura sand are adopted (see Figure 4.2).

A distinction is made between NorSand soil parameters and soil state parameters. The NorSand soil parameters represent the intrinsic soil properties of the sand. The soil state parameters represent the current state of the sand. In Table 8.1 an overview of the NorSand soil parameters of the reference scenario is presented. Table 8.3 shows an overview of all considered soil states.

The numerical settings (e.g. mesh type, mesh size) and boundary conditions (e.g. smooth or rough, constant lateral stress or zero displacement) are kept constant in all calculations, such that these are not a factor of changing q_c results. Quadrilateral elements with Mesh 00 are used in the analysis. A constant lateral stress boundary condition is adopted, with a domain size equalling CCR $= 50$.

Table 8.1: NorSand soil parameters of the reference scenario of the sensitivity analysis.

Parameter [unit]	Value	Parameter [unit]	Value
G_{ref} [-]	400	ϕ_c [°]	31.1
ν [-]	0.2	N [-]	0.35
a [-]	0.5	H [-]	100
e_Γ [-]	0.934	χ_{tc} [-]	3.5
λ_c [-]	0.019	$F_{e,fac}$ [-]	0
ξ [-]	0.70	$e_{el,min}$ [-]	0.20

Starting from the reference scenario, NorSand parameters are increased and decreased one by one. When a specific parameter is increased or decreased, all other parameters are kept at the original values of the reference scenario in Tables 8.1. This ensures that changes in model results can be completely attributed to the single change of that specific parameter. In Table 8.2 the increased and decreased values of the NorSand soil parameters are shown.

Table 8.2: Increased and decreased NorSand soil parameters in the sensitivity analysis.

Parameter [unit]	Reference value	Increased value	Decreased value	Abs. % change
G_{ref} [-]	400	500	300	25
ϕ_c [°]	31.1	33.4	28.8	7.4
N [-]	0.35	0.45	0.25	28.57
H [-]	100	130	70	30
χ_{tc} [-]	3.5	4.5	2.5	28.57

It is interesting to evaluate if the sensitivity of the NorSand soil parameter changes when changing the initial state of the soil. To investigate this, the sensitivity of NorSand soil parameters is assessed for three different initial soil states. The sensitivity of the soil state parameters itself is also determined. Four different initial soil states are determined for these analyses. An overview of these initial soil states is shown in Table 8.3.

Table 8.3: Overview of different soil states used in the NorSand sensitivity analysis.

Name	ψ_0 [-]	σ'_{v0} [kPa]
Soil state 1	−0.10	100
Soil state 2	−0.15	100
Soil state 3	−0.10	200
Soil state 4	−0.20	100

8.2 Results

8.2.1 Soil parameters

In Figure 8.1 the results of the NorSand soil parameter sensitivity analysis are shown. The q_c value of the reference scenario is the same for all parameters, also emphasised by the horizontal line drawn through the Figure. The respective icons indicate the obtained cone resistance with the parameter increase or decrease according to Table 8.2.

Figure 8.2 shows how the percentage change of each specific parameter relates to the percentage change in obtained q_c results, taking the reference scenario as reference point. The middle point in all graphs is always at $(0\%; 0\%)$, because a 0% value change of a parameter results in a 0% change in q_c. A linear line is fitted through the three points. The absolute value of the slope of this fitted line indicates how sensitive a parameter is to the cone resistance obtained with the model. The absolute value of the slope will be called the "Sensitivity Index" and is denoted with symbol S_I in Figure 8.2. The same percentile change of a parameter results in a larger difference in q_c for a higher S_I compared to a lower S_I. The larger S_I is for a parameter, the more sensitive that parameter thus is to q_c results.

For each soil parameter it is verified whether the differences in cone resistance for changing input parameters can be substantiated from the underlying theory of the NorSand model. The sensitivity of the parameter and differences in sensitivity for a different initial state are also commented on.

- G_{ref}: Increasing G_{ref} leads to an increase in q_c. This is what is to be expected when evaluating the stiffness equation used in the model (Eq. 4.1). At the same void ratio, increasing G_{ref} increases the shear modulus G. The stiffer soil mobilises more reaction forces under the cone, resulting in a higher q_c value. The S_I value is relatively low compared to other parameters. Increasing the relative density only results in a very small change in S_I Increasing the stress level has little effect on the S_I of G_{ref}. The G_{ref} parameter is therefore little influenced by the soil state.

- ϕ_c: Increasing ϕ_c leads to an increase in q_c. Increasing the critical state friction angle increases both the peak and critical shear strength of the soil. The higher shear strength results in a higher resistance experienced by the cone when pushed through, increasing q_c. ϕ_c is by far the most sensitive soil parameter, with a high S_I value and visible steep slope compared to the other parameters. Lowering ψ_0 has an almost negligible effect on S_I. Increasing σ'_{v0} results in a small decrease in sensitivity.

- N: Increasing N results in a decrease of q_c. Increasing N results in a larger portion of the work that is exerted on the soil to be transferred to the volumetric strain, rather than the distortional strain. This reduces the mobilisation of peak shear strength of the soil, resulting in less resistance experienced by the cone and a lower q_c. The decrease in peak shear strength due to N is limited, resulting in a low S_I value. Changes in soil state have a small, but noticeable effect on S_I.

- H: Increasing H leads to an increase in q_c. Increasing H results in faster hardening (see Eq. 2.47). The peak strength will be reached faster and the initial stiffness is increased, leading to higher q_c values. The S_I is moderately high compared to the other parameters. Decreasing H seems to have a larger effect than applying an increase. This could be the case due to the relatively low starting value of H. A small increase in S_I is observed when increasing the sand's initial state. Increasing the stress level in soil state 3 results in a decrease in sensitivity as the percentage change in initial stiffness becomes smaller as the stress level increases.

- χ_{tc}: An increase in χ_{tc} results in a higher q_c. Increasing χ_{tc} means that the maximum dilatancy is increased for a previously similar soil state (see Eq. 2.14). Therefore, a larger peak strength of the soil can be mobilised. Decreasing the state parameter has a significant effect on the S_I. This is what is to be expected, due to the direct coupling of χ_{tc} and ψ through Eq. 2.14 to define the maximum dilatancy of a sand. χ_{tc} directly amplifies or reduces soil strength mobilisation with a change in soil state, making the S_I susceptible to a change in ψ_0. When the stress level is increased, an increase or decrease in χ_{tc} still leads to a larger and smaller peak strength respectively. However, in terms of percentage this is smaller compared to lower stress levels, resulting in a lower sensitivity of χ_{tc} when increasing the stress level.

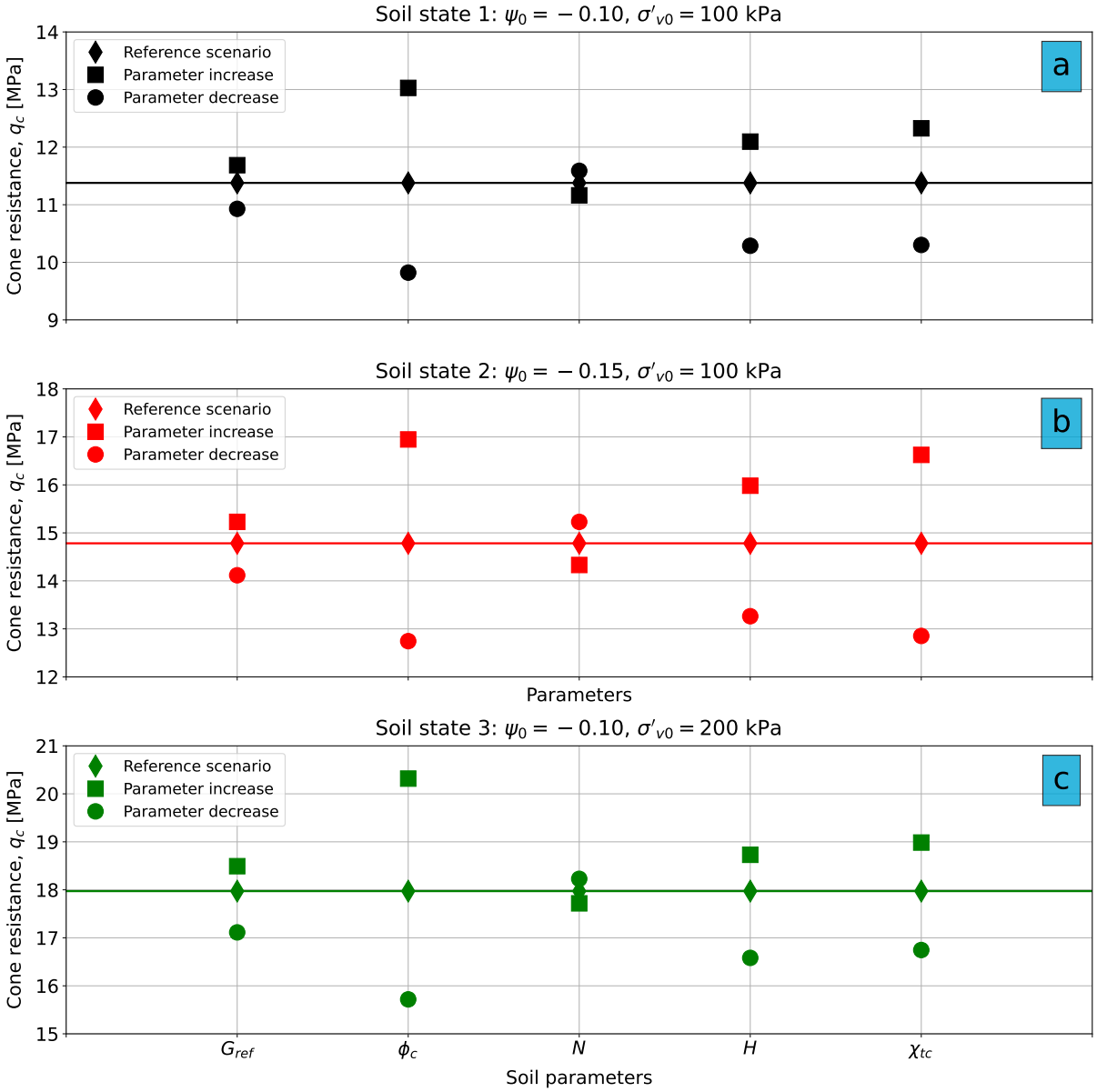

Figure 8.1: Obtained cone resistance values for the increased and decreased NorSand soil parameters.

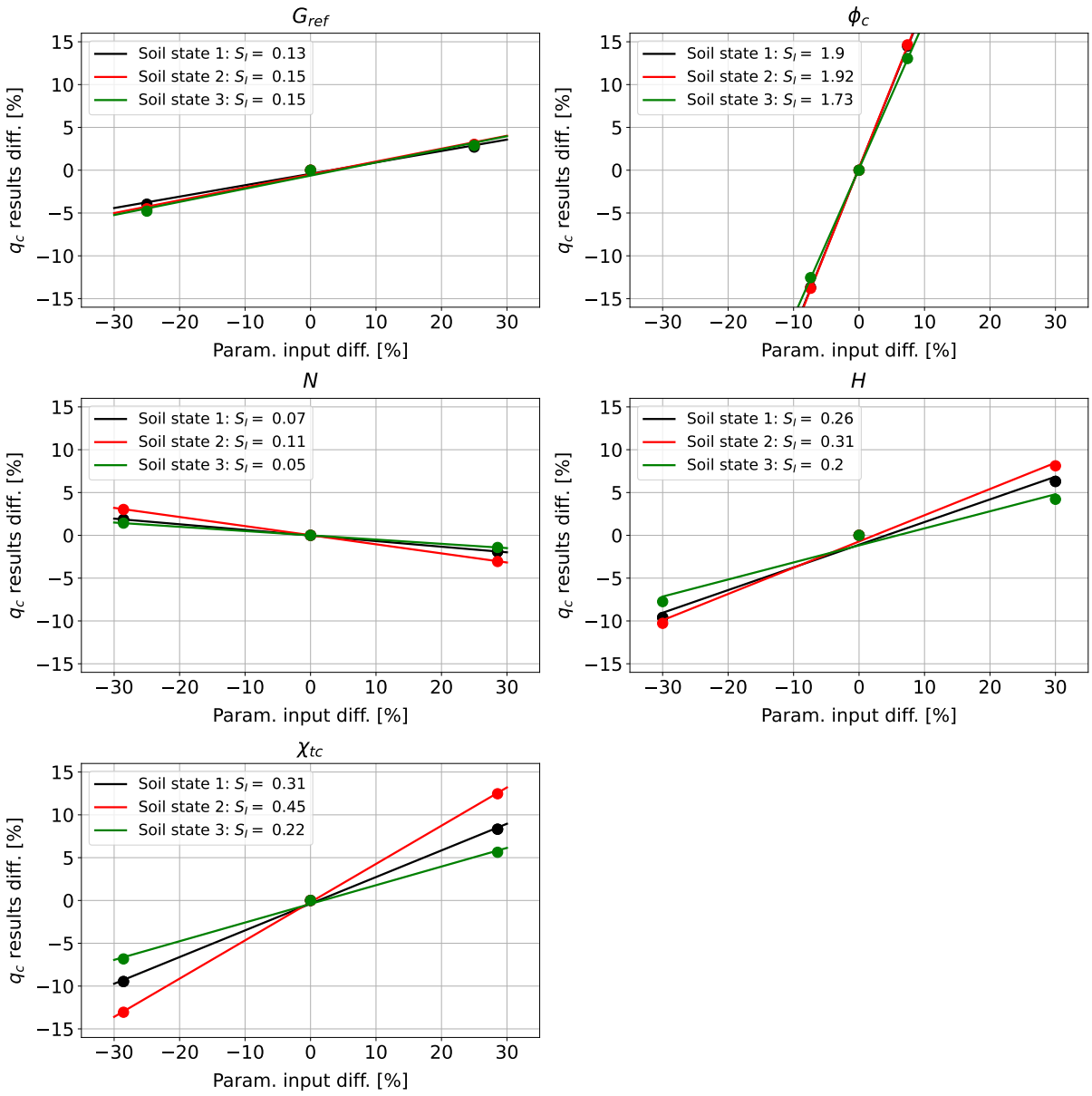

Figure 8.2: Sensitivity of NorSand soil parameters. Percentage difference of input parameters related to percentage difference in q_c.

8.2.2 Soil state parameters

Figure 8.3 shows the results of the soil state parameter sensitivity analysis for initial soil state 1. In Figure 8.4 the sensitivity of the NorSand state parameters is determined. It is also assessed how the sensitivity of a soil state parameter changes if the soil state is altered.

For the two soil state parameters it is briefly discussed whether the results are in accordance with expectations based on underlying theory.

- ψ_0: Increasing the initial state parameter leads to a decrease in q_c. This is what is to be expected because a higher state parameter means that the soil is in a looser state and subsequently less resistance is experience by the cone when pushed through, resulting in a lower q_c. For soil state 4 the initial state parameter is lowered compared to soil state 1, while the stress level is kept constant. This significantly increases the S_I value of ψ_0. This is not surprising, because a percentage change at a higher initial value results in a large absolute change of the parameter. It does however show that at lower values of ψ_0, relatively small changes in absolute terms still have a relatively large effect on q_c. When comparing the S_I to the NorSand soil parameters it becomes clear that the sensitivity of ψ_0 is higher in most cases (ϕ_c being the exception). This emphasises the importance of the sands density when modelling a CPT.
- σ'_{v0}: Increasing the stress level increases the cone resistance. The increase in stress level increases both the initial stiffness of the soil and the shear strength. Both these factors contribute to a higher resistance experienced by the cone when penetrated into the soil. Similarly to ψ_0, the S_I of σ'_{v0} is generally higher than that of most NorSand soil parameters. Increasing the vertical effective stress in soil state 3 and then performing the sensitivity analysis has a minimal effect on S_I.

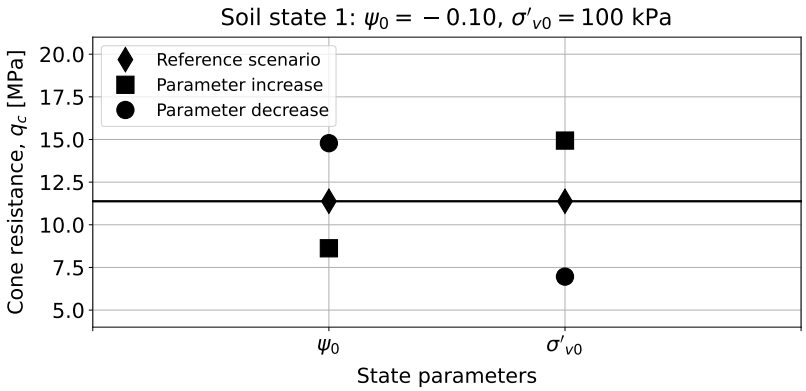

Figure 8.3: Obtained cone resistance values for the increased and decreased NorSand state parameters for soil state 1.

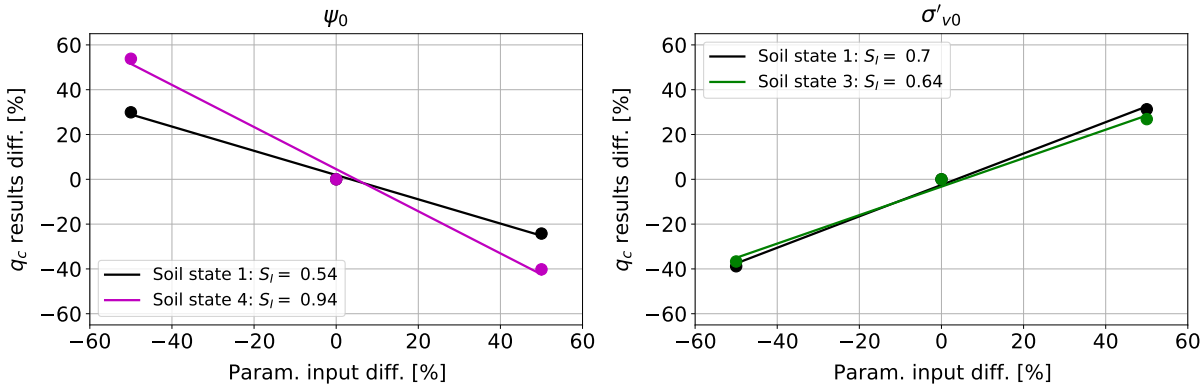

Figure 8.4: Sensitivity of soil state parameters. Percentage difference of input parameters related to percentage difference in q_c.

8.3 Conclusion of the NorSand parameters sensitivity analysis

The goal of the NorSand parameter sensitivity analysis was to obtain insight into how specific NorSand parameters influence cone resistance results and how sensitive the cone resistance obtained with the MPM model is to changes in these parameters. To evaluate this, NorSand parameters are increased and decreased and compared to a reference scenario. A clear distinction is made between NorSand soil and state parameter in the analyses.

For all NorSand soil and state parameters, the increase or decrease of the specific parameters led to a change in q_c that met expectations. For each parameter is has been substantiated from the theory behind NorSand why a certain change leads to a certain response.

The sensitivity of a parameter has been indicated by a so-called "Sensitivity Index" S_I, which is defined as the absolute value of the slope of a linear fitted line through a plot of the percentage change of q_c vs. the percentage change in input parameter. The higher the value of S_I, the more sensitive q_c is to a change of the parameter. It is important that parameters with a high S_I are accurately determined, as even a small change in these parameters due to potential inaccurate parameter determination will have a large effect on the obtained q_c results.

The most sensitive NorSand soil parameter is ϕ_c, with a substantial higher S_I compared to the other parameters. Changing the soil state generally has a small to negligible effect on the soil parameter sensitivity, except for χ_{tc}. This is in line with what is to be expected given the theory behind the χ_{tc} parameter.

The sensitivity of the sand state to the obtained q_c is generally higher than the sensitivity of the NorSand soil parameters. This emphasises the importance of the soil state within the NorSand constitutive framework for accurate CPT modelling.

Overall, the NorSand parameter sensitivity analysis confirms the correct functioning of all NorSand soil and state parameters within the constitutive framework for the modelling of a CPT.

9

Conclusions

The objective of this thesis is to investigate whether the MPM using NorSand as the soil's constitutive model is able to produce reliable CPT results in dry sand that are reliable and which correspond quantitatively to reality.

This objective has led to the main research question of this thesis to be formulated as follows:

"Is the MPM using NorSand as its constitutive model suitable as a reliable quantitative modelling tool for a CPT in dry sand?"

Four research phases are conducted to answer the main research question. The main conclusions drawn from the results are listed below.

- The numerical verification phase shows that changing the mesh size adjacent to the shaft of the cone results in inconsistencies in the obtained sleeve friction values. A further investigation into the cause of this reveals that the inconsistencies are related to the current implementation of the constitutive model. This leads to the conclusion that, although sleeve friction results are in an order of magnitude which would be expected based empirical relations, the current implementation of NorSand is unable to reliably quantify the sleeve friction.
- The use of quadrilateral elements instead of triangular elements results in quantitative differences in cone resistance due to the different anti-volumetric locking techniques used in the elements. During this study a localisation of volumetric strains due to compaction resulting from the prescribed movement of the cone has been identified. Using quadrilateral elements with the B-Bar method as anti-volumetric locking technique proved to be the most suitable for the analysis. This setup avoids sharing volumetric strains with adjacent elements, as would be the case when applying triangular elements with the strain smoothing procedure.
- The boundary condition analysis shows that the model reacts similarly to different boundary conditions as real CC tests. The results that have been obtained are in agreement with conclusions drawn in previous studies on CC tests. The analysis provides insight in how to set up the domain and boundary conditions in future analyses. The state of the sand is an important factor in setting up the domain. For most situations a value of CCR $= 50$ will suffice to mitigate most of the lateral boundary effects. When a very dense sand is modelled at a low stress level, the CCR may have to be increased due to the larger zone of influence. Similarly, a smaller domain size can be used when modelling loose sand.

- In the validation phase the MPM shows that a good agreement is found between the cone resistance of the MPM model and the CC tests for initial soil states which can be characterised as medium-dense to dense ($\psi_0 \leq -0.10$). This has been validated for three different sands of which CC test data and NorSand parameters are obtained from literature, at different effective stress levels ranging from relatively low ($\sigma'_{v0} = 60$ kPa) to relatively high ($\sigma'_{v0} = 600$ kPa).

- The validation of GEBA sand shows that a good agreement is found between the conducted CC tests and the MPM model at a relative density of $D_R = 40\%$. However, the incorrect application of the lateral constant stress boundary condition at $D_R = 80\%$ prevents the validation of GEBA sand at a higher relative density.

- The downward trend of the normalised cone resistance with increasing ψ_0 is generally greater for the CC tests compared to the MPM results. This means that for looser sand, generally at $\psi_0 \geq -0.05$, a difference between the MPM results and CC test data is observed in certain cases. When modelling sand at this state, caution is needed when interpreting MPM results, as it is possible that the results are an overestimation of reality. The root of any possible overestimation at this density has not been identified as of yet.

- The NorSand parameter sensitivity analysis confirms the correct functioning of the NorSand parameters within the constitutive model. Changes in input values of the parameters lead to changes in cone resistance which are in accordance with expectations based on underlying NorSand theory. Insight is provided into the sensitivity of NorSand parameters to cone resistance results. Changing the initial state of the sand generally results in minor changes in the sensitivity of NorSand soil parameters, with the χ_{tc} parameter as exception. The sensitivity of the sand's state to the cone resistance is generally higher than the sensitivity of the NorSand soil parameters, emphasising the importance of the soil state within the NorSand constitutive framework.

- The obtained results of the four research phases illustrate the improvement of modelling a CPT in dry sand using the MPM compared to the previous studies with the Mohr-Coulomb model by Schuringa (2020) and Hardening Soil model by Martinelli and Galavi (2021). Compared to the other constitutive models, the advanced description of dilatancy in NorSand is regarded an important feature. Using a proper numerical setup and parameter determination process, the MPM using NorSand is able to accurately calculate the cone resistance at moderately-dense to dense soil states for a variety of different sands and stress states. Furthermore, the NorSand parameter sensitivity analysis shows that the response in cone resistance to changing input parameters is in agreement with what would be expected from theoretical understanding of the constitutive model. This implies that when NorSand parameters are properly determined for new sands, the MPM model will be able to produce accurate values of the cone resistance at moderately-dense to dense soil states.

  However, in answering the main research question the answer can only be partially confirmed. In certain instances, sands in loose states still show a difference between model results and experimental data. Furthermore, the inconsistency in sleeve friction results due to mesh size changes adjacent to the shaft is also a factor preventing a definitive positive answer to the main research question.

10 Recommendations

Certain results of the conducted research in this thesis form grounds for further research regarding this research topic. In this Chapter the most important recommendations for further research will be discussed.

- The inconsistencies in sleeve friction results due to numerical factors currently prevent the complete modelling of the installation of a CPT, because only cone resistance results can be reliably obtained. This thesis investigates the cause of these inconsistencies in sleeve friction results and identifies the constitutive model as a possible source. A further investigation into how NorSand behaves in rapid unloading conditions, such as around the shoulder of the cone, is advised to confirm whether this is indeed the cause of the problems and to potentially solve it. This helps to ensure that the sleeve friction can ultimately be reliably determined, enabling a complete CPT to be modelled by the MPM.

- The localisation of volumetric strains under the cone due to compaction is maintained in the calculations when using quadrilateral elements with the B-Bar method. This type of localisation is a relative novelty in the MPM, as most localisation issues are due to shear. A further investigation into localisation behaviour due to compression and methods to solve it is advised to see if mitigation of the localisation without having to share volumetric strains with adjacent elements results in an improvement of model results.

- Currently, the cone resistance results of the validation phase only allow for a consistent good agreement between MPM results and CC tests for soil states for which it approximately holds that $\psi_0 \leq -0.10$. Ideally, however, the entire range of relative densities of sand could be accurately modelled, including sand in looser states. A further investigation into the differences is recommended to be able to confidently interpret CPT results of the MPM model of sand in any state in the future. A starting point could be to investigate the relation between the hardening modulus parameter H and ψ_0. H is often a function of ψ_0 and decreases with increasing ψ_0. The NorSand parameter sensitivity analysis has shown that changing H has a noticeable effect on q_c. A larger decrease in H when the soil state become more loose is therefore likely to have a noticeable effect and could improve the agreement between MPM results and CC tests at looser soil states.

- A topic which has remained relatively untouched in this thesis is the particle crushing of sand at the cone tip. Due to the high stresses directly under the cone, the crushing of sand particles during a CPT is no new phenomenon. In this thesis the crushing of particles is taken into consideration by applying the curvature in the CSL at high confining stresses. The requirement of this curved CSL is that it falls within a region close the the $K_0 - LCC$, and the $K_0 - LCC$ is mainly governed by particle crushing. This is one method of incorporating particle crushing effects, but other methods are also available. Recent studies have shown promising results of incorporating particle crushing effects in critical state based constitutive models for granular soils, mainly focusing on how the CSL is altered due to particle crushing (Chang & Deng, 2020; Tong et al., 2021). Due to the importance of incorporating particle crushing during the modelling of a CPT, it is interesting to investigate whether the implementation of NorSand can be extended by including particle crushing effects in the constitutive equations to see if doing so results in improved MPM results compared to the current approach.

- Considering that this thesis is conducted in the scope of the DCPM project, it is relevant to discuss the further course of research regarding the development of the DCPM.

  In this thesis most emphasis is placed upon the obtained cone resistance and shaft friction results of the model. The range of sand densities for which the model produces robust results provide a natural starting point for further assessment of the disturbance behind the cone at the position of the inflatable membrane as a result of cone penetration. During this thesis the disturbance caused by cone penetration has been occasionally assessed, but a lot of room remains for a more in-depth investigation of this effect.

  The second recommendation in this scope is to extend the model to the modelling of two-phase materials, meaning the modelling of a saturated sand. The dry sand conditions in this thesis are convenient for the validation to CC tests, but for the intended application of the DCPM in near- and offshore environments this is unrealistic as the soil conditions are predominantly saturated. Modelling the installation of a CPT in saturated sand with NorSand and the assessment of e.g. excess pore pressure development around the cone is a possible next step to further validate the model to new materials.

Bibliography

Ahmadi, M. M., & Robertson, P. K. (2008). A numerical study of chamber size and boundary effects on CPT tip resistance in NC sand. *Scientia Iranica*, *15*(5), 541–553.

Al-Kafaji, I. K. J. (2013). *Formulation of a Dynamic Material Point Method (MPM) for Geomechanical Problems* (Doctoral dissertation). University of Stuttgard.

Arroyo, M., Butlanska, J., Gens, A., Calvetti, F., & Jamiolkowski, M. (2011). Cone penetration tests in a virtual calibration chamber. *Geotechnique*, *61*(6), 525–531. https://doi.org/10.1680/geot.9.P.067

Baldi, G., Bellotti, R., Ghionna, V., Jamiolkowski, M., & Pasqualini, E. (1986). Interpretation of CPTs and CPTUs, Part □: Drained Penetration in Sands. *Proc. of 4th International Geotechnical Seminar on Field Instrumentation and In Situ Measurements*.

Been, K., Jefferies, M. G., Crooks, J. H., & Rothenburg, L. (1987). The cone penetration test in sands: Part II, general inference of state. *Geotechnique*, *37*(3), 285–299. https://doi.org/10.1680/geot.1987.37.3.285

Been, K., Crooks, J. H., Becker, D. E., & Jefferies, M. G. (1986). The cone penetration test in sands: Part I, state parameter interpretation. *Geotechnique*, *36*(2), 239–249. https://doi.org/10.1680/geot.1986.36.2.239

Been, K., & Jefferies, M. G. (1985). A state parameter for sands. *Geotechnique*, *35*(2), 99–112. https://doi.org/10.1680/geot.1986.36.1.123

Brackbill, J. U., & Ruppel, H. M. (1986). FLIP: A method for adaptively zoned, particle-in-cell calculations of fluid flows in two dimensions. *Journal of Computational Physics*, *65*(2), 314–343.

Brinkgreve, R. J. B. (2019). Behaviour of Soils and Rocks: Lecture Slides. Delft University of Technology (personal communication).

Carter, J. P., Desai, C. S., Potts, D. M., Schweiger, H. F., & Sloan, S. W. (2000). Computing and computer modelling in geotechnical engineering. *ISRM International Symposium 2000, IS 2000*.

Casagrande, A. (1936). Characteristics of cohesionless soils affecting the stability of slopes and earth fills. *J. Boston Society of Civil Engineers*, *23*(1), 13–32.

Ceccato, F., Chmelnizkij, A., Di Carluccio, G., Fern, J., Marveggio, P., Pinyol, N., Rohe, A., Stapelfeldt, M., & Yerro, A. (2019). *MPM Software – Anura3D, Scientific Manual* (tech. rep.). Anura3D MPM Research Community.

Chang, C. S., & Deng, Y. (2020). Modeling for critical state line of granular soil with evolution of grain size distribution due to particle breakage. *Geoscience Frontiers*, *11*(2), 473–486. https://doi.org/10.1016/j.gsf.2019.06.008

Chavez Abril, M. A. (2017). Numerical simulations of static liquefaction in submerged slopes [Master's thesis, Delft University of Technology].

Courant, R., Friedrichs, K., & Lewy, H. (1967). On the partial difference equations of mathematical physics. *IBM journal of Research and Development*, *11*(2), 215–234.

Donea, J., Huerta, A., Ponthot, J., & Rodrígues-Ferran, A. (2004). Arbitrary Lagrangian–Eulerian Methods. *Encyclopedia of computational mechanics*.

Drucker, D. C., Gibson, R. E., & Henkel, D. J. (1957). Soil Mechanics and Work-Hardening Theories of Plasticity. *Transactions of the American Society of Civil Engineers*, *122*(1), 338–346. https://doi.org/10.1061/taceat.0007430

Evans, M. W., & Harlow, F. H. (1957). *The particle-in-cell method for hydrodynamic calculations* (tech. rep.). LOS ALAMOS NATIONAL LAB NM.

Fallah, S., Gavin, K., & Jalilvand, S. (2016). Numerical modelling of Cone Penetration Test in Clay using Coupled Eulerian Lagrangian Method. *Proceedings of Civil Engineering Research*.

Galavi, V., Tehrani, F. S., Martinelli, M., Elkadi, A., & Luger, D. (2019). Axisymmetric Formulation. In J. Fern, A. Rohe, K. Soga, & E. Alonso (Eds.), *The material point method for geotechnical engineering: A practical guide* (pp. 89–100). CRC Press.

Ghafghazi, M., & Shuttle, D. (2008). Interpretation of sand state from cone penetration resistance. *Géotechnique*, *58*(8), 623–634. https://doi.org/10.1680/geot.2008.58.8.623

Harlow, F. H. (2004). Fluid dynamics in group T-3 Los Alamos National Laboratory (LA-UR-03-3852). *Journal of Computational Physics*, *195*(2), 414–433. https://doi.org/10.1016/j.jcp.2003.09.031

Harman, D. (1976). A statistical study of static cone bearing capacity, vertical effective stress, and relative density of dry and saturated fine sands in a large triaxial testing chamber [Master's Thesis, University of Florida].

Houlsby, G. T., & Withers, N. J. (1988). Analysis of the cone pressuremeter test in clay. *Geotechnique*, *38*(4), 575–587. https://doi.org/10.1680/geot.1988.38.4.575

Hughes, T. J. (2000). Strain Projection: The B-approach. *The finite element method: Linear static and dynamic finite element analysis*. Courier Corporation.

Ishihara, K., Tatsuoka, F., & Yasuda, S. (1975). Undrained Deformation and Liquefaction of Sand Under Cyclic Stresses. *Soils and Foundations*, *15*(1), 29–44. https://doi.org/10.3208/sandf1972.15.29

Jefferies, M. G. (1993). Nor-Sand: A simple critical state model for sand. *Geotechnique*, *43*(1), 91–103. https://doi.org/10.1680/geot.1993.43.1.91

Jefferies, M. G. (1997). Plastic work and isotropic softening in unloading. *47*(5), 1037–1042.

Jefferies, M. G., & Been, K. (2016). *Soil liquefaction: a critical state approach* (Second Ed.). CRC Press.

Jefferies, M. G., & Shuttle, D. A. (2002). Dilatancy in general Cambridge-type models. *Geotechnique*, *52*(9), 625–638. https://doi.org/10.1680/geot.2002.52.9.625

Jefferies, M. G., & Shuttle, D. A. (2011). On the operating critical friction ratio in general stress states. *Geotechnique*, *61*(8), 709–713. https://doi.org/10.1680/geot.9.T.032

Kulak, R. F., & Bojanowski, C. (2011). Modeling of Cone Penetration Test Using SPH and MM-ALE Approaches. *8th European LS-DYNA Users Conference*, (May 2011), 1–10.

Lunne, T. (1986). Results obtained at Southampton and some preliminary interpretation (Personal Communication by Jefferies, M. G., & Been, K. (2016)).

Martinelli, M., & Galavi, V. (2021). Investigation of the Material Point Method in the simulation of Cone Penetration Tests in dry sand. *Computers and Geotechnics*, *130*, 103923. https://doi.org/10.1016/j.compgeo.2020.103923

Nelder, J. A., & Mead, R. (1965). A Simplex Method for Function Minimization. *The Computer Journal*, *7*(4), 308–313. https://doi.org/10.1093/comjnl/7.4.308

NEN-EN-ISO22476-1. (2012). *Geotechnical investigation and testing - Field testing - Part 1: Electrical cone and piezocone penetration test (ISO 22476-1:2012,IDT)* (Standard). Nederlands Normalisatie-instituut. Delft.

Niemunis, A. (2007). Incremental Driver: Single Element Program. https://soilmodels.com/idriver/

Nishiguchi, A., & Yabe, T. (1983). Second-order fluid particle scheme. *Journal of Computational Physics*, *52*(2), 390–413. https://doi.org/10.1016/0021-9991(83)90037-2

Oh, K.-Y., Nam, W., Ryu, M. S., Kim, J. Y., & Epureanu, B. I. (2018). A review of foundations of offshore wind energy convertors: Current status and future perspectives. *Renewable and Sustainable Energy Reviews*, *88*, 16–36. https://doi.org/10.1016/j.rser.2018.02.005

Parkin, A., & Lunne, T. (1982). Boundary effects in the laboratory calibration of a cone penetrometer for sand. *Norwegian Geotechnical institute publication*, *138*.

Pestana, J. M., & Whittle, A. J. (1995). Compression model for cohesionless soils. *Geotechnique*, *45*(1), 611–631.

Phoon, K.-K., & Kulhawy, F. H. (1999). Characterization of geotechnical variability. *Canadian geotechnical journal*, *36*(4), 612–624.

Reynolds, O. (1885). LVII. On the dilatancy of media composed of rigid particles in contact. With experimental illustrations. *The London, Edinburgh, and Dublin Philosophical Magazine and Journal of Science*, *20*(127), 469–481. https://doi.org/10.1080/14786448508627791

Robertson, P. K. (2010). Soil behaviour type from the CPT: an update. *2nd International Symposium on Cone Penetration Testing*, (2), 575–583.

Robertson, P. K. (2017). Evaluation of flow liquefaction: influence of high stresses. *Proceedings of the 3rd International Conference on Performance Based Design (PBD-III), Vancouver: ISSMGE*.

Roscoe, K. H., Schofield, A. N., & Wroth, C. P. (1958). On the yielding of soils. *Geotechnique*, *8*(1), 22–53. https://doi.org/10.1680/geot.1958.8.1.22

Rowe, A. P. W. (1962). The stress-dilatancy relation for static equilibrium of an assembly of particles in contact. *Proceedings of the Royal Society of London. Series A. Mathematical and Physical Sciences*, *269*(1339), 500–527. https://doi.org/10.1098/rspa.1962.0193

Schanz, T., Vermeer, P. A., & Bonnier, P. G. (1999). The hardening soil model: Formulation and verification. *Proceedings of the international symposium Beyond 2000 in computational geotechnics*, 281–296. https://doi.org/10.1201/9781315138206-27

Schofield, A. N., & Wroth, P. (1968). *Critical state soil mechanics* (Vol. 310). McGraw-hill London.

Schuringa, J. W. T. A. (2020). Modelling the Installation of a Cone [Master's thesis, Delft University of Technology]. https://repository.tudelft.nl/islandora/object/uuid%3A1db732e7-fde1-4a2f-9912-46cdb4cd2c52

Skempton, A. W., & Bishop, A. W. (1950). Measurement of shear strength of soils. Discussion by A. W. Bishop. *Geotechnique*, *2*(2), 113.

Sulsky, D., Chen, Z., & Schreyer, H. L. (1994). A particle method for history-dependent materials. *Computer Methods in Applied Mechanics and Engineering*, *118*(1-2), 179–196. https://doi.org/10.1016/0045-7825(94)90112-0

Sulsky, D., & Schreyer, H. L. (1996). Axisymmetric form of the material point method with applications to upsetting and Taylor impact problems. *Computer Methods in Applied Mechanics and Engineering*, *139*(1-4), 409–429. https://doi.org/10.1016/S0045-7825(96)01091-2

Tong, C. X., Zhai, M. Y., Li, H. C., Zhang, S., & Sheng, D. (2021). Particle breakage of granular soils: changing critical state line and constitutive modelling. *Acta Geotechnica*, 1–14. https://doi.org/10.1007/s11440-021-01231-8

Van den Berg, P. (1994). *Analysis of soil penetration* (Doctoral dissertation). Delft University of Technology.

Verdugo, R. (1992). The critical state of sands: Discussion. *Geotechnique*, *42*(4), 655–663. https://doi.org/10.1680/geot.1992.42.4.655

Withers, N. J., Howie, J., Hughes, J. M., & Robertson, P. K. (1989). Performance and analysis of cone pressuremeter tests in sands. *Geotechnique*, *39*(3), 433–454. https://doi.org/10.1680/geot.1989.39.3.433

Withers, N. J., Schaap, L. H., & Dalton, C. P. (1986). The development of a full displacement pressuremeter. *The Pressuremeter and Its Marine Applications: Second International Symposium*.

Yang, J., & Liu, X. (2016). Shear wave velocity and stiffness of sand: The role of non-plastic fines. *Geotechnique*, *66*(6), 500–514. https://doi.org/10.1680/jgeot.16.D.006

Zhang, X., Chen, Z., & Liu, Y. (2016). *The material point method: a continuum-based particle method for extreme loading cases*. Academic Press.

A

Surfaces Defined in the Domain

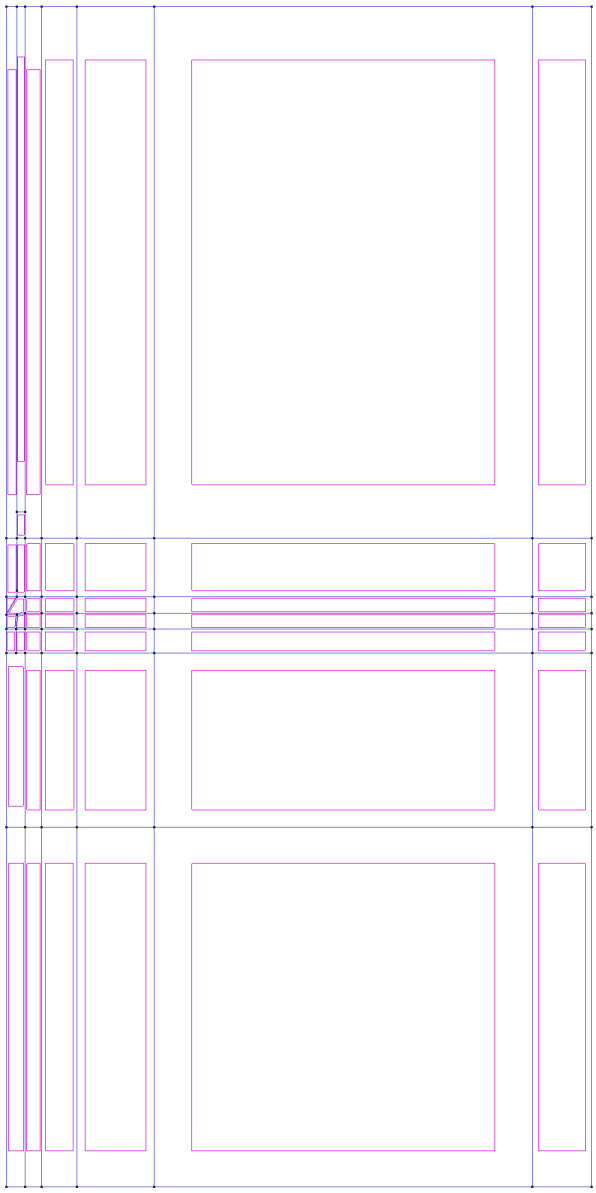

Figure A.1: Example model domain with drawn geometry and defined surfaces.

B

Compression Model and Oedometer Simulation Fit Quality Quantification

As described in Chapter 4 it is desired to be able to quantify the quality of the oedometer simulation compared to the compression model of Pestana and Whittle (1995). This way the determination of the curved CSL parameters is not solely based on 'visual inspection' of the two results.

Standard practice is to calculate the coefficient of determination R^2. This has been conducted for the determination of the elasticity parameters (see e.g. Figure 4.1). However, this method cannot directly be used to determine an R^2 value for the results of the oedometer simulation and the compression model. The problem is that for the calculation of R^2 a function must be fitted through a dataset. In this situation there is not a single function describing either of the two results. Both the compression model and the oedometer simulation are solved incrementally and results are returned and subsequently plotted in terms of arrays. However, with the help of an assumption it is possible to quantify the quality of the parameter optimisation.

Consider Figure B.1. The assumption that has been made is that between two datapoints of the compression model linear interpolation can be applied to obtain the void ratio of points which lie in between these two datapoints. Subsequently, from this linear interpolation the residuals can be determined as normal, also indicated in Figure B.1. The sum of the squares of the residuals determined using this method will be denoted as SS^*_{res} in this thesis. This version of the coefficient of determination will be denoted as R^2_* in this thesis and is calculated similarly as the conventional R^2, as is shown in Eq. B.1.

$$R^2_* = 1 - \frac{SS^*_{res}}{SS_{tot}} \tag{B.1}$$

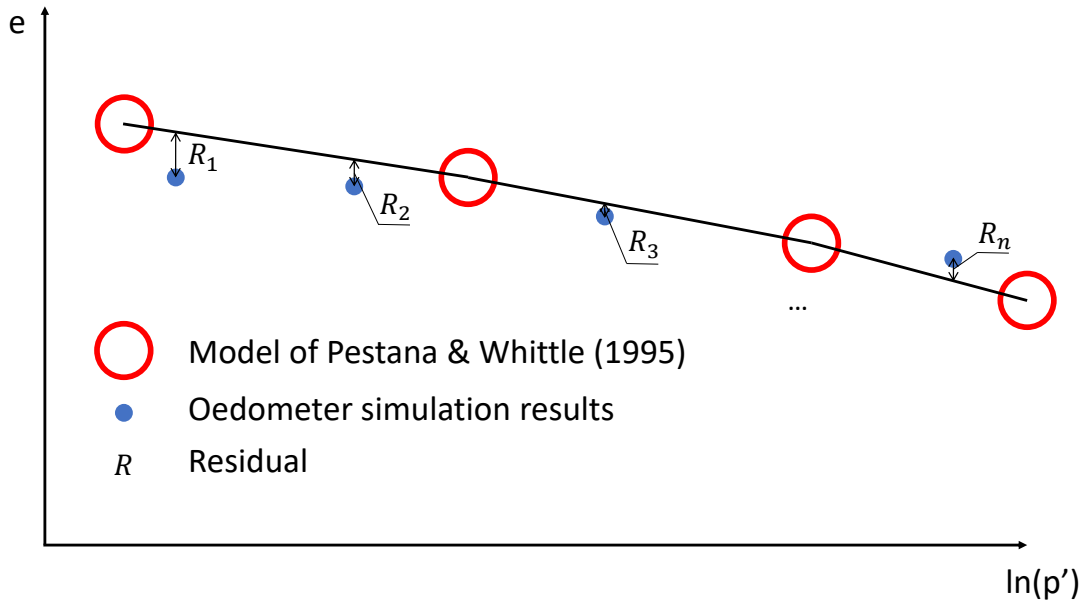

Figure B.1: Sketch of the linear interpolation between two points of the compression model of Pestana and Whittle (1995) and how subsequently the residuals are determined.

B.1 Remark about typical R^2_* values

The R^2_* values of the oedometer simulation fit are generally not that high when compared with e.g. the R^2 values obtained in the elasticity parameter optimisation. The reason for this is that the compression path of the model of Pestana and Whittle (1995) decreases more gradually than the oedometer simulation. This results in a relatively large difference between the two results in the 'transition zone' towards the LCC regime, shown in the red circled area of Figure B.2. The parameter mainly controlling this transition in the oedometer simulation is the exponent in the stiffness relation a, from Eq. 4.1. When a is decreased a smoother transition towards the LCC regime is observed in Figure B.2. As a result the R^2_* is higher compared to higher values of a.

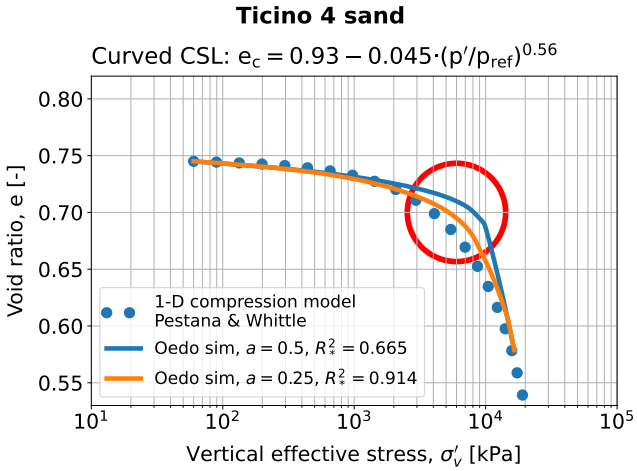

Figure B.2: Comparison between different values of a on the transition zone of the oedometer simulation.

The reason a lower value of a is not considered is because it results in an inaccurate representation of the stiffness reported in literature. Figure B.3 shows the results of the optimisation of G_{ref} when a value of $a = 0.25$ is used instead of the default $a = 0.5$. Clearly the elasticity implementation used in this thesis has a worse fit to the relation reported in literature (compared to e.g. Figure 4.1). Attempts have been made to see if an accurate fit was possible by also optimising a and $e_{el,min}$ alongside G_{ref}, but results unfortunately did not improve.

It is therefore decided to adopt the default value of $a = 0.5$ to continue to describe the stiffness accurately. As a consequence the R^2_* value will be lower. Instead of purely trying to decrease the R^2_* value the aim should be to obtain an accurate fit before and after the transition zone, which is also achieved with $a = 0.5$. The R^2_* can be used to fine-tune the details of the curved CSL parameters.

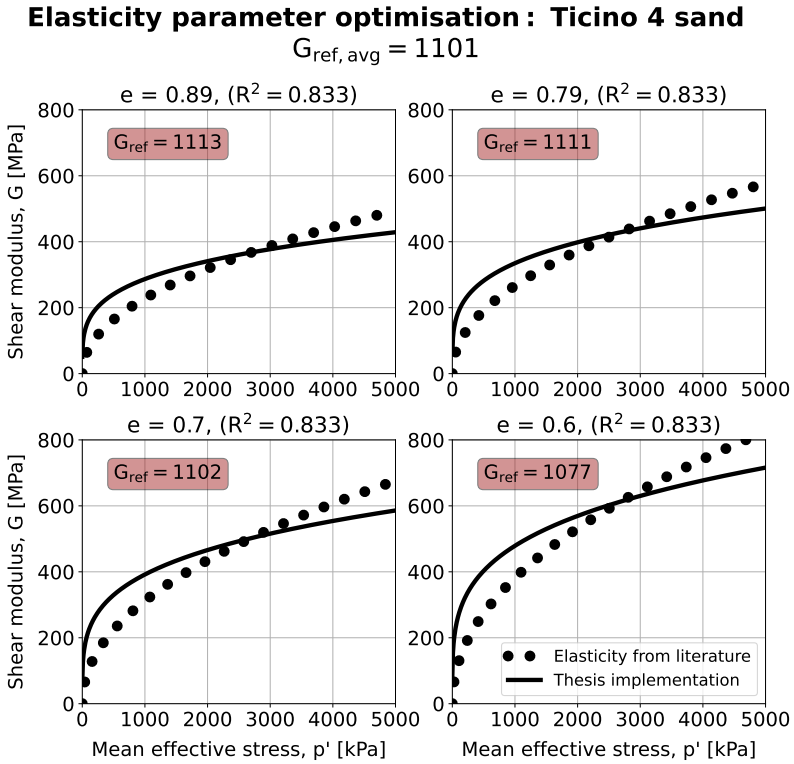

Figure B.3: Results of the elasticity parameter optimisation when a value of $a = 0.25$ is used.

C

Additional Figures and Results for the Numerical Verification

In this Appendix the results of the numerical verification phase which are not reported in Chapter 5 due to reasons of conciseness are shown.

C.1 Additional figures mesh size analysis triangular elements

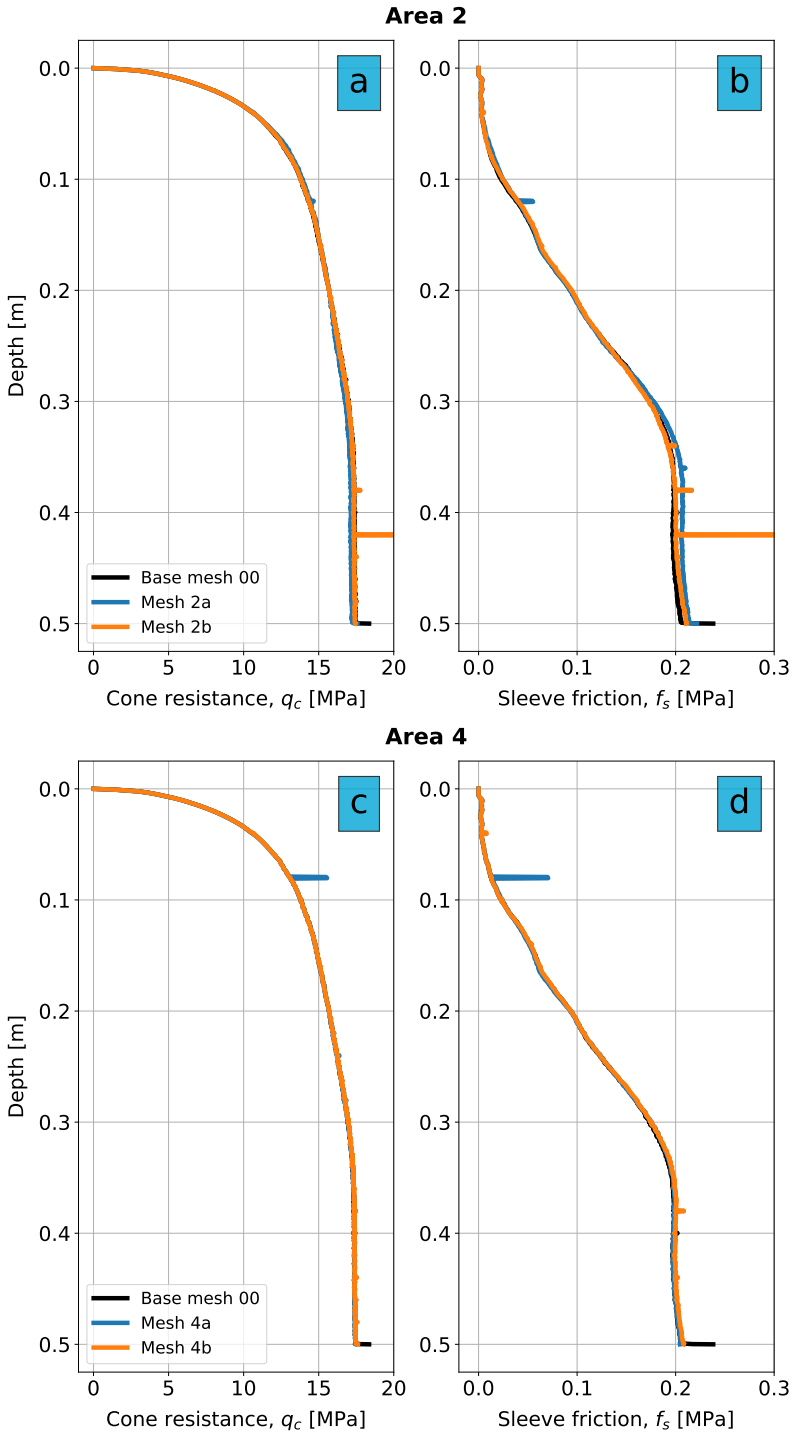

Figure C.1: Depth vs. cone resistance and sleeve friction results of the mesh size analysis for Area 2 and 4. Constitutive model used: NorSand.

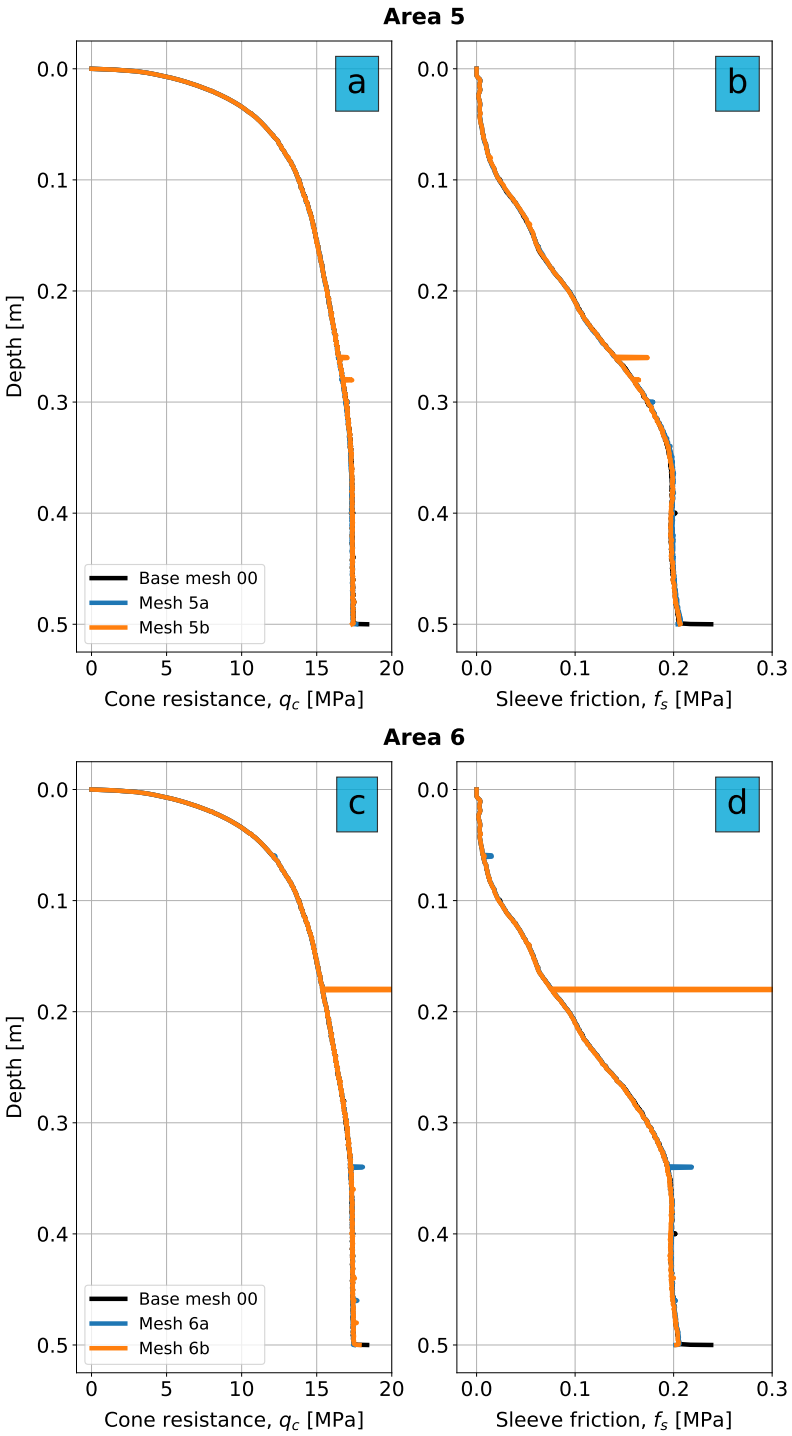

Figure C.2: Depth vs. cone resistance and sleeve friction results of the mesh size analysis for Area 5 and 6. Constitutive model used: NorSand.

C.2 Additional figures mesh size analysis quadrilateral elements

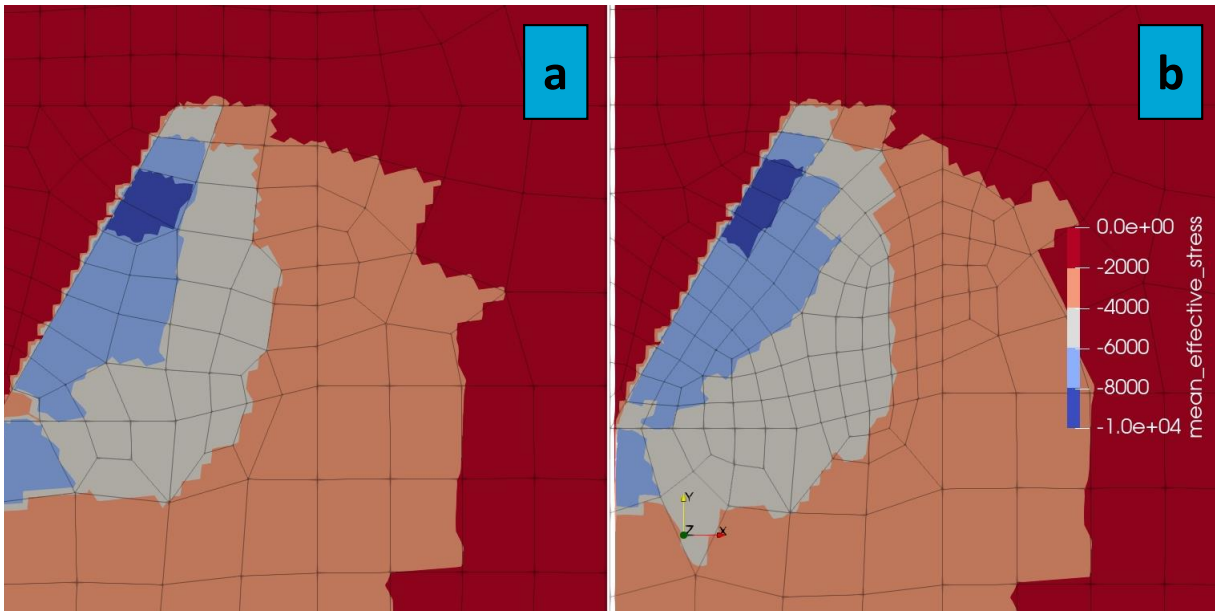

Figure C.3: Effect of mesh refinement on the localisation using quadrilateral elements. (a) Mesh 00, (b) Mesh 1a. Constitutive model used: NorSand.

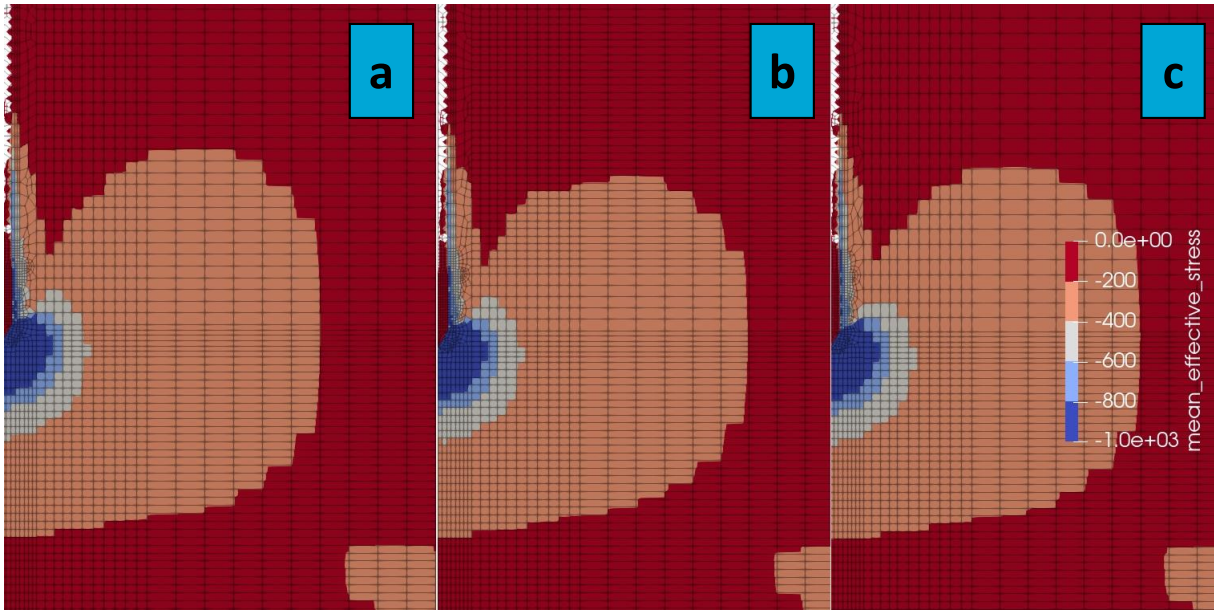

Figure C.4: Contour plot of the mean effective stress using quadrilateral elements for (a) Mesh 00, (b) Mesh 5a, (c) Mesh 5b. Constitutive model used: NorSand.

D

Additional Figures and Results for the Boundary Condition Analysis

In this Appendix the results of the boundary condition analysis phase which are not reported in Chapter 6 due to reasons of conciseness are shown.

D.1 Relevant boundaries in the domain

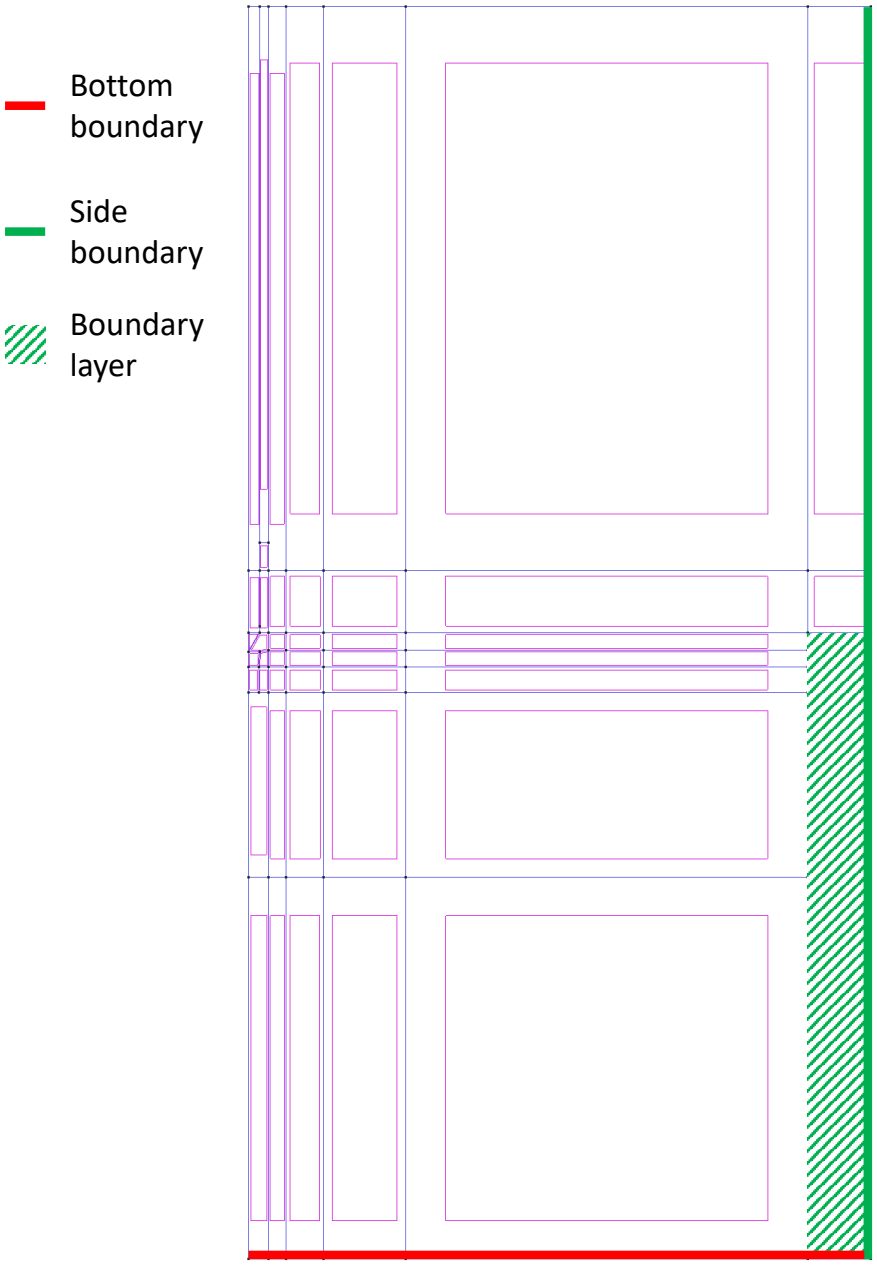

Figure D.1: Overview of the relevant boundaries in the domain.

D.2 Additional figures lateral boundary condition investigation

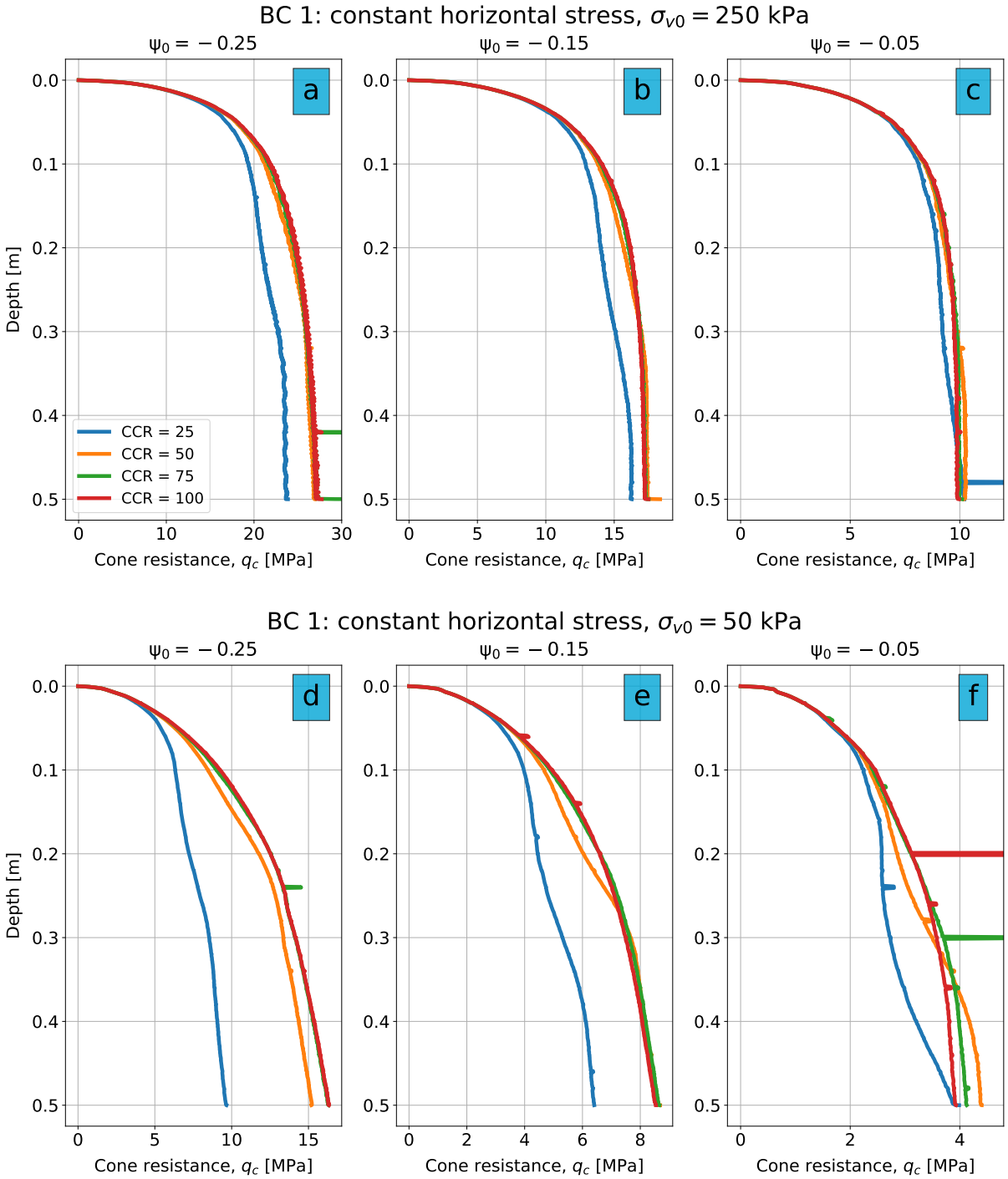

Figure D.2: Depth vs. cone resistance results for a constant lateral stress lateral boundary condition.

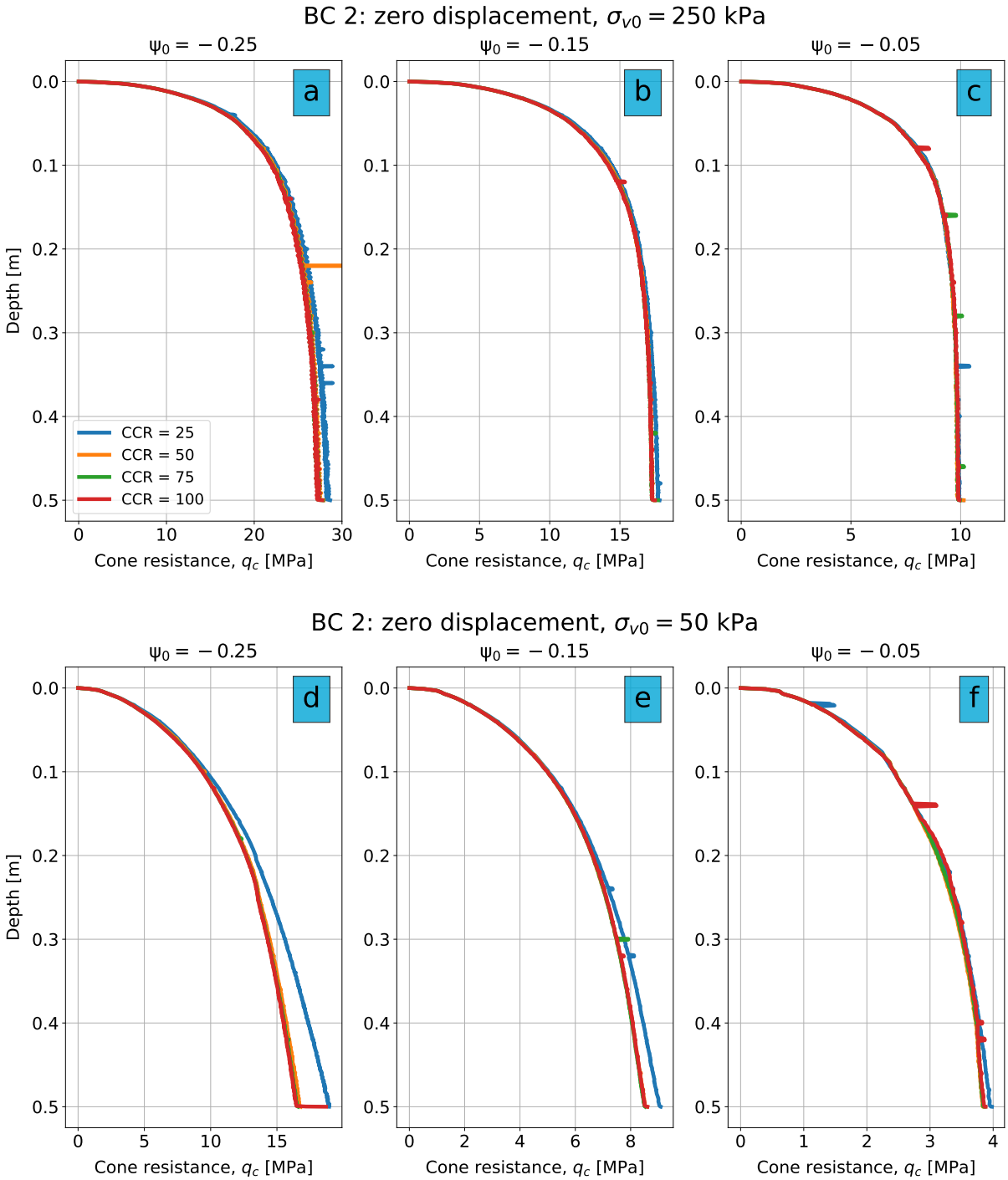

Figure D.3: Depth vs. cone resistance results for a zero displacement lateral boundary condition.

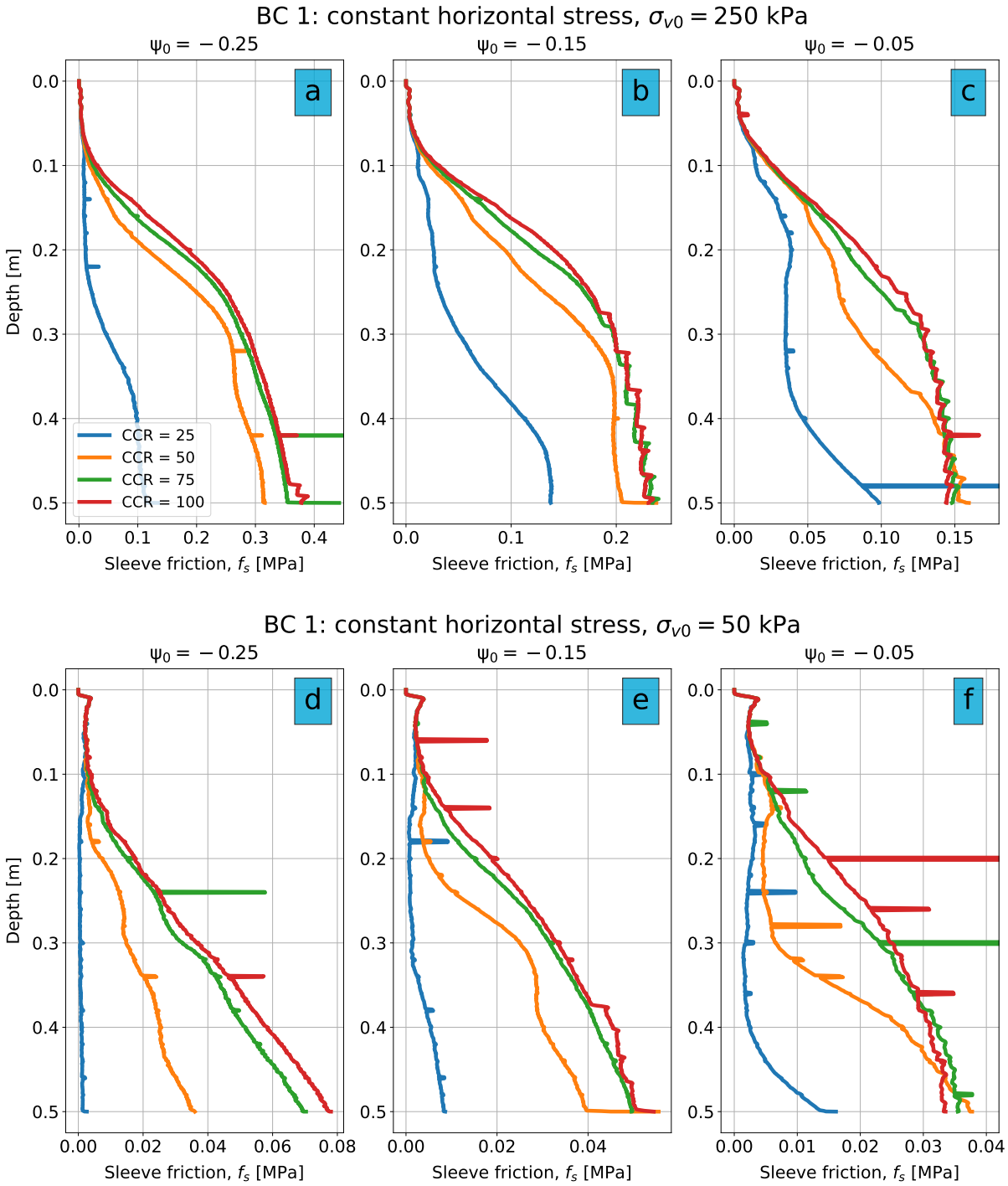

Figure D.4: Depth vs. sleeve friction results for a constant lateral stress lateral boundary condition.

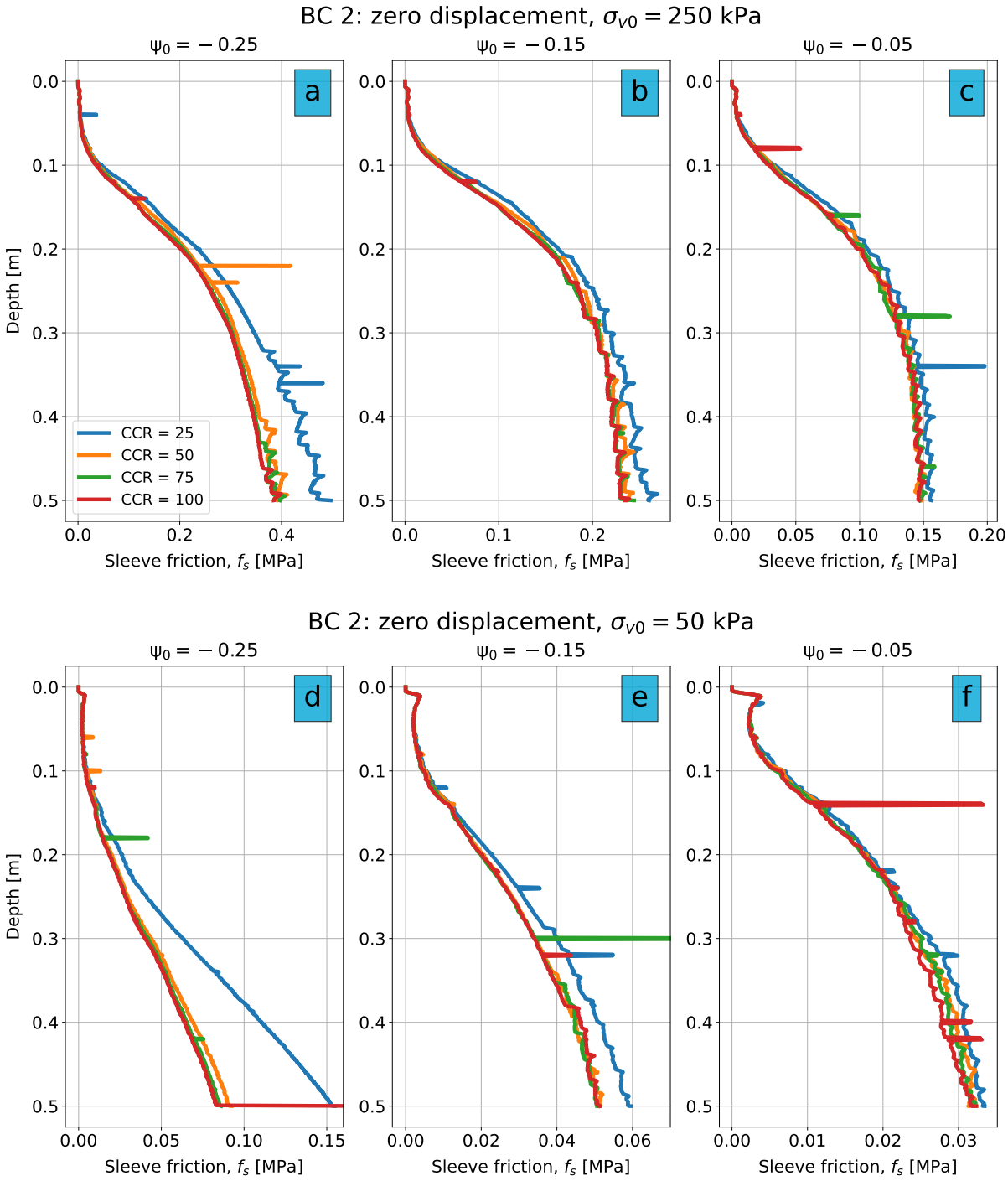

Figure D.5: Depth vs. cone resistance results for a zero displacement lateral boundary condition.

E

Additional Figures and Results for the Validation Phase

In this Appendix the results of the validation phase which are not reported in Chapter 7 due to reasons of conciseness are shown.

E.1 Ticino 4 sand parameter determination

E.1.1 Elasticity parameters

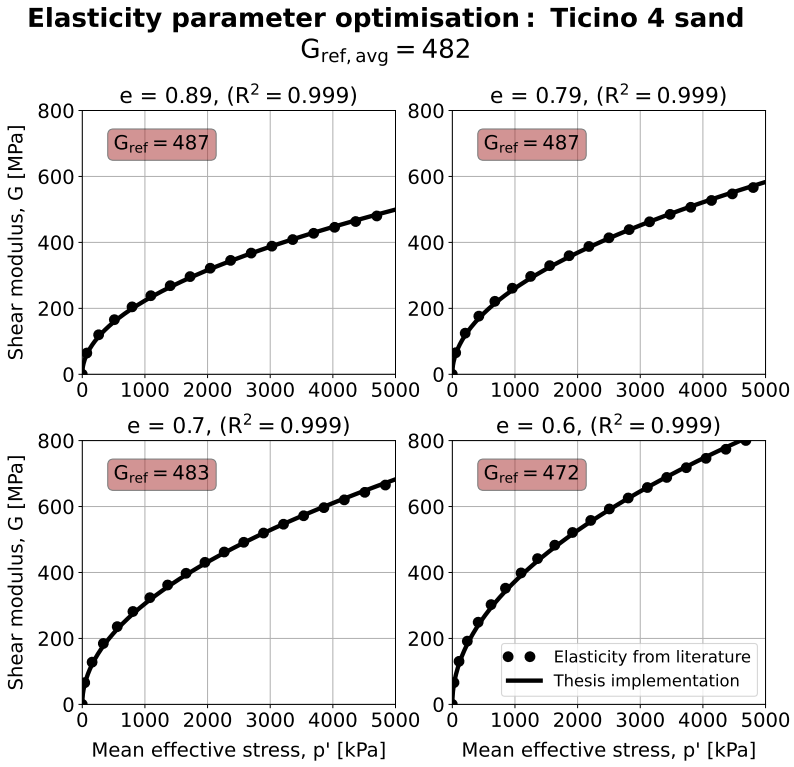

Figure E.1: Results of the elasticity parameter optimisation for Ticino 4 sand.

E.1.2 Curved CSL parameters

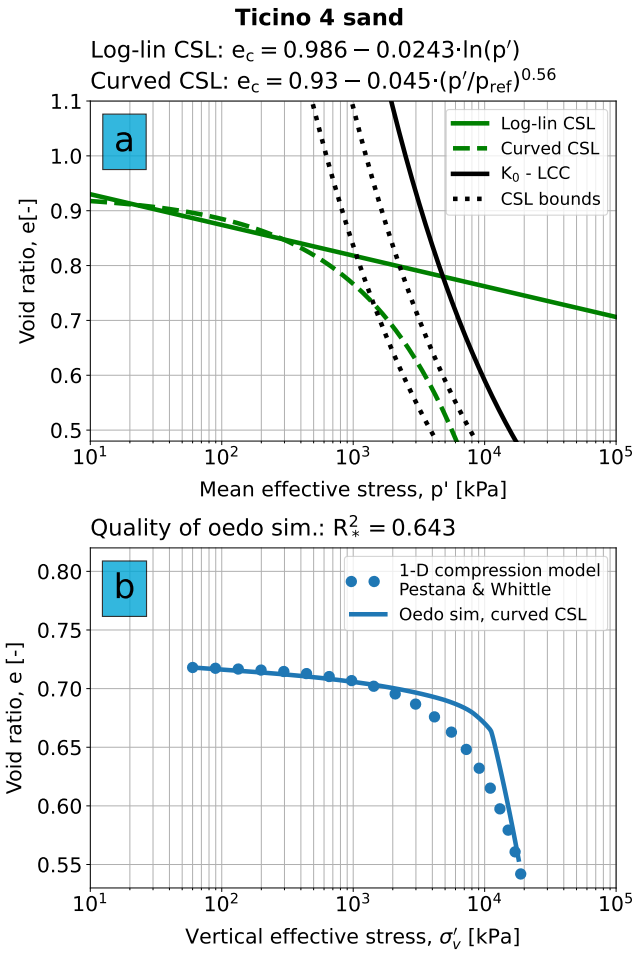

Figure E.2: Results of the curved CSL parameter calibration for Ticino 4 sand.

E.2 Ottawa sand parameter determination

E.2.1 Elasticity parameters

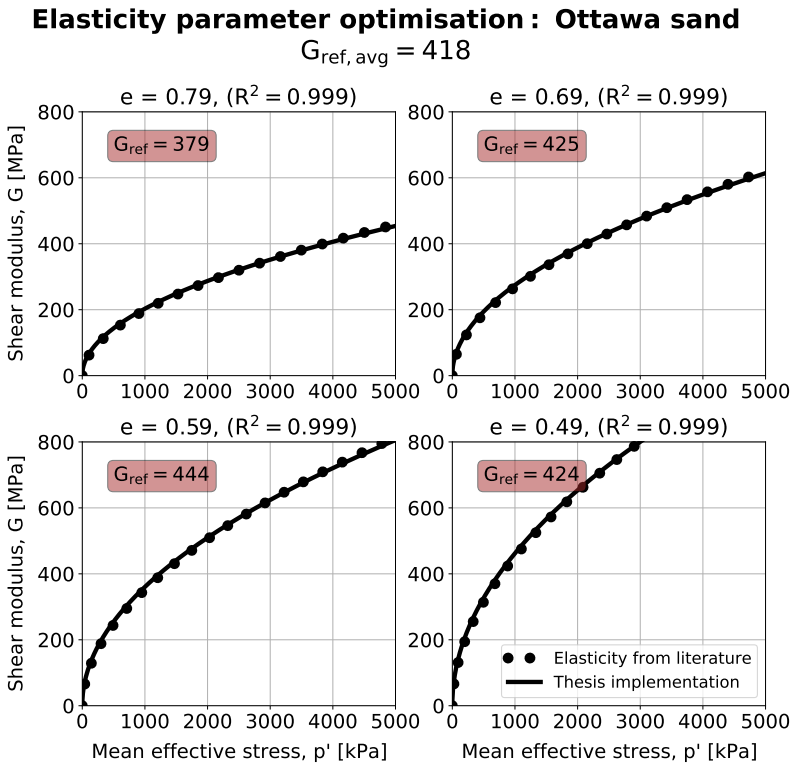

Figure E.3: Results of the elasticity parameter optimisation for Ottawa sand.

E.2.2 Curved CSL parameters

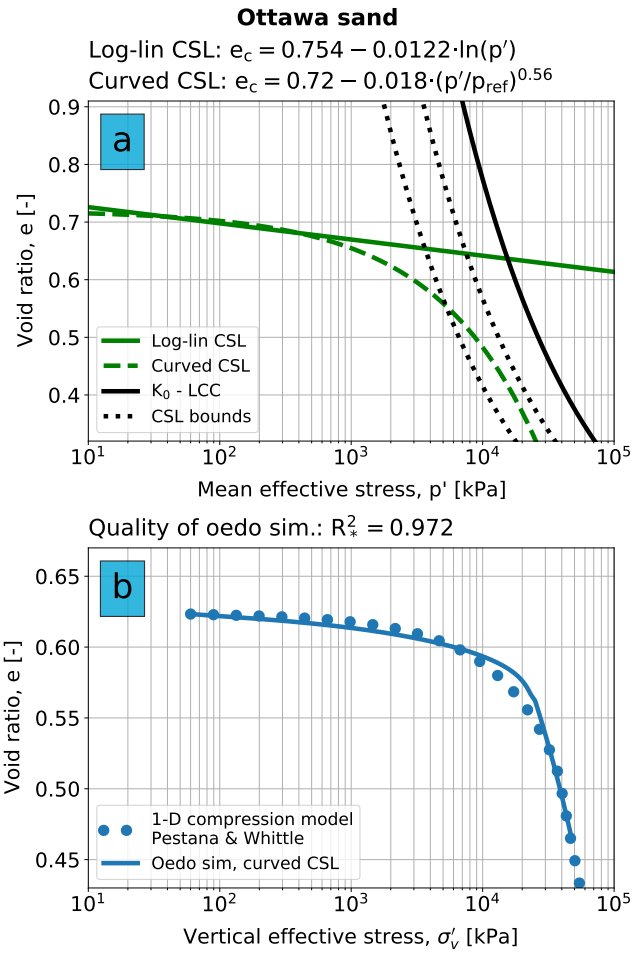

Figure E.4: Results of the curved CSL parameter calibration for Ottawa sand.

E.3 Hokksund sand parameter determination

E.3.1 Elasticity parameters

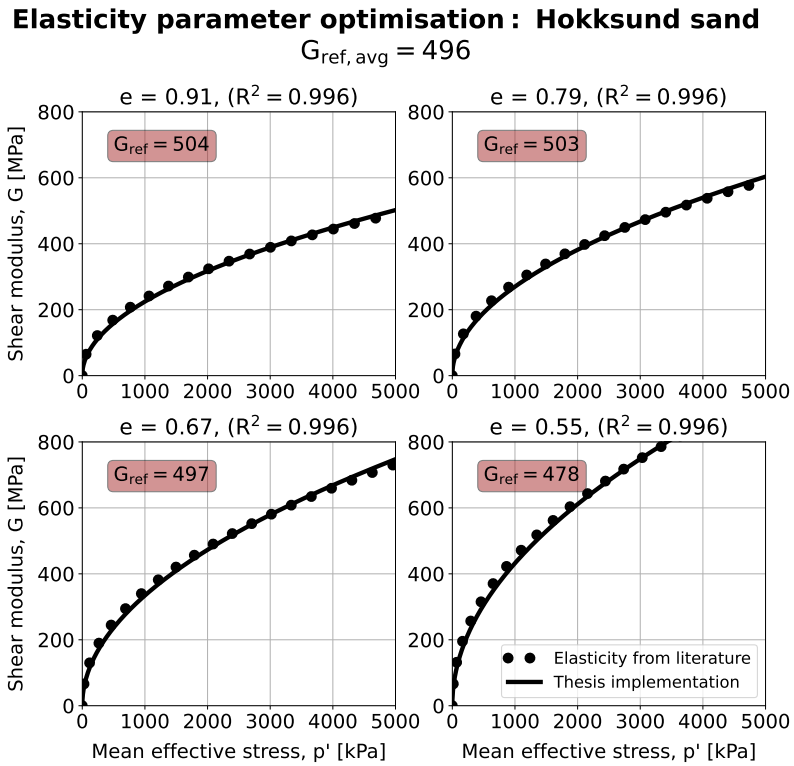

Figure E.5: Results of the elasticity parameter optimisation for Hokksund sand.

E.3.2 Curved CSL parameters

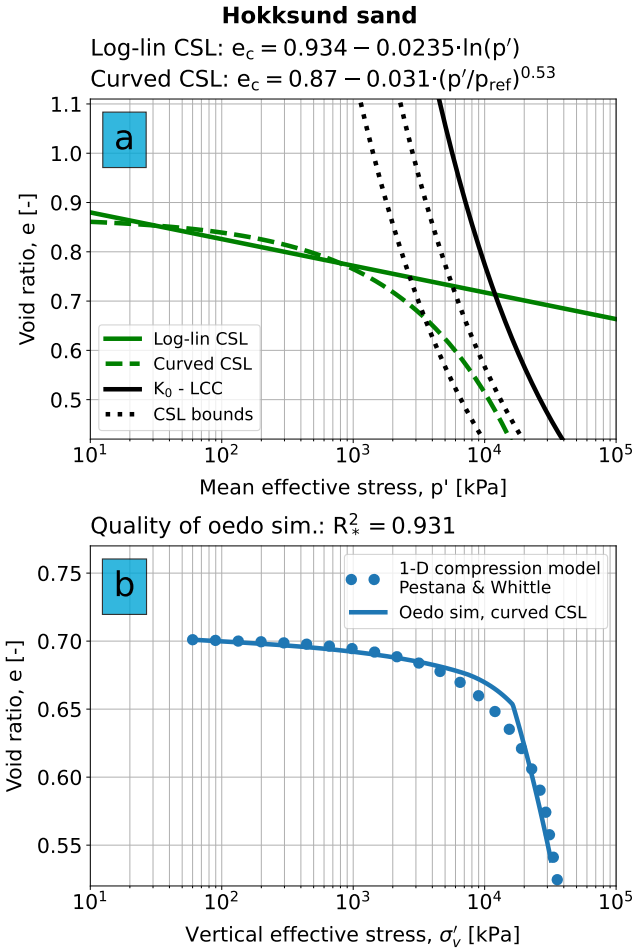

Figure E.6: Results of the curved CSL parameter calibration for Hokksund sand.

E.4 GEBA sand parameter determination

In this Section it is showed how the NorSand parameters for GEBA sand are determined from laboratory tests. The NorSand parameter determination is performed as follows:

1. Determination of elasticity parameter G_{ref};
2. Determination of plasticity parameters;
3. Determination of curved CSL parameters.

For the determination of the plasticity parameters the procedure is followed as described by Jefferies and Been (2016). For a more detailed explanation of the parameter determination procedure the reader is referred to Jefferies and Been (2016) where a clear explanation is provided.

E.4.1 Elasticity parameters

To determine the G_{ref} parameter two types of tests are performed:

1. Bender element (BE) tests by Deltares;
2. Resonant column (RC) tests by Fugro.

Both types of tests are performed for different densities at different stress levels. The result of both test types is a value of the shear modulus G.

In Figure E.7 the results of all conducted BE and RC tests are shown. In the legend it is indicated what the relative density of the sand is for a performed test.

It is important to have multiple stress levels (preferably also more than two) at a constant density such that the G_{ref} parameter of the stiffness equation in the MPM (Eq. 4.1, repeated in Eq. E.1) can be adequately optimised. The results in Figure E.7 show that this is only the case for the BE tests at $D_R = 60\%$. Therefore, the optimisation of G_{ref} is only performed for these three tests. The obtained value of G_{ref} from the optimisation is $G_{ref} = 385$. With this value Eq. E.1 fits well through the three test results at $D_R = 60\%$.

Eq. E.1 describes both the density dependency as well as the stress dependency of the stiffness. This is because the F_e term is a function of the void ratio. Using the value of $G_{ref} = 385$, it is verified for the densities $D_R = 40\%$ and $D_R = 80\%$ if Eq. E.1 results in a shear modulus which is in agreement with the BE and RC tests at these densities. The MPM stiffness function at these densities is shown in Figure E.7 as dotted lines. A first observation at $p' = 200$ kPa is that there is a difference in the obtained shear modulus for BE and RC tests. The MPM value of G falls for both $D_R = 40\%$ and $D_R = 80\%$ in between these values. At $p' = 50$ kPa, generally good matching values between the MPM stiffness implementation and the BE tests are visible.

It is concluded that based on the conducted BE and RC tests the value of $G_{ref} = 385$ is an accurate value in the stiffness relation of Eq. E.1 for GEBA sand.

$$G = G_{ref} F_e p_{atm} \left(\frac{p + p_t}{p_{atm}} \right)^a \tag{E.1}$$

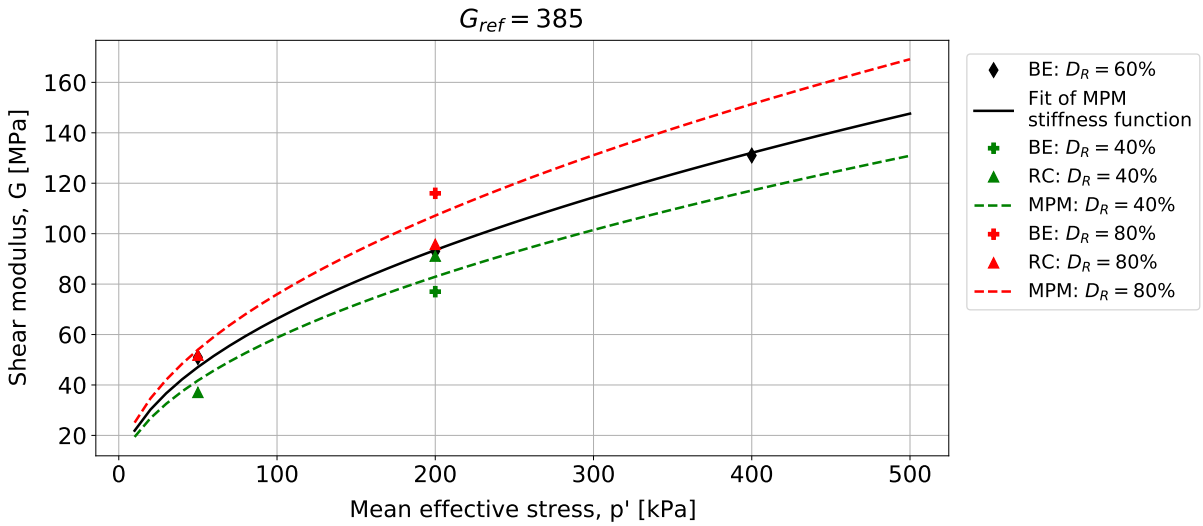

Figure E.7: Results of the performed BE and RC tests. The MPM optimisation fit is shown for $D_R = 60\%$ and verified for $D_R = 40\%$ and $D_R = 80\%$.

E.4.2 Plasticity parameters

Results drained triaxial tests

The NorSand plasticity parameters of GEBA sand are determined based on five consolidated isotropic drained (CID) triaxial tests. The results of the triaxial tests are shown in Figures E.8 to E.12. In the Figures it is indicated what the initial soil state is for each test. Eq. 2.8 (repeated in Eq. E.2) is used to quantify the dilatancy D.

$$D = \frac{\dot{\varepsilon}_v}{\dot{\varepsilon}_q} \tag{E.2}$$

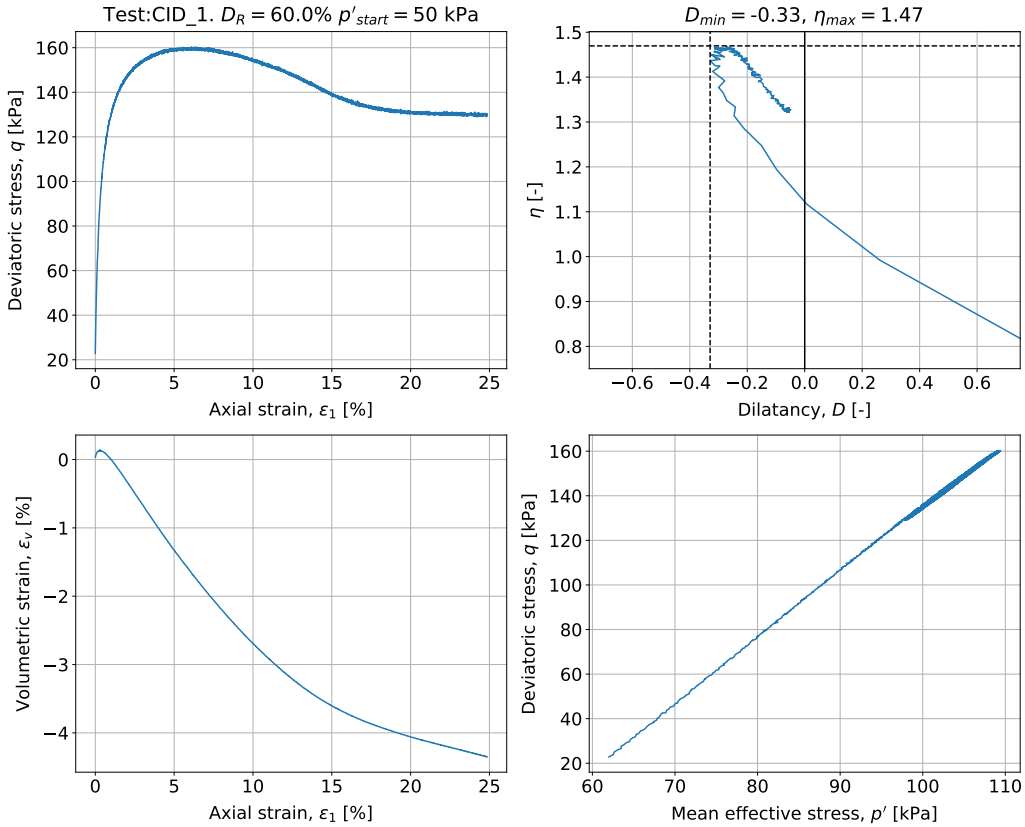

Figure E.8: Results of CID 1.

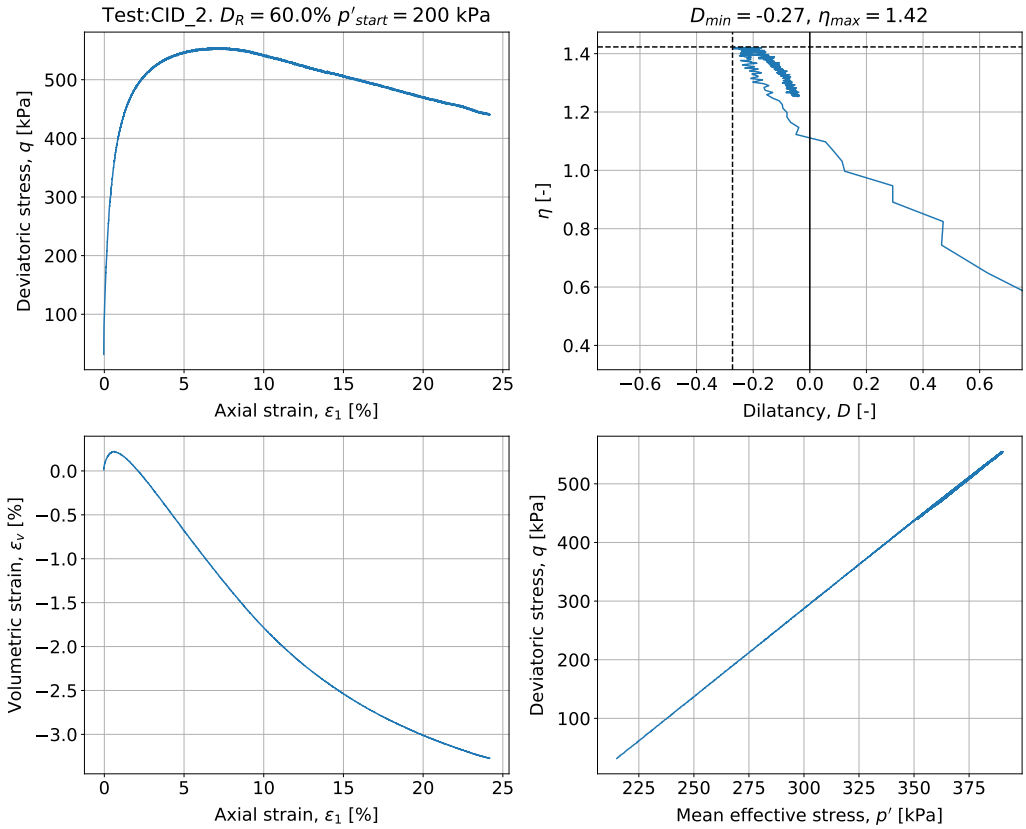

Figure E.9: Results of CID 2.

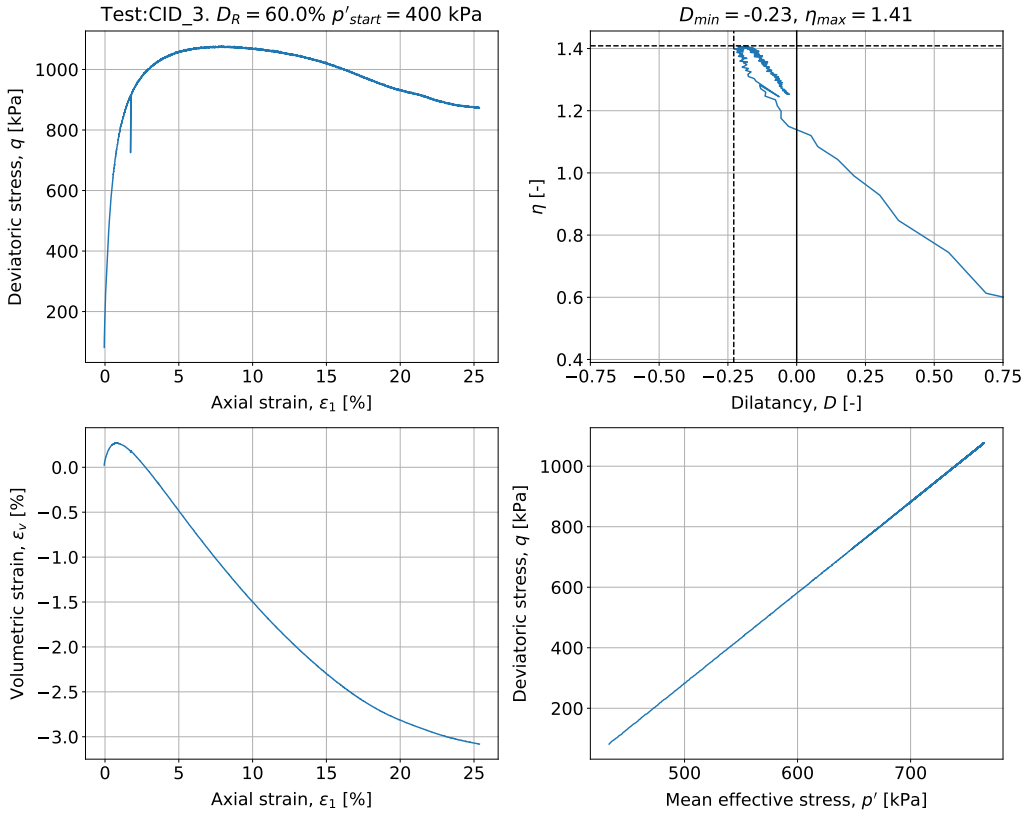

Figure E.10: Results of CID 3.

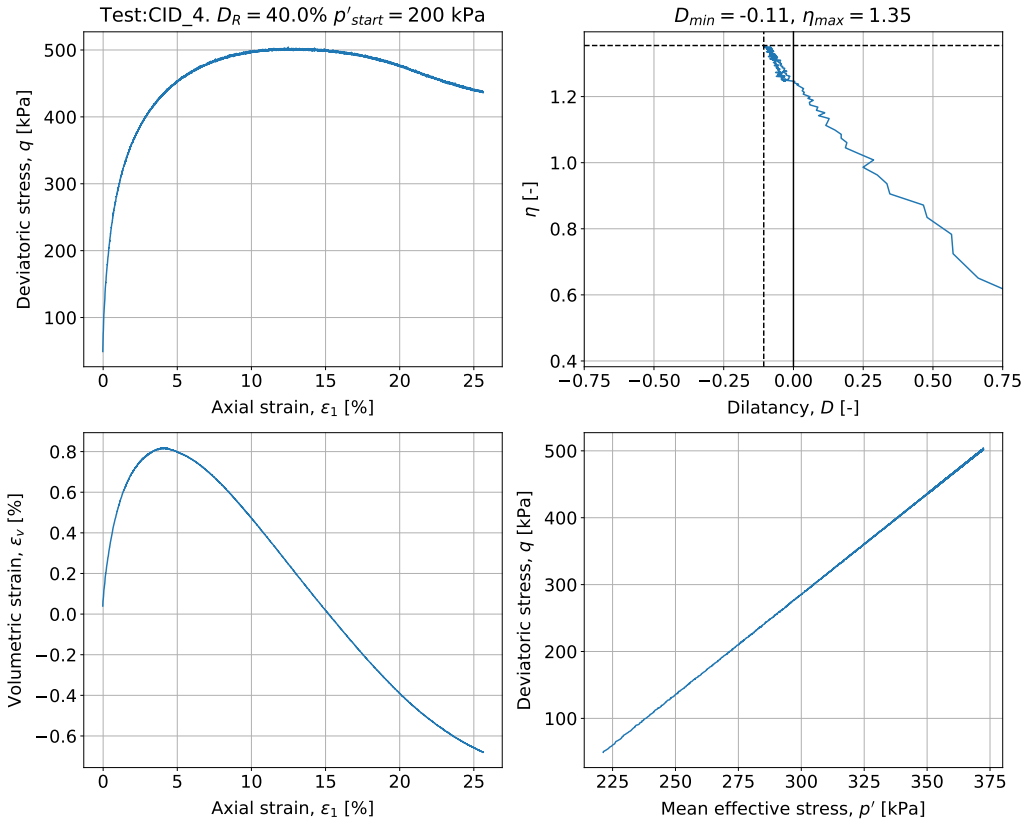

Figure E.11: Results of CID 4.

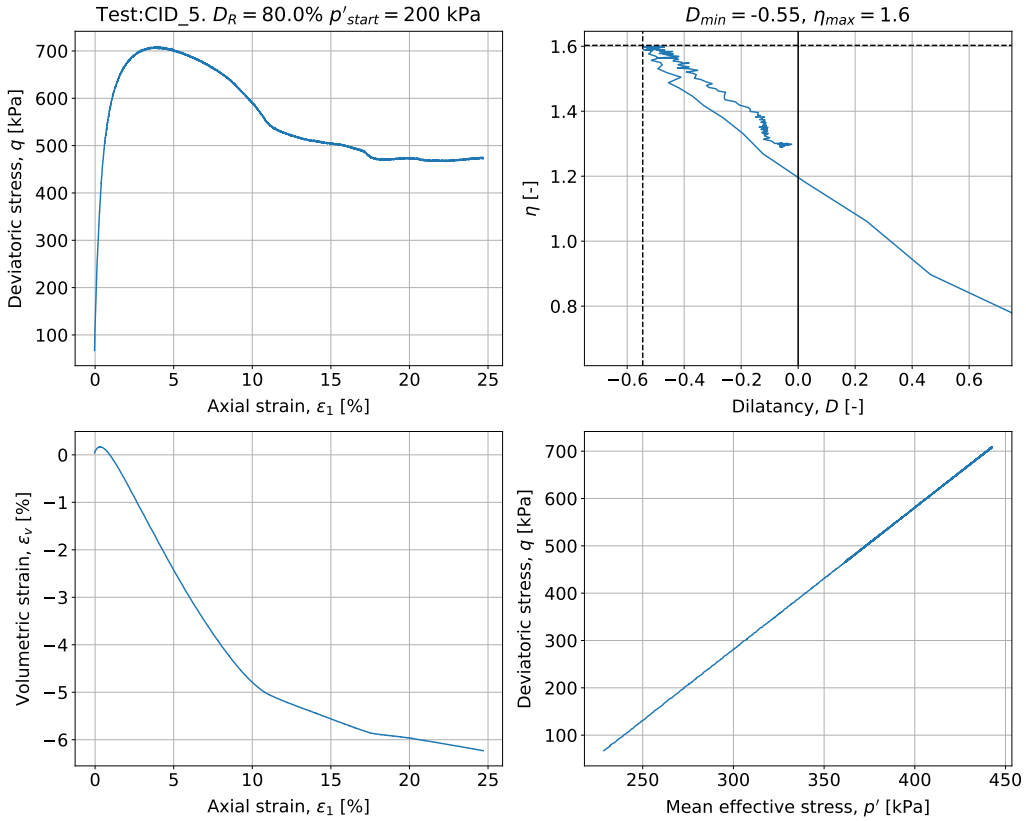

Figure E.12: Results of CID 5.

Obtaining NorSand parameters from triaxial tests

In Figure E.13 the results of the processing of the triaxial tests are shown.

In Figure E.13a the maximum dilation D_{min} is plotted vs. the maximum stress ratio η_{max}. A linear line is fitted through the points. The value of η_{max} for $D_{min} = 0$ is the value of M_{tc}. The slope of the linear fit is equal to $N - 1$, resulting in a value for N.

Figure E.13b shows how the log-linear CSL is determined. Unfortunately, this CSL could not be determined based on the performed triaxial tests, because in some tests the critical state is not fully reached. It is also not advised to determine the CSL based on tests with a high relative density due to the formation of shear zones in the sample. Standard practice according to Jefferies and Been (2016) is to determine the CSL based on both drained and undrained triaxial tests with relative densities ranging from 10% to 30%. These tests are currently not available for GEBA sand. A literature search on GEBA sand properties has been performed to investigate if the CSL of GEBA sand has been previously determined. In the thesis of Chavez Abril (2017) a formulation of a CSL for GEBA is proposed for a hypoplasticity model. The critical void ratio for this formulation is plotted in Figure E.13b. Subsequently the traditional log-linear CSL equation (Eq. 2.5) is fitted through the points to obtain values for Γ and λ.

Using the log-linear CSL obtained in Figure E.13b, the state parameter at D_{min} is determined and is plotted vs. D_{min} in Figure E.13c. A linear line is fitted through the points. The requirement of this fit is that at the point ψ at D_{min} is zero, $D_{min} = 0$. This follows from one of the fundamentals of critical state theory that at critical state the dilatancy is zero. The slope of the fitted line is the value of χ_{tc}.

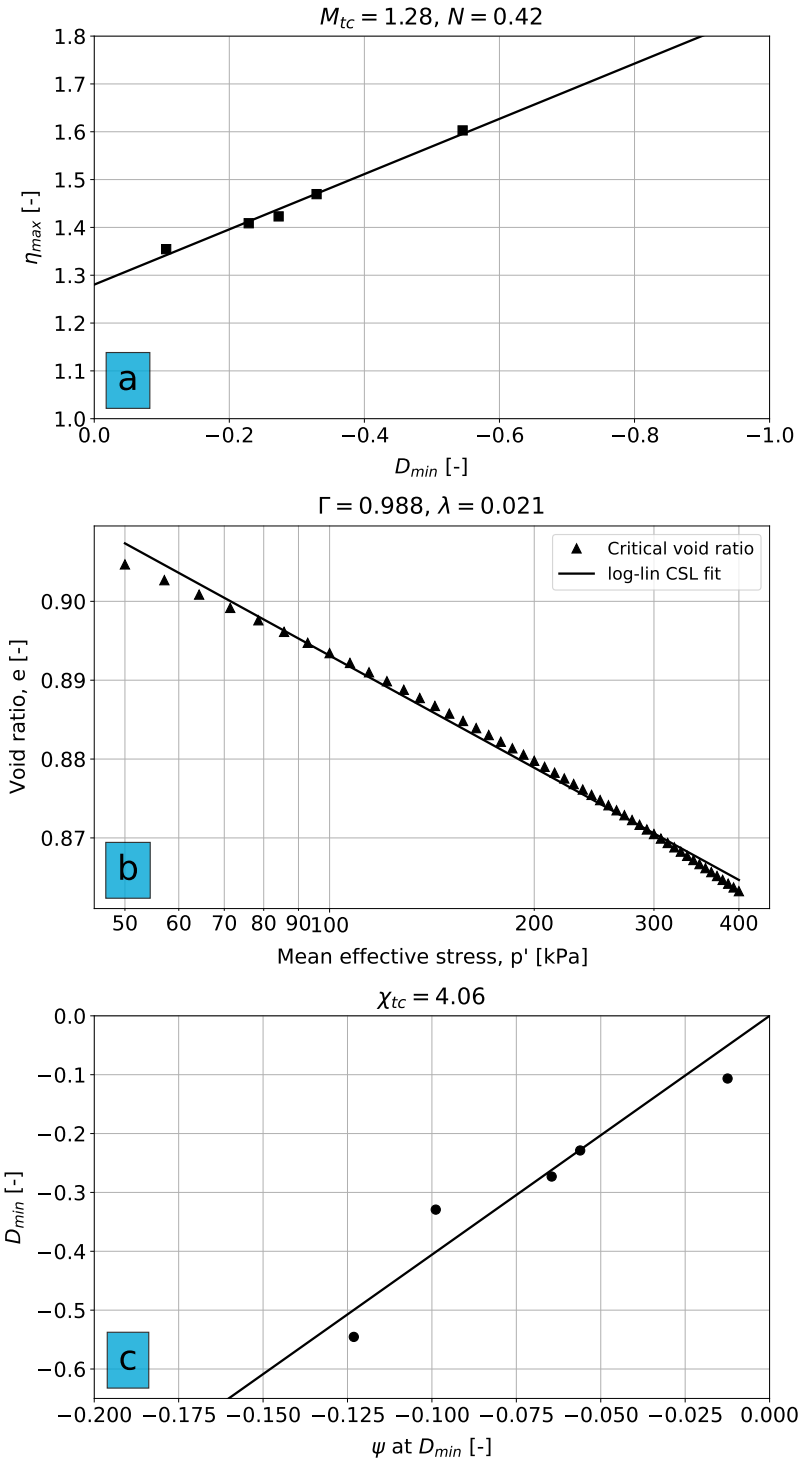

Figure E.13: Results of processing triaxial tests.

Calibrations for hardening modulus H

The hardening modulus H has to be determined by calibration to experimental data. It is possible for H to be a function of ψ. However, due to the limited number of triaxial tests considered it is decided that this relation could not be accurately determined and a constant value of H is used. The proposed value of H is H = 150. In Figures E.14 to E.18 the results of the performed triaxial tests are compared with a simulation of a drained triaxial test using the incremental driver single element program of Niemunis (2007).

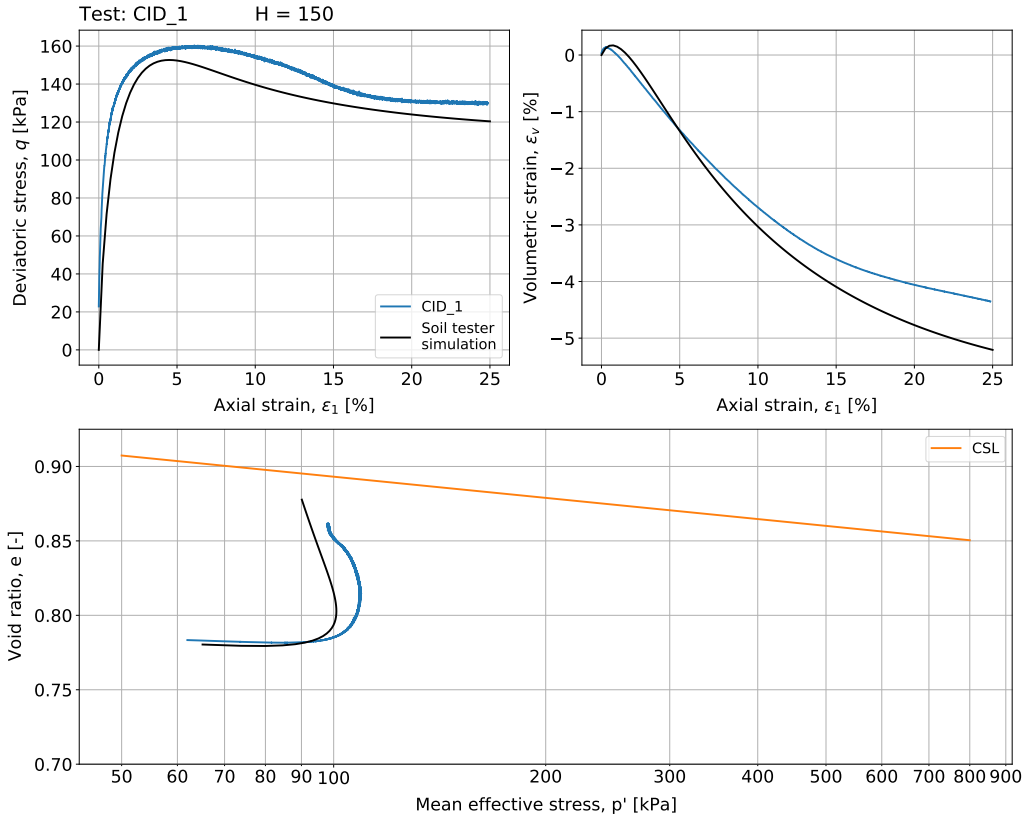

Figure E.14: Results of the soil test calibration of CID 1.

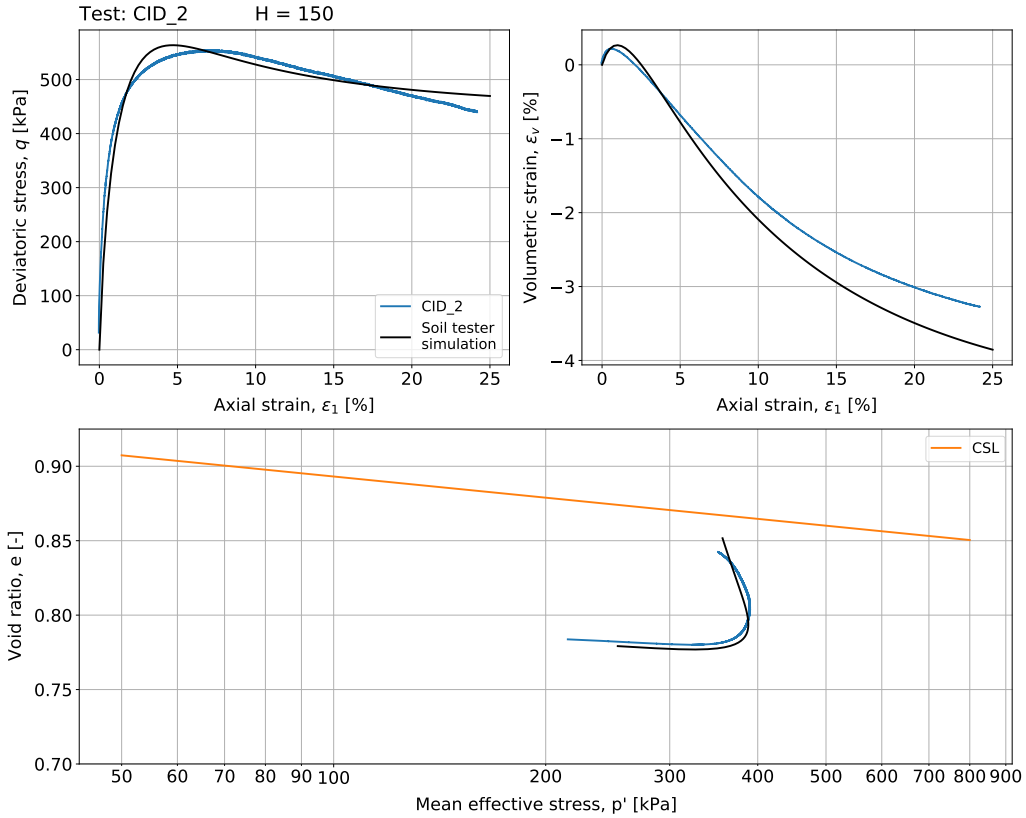

Figure E.15: Results of the soil test calibration of CID 2.

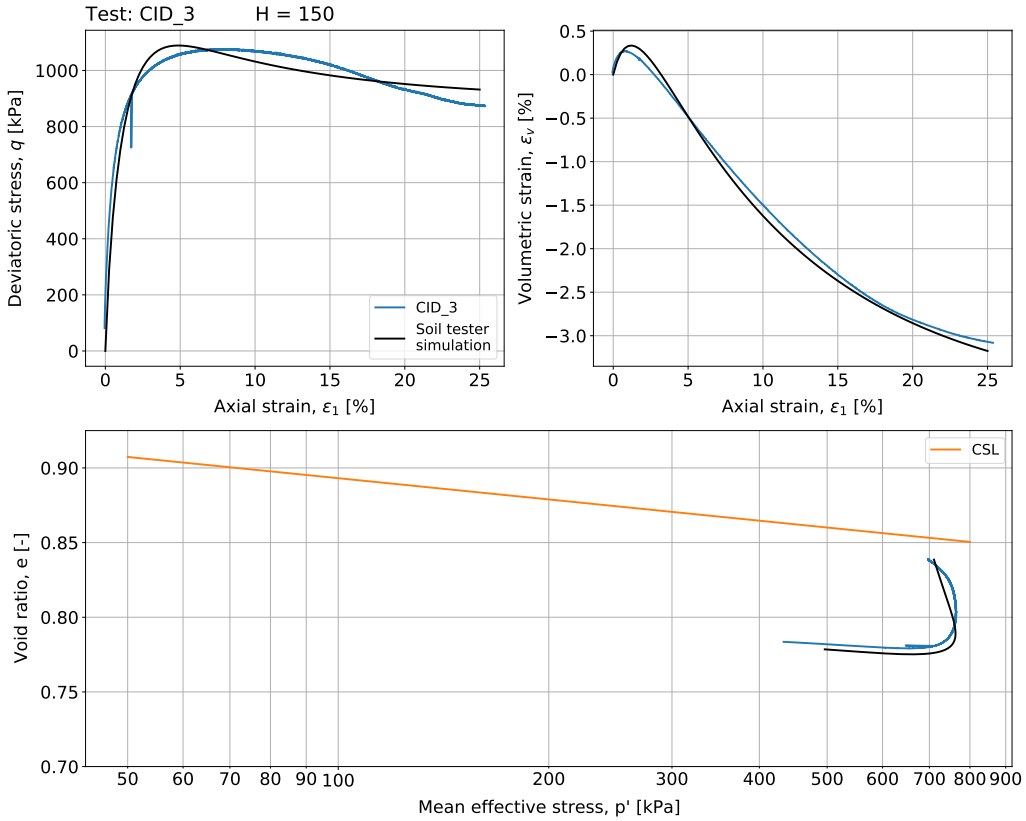

Figure E.16: Results of the soil test calibration of CID 3.

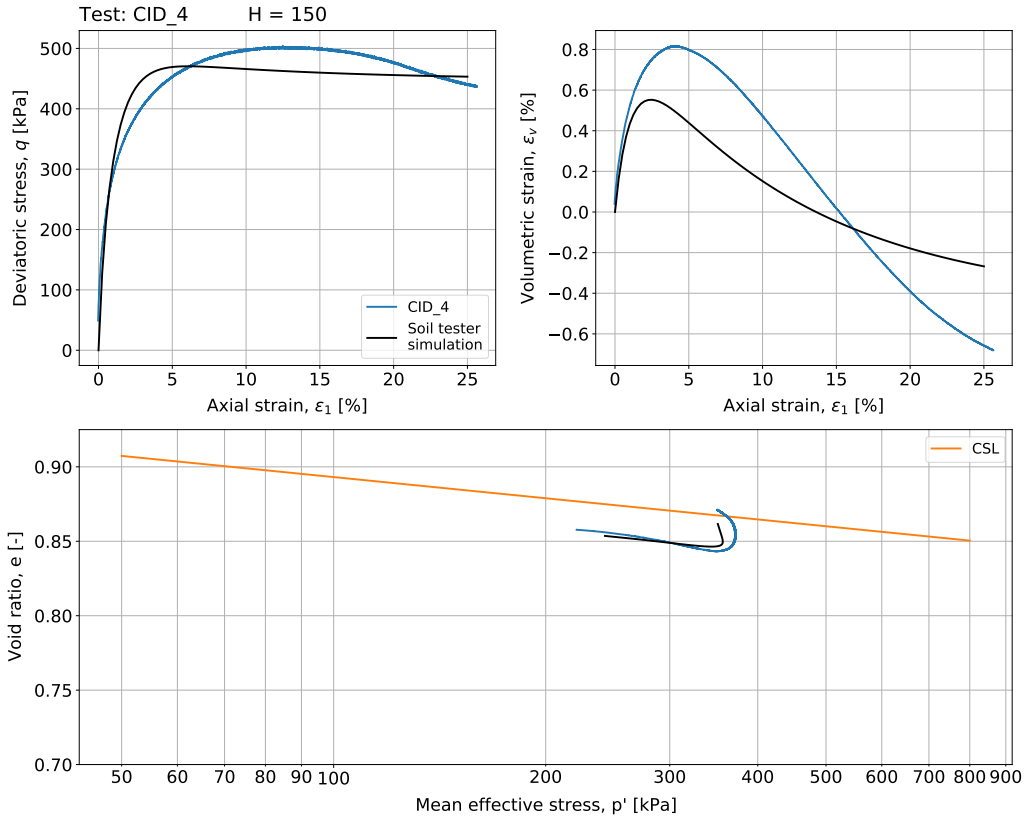

Figure E.17: Results of the soil test calibration of CID 4.

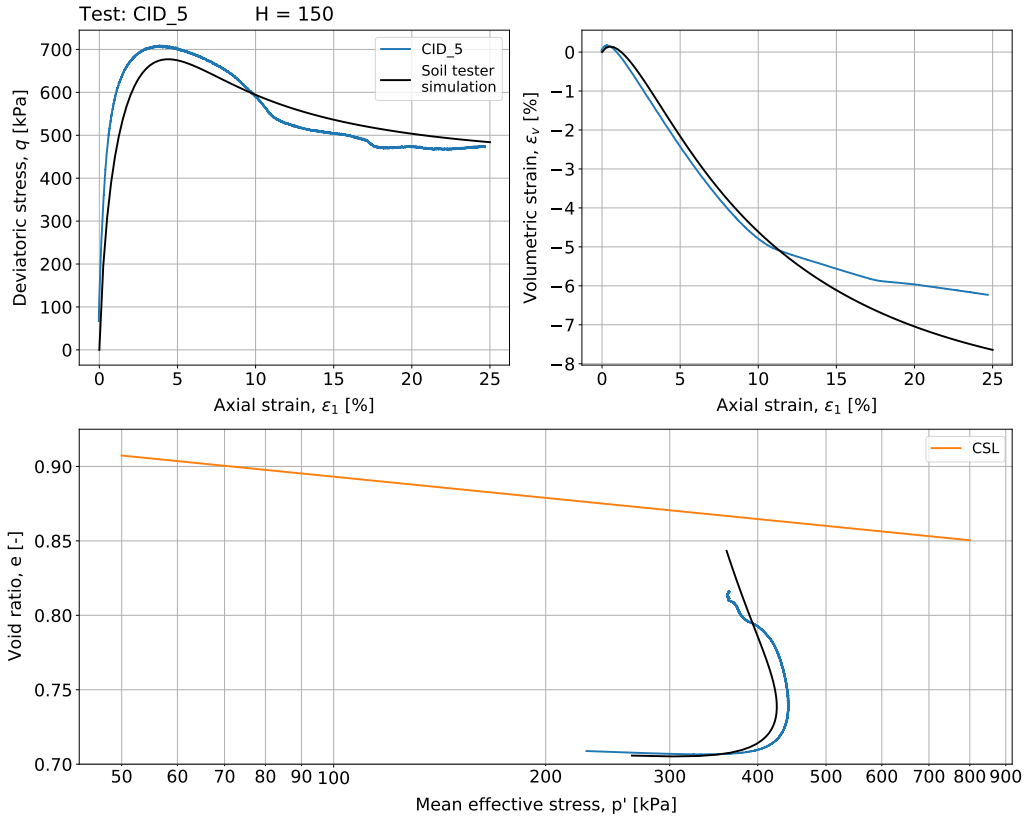

Figure E.18: Results of the soil test calibration of CID 5.

Figures E.14 to E.18 show the results of the calibration of H using the soil tester to the experimental tests. It is inevitable that there are differences between actual tests and a simulation. For certain tests a relatively good agreement is present (e.g. CID 3), whereas for others larger differences are visible (e.g. CID 4). Overall, a value of H = 150 results in an acceptable agreement between the conducted triaxial tests and the simulation using the obtained NorSand parameters. This value will subsequently be used in the calibration of the curved CSL.

E.4.3 Curved CSL parameters

To obtain the curved CSL parameters for GEBA sand a simulation of an oedometer test is performed as is described in Chapter 4. However, instead of a comparison with the compression model of Pestana and Whittle (1995), the simulation is compared with an actual oedometer test conducted in the laboratory of Fugro. The results of the oedometer test and the oedometer simulation are shown in Figure E.19. The best fitting curved CSL parameters are $e_\Gamma = 0.953$, $\lambda_c = 0.060$ and $\xi = 0.32$. The fit optimisation is performed after the unloading of the sample at around $\sigma'_{v0} = 300$ kPa, which can be seen in Figure E.19b.

In Figure E.19a in can be seen that for stress states where $p' \leq 1000$ kPa, the critical void ratio of the log-linear and curved CSL is almost identical. This is what is desired to also accurately describe the critical state a lower stress levels.

Figure E.19b shows a good match between the conducted oedometer test and the oedometer simulation. This indicates that with the proposed parameters NorSand is able to accurately model the compression behaviour of GEBA sand at high stresses (when using the curved CSL).

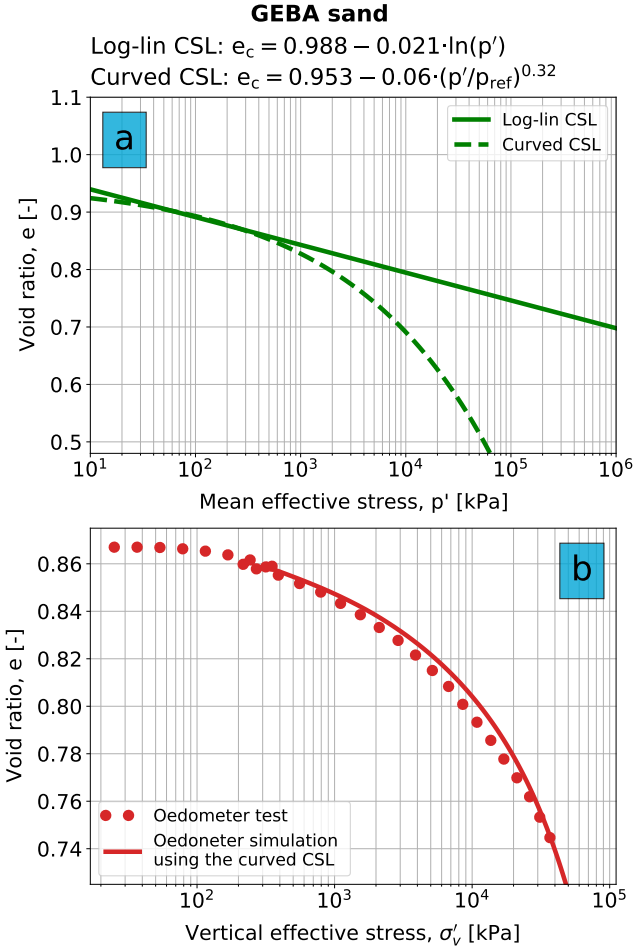

Figure E.19: Results of the curved CSL parameter calibration for GEBA sand.